Space Science Reviews (2022) 218:10
https://doi.org/10.1007/s11214-022-00875-6

Particles and Photons as Drivers for Particle Release from the Surfaces of the Moon and Mercury

P. Wurz[1] · **S. Fatemi**[2] · **A. Galli**[1] · **J. Halekas**[3] · **Y. Harada**[4] · **N. Jäggi**[1] · **J. Jasinski**[5] · **H. Lammer**[6] · **S. Lindsay**[7] · **M.N. Nishino**[8] · **T.M. Orlando**[9] · **J.M. Raines**[10] · **M. Scherf**[6] · **J. Slavin**[10] · **A. Vorburger**[1] · **R. Winslow**[11]

Received: 20 April 2021 / Accepted: 16 February 2022 /

Abstract

The Moon and Mercury are airless bodies, thus they are directly exposed to the ambient plasma (ions and electrons), to photons mostly from the Sun from infrared range all the way to X-rays, and to meteoroid fluxes. Direct exposure to these exogenic sources has important consequences for the formation and evolution of planetary surfaces, including altering their chemical makeup and optical properties, and generating neutral gas exosphere. The formation of a thin atmosphere, more specifically a surface bound exosphere, the relevant physical processes for the particle release, particle loss, and the drivers behind these processes are discussed in this review.

Keywords Mercury · Moon · Exosphere · Release processes · Sputtering · Photon-stimulated desorption · Escape

---

Surface-Bounded Exospheres and Interactions in the Inner Solar System
Edited by Anna Milillo, Menelaos Sarantos, Benjamin D. Teolis, Go Murakami, Peter Wurz and Rudolf von Steiger

✉ P. Wurz
peter.wurz@space.unibe.ch

1 Physics Institute, University of Bern, Bern, Switzerland
2 Department of Physics, Umeå University, Umeå, Sweden
3 Department of Physics and Astronomy, University of Iowa, Iowa City, IA, USA
4 Kyoto University, Oiwake-cho, Sakyo-ku, Kyoto, Japan
5 NASA Jet Propulsion Laboratory, California Institute of Technology, Pasadena, CA, USA
6 Space Research Institute, Austrian Academy of Sciences, Graz, Austria
7 School of Physics and Astronomy, The University of Leicester, Leicester, UK
8 Japan Aerospace Exploration Agency, Sagamihara, Kanagawa, Japan
9 Georgia Institute of Technology, Atlanta, GA, USA
10 Dept. of Climate and Space Sciences and Engineering, University of Michigan, Ann Arbor, USA
11 Institute for the Study of Earth, Oceans, and Space, University of New Hampshire, Durham, NH, USA

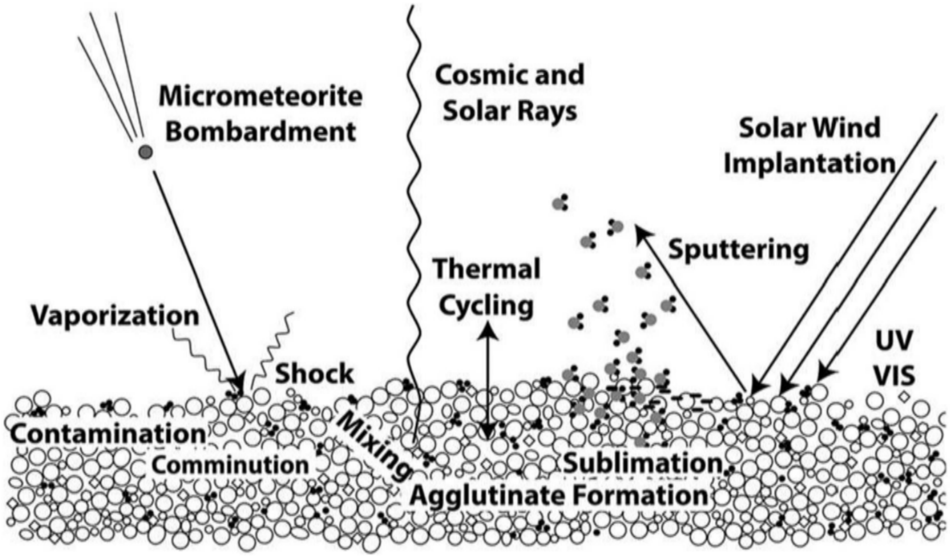

Fig. 1 Summary of the processes acting on the surface of airless planetary bodies, typically covered by regolith of heterogeneous in composition. Figure reproduced from Pieters and Noble (2016), with permission

1 Space Environment

The Moon and Mercury are planetary bodies without a substantial atmosphere, there is only a thin collisionless atmosphere, which is called exosphere. Thus, their surfaces are directly exposed to the ambient plasma (ions and electrons), to energetic particles, to photons mostly from the Sun ranging from the infrared range all the way to X-rays, and to meteoroid fluxes. Direct exposure to these exogenic sources has important consequences for the formation and evolution of planetary surfaces, including altering the chemical makeup of the surface material, formation of the regolith, and significantly modifying optical properties of the surface. These alterations of planetary surfaces are referred to as space weathering in the literature.

Figure 1 shows an overview of the processes acting on the surface of the Moon or Mercury. Actually, the processes illustrated in Fig. 1 apply to the many planetary objects of our solar system that are not protected against these external agents by a sufficient atmosphere.

These external agents are responsible for the formation of a neutral gas exosphere, and the escape of a fraction of particles from this exosphere into space. Since the particles in the exosphere have their origin at the surface of the Moon or Mercury, we speak of a surface bound exosphere. The origin of the exospheric particles, the relevant physical processes for the particle release, the loss of particles from the exosphere to interplanetary space, and the drivers behind these processes are the main topic of this review.

1.1 Space Weathering

The effects of these external agents on the surface of airless planetary bodies are discussed in the literature as space weathering. Space weathering is very important for studies of planetary bodies by remote sensing because it causes major changes in the optical properties of the surfaces over time. Micrometeorites, solar wind plasma and electromagnetic radiation bombard the surfaces of Mercury, moons, and asteroids without atmospheres during billions of years. Therefore, these processes can have important effects on the regolith, which can result in particle implantation, chemical modification of surface material, surface spectral alterations (darkening, reddening and subdued absorption bands), and the distinctive magnetic electron spin resonance caused by single-domain metallic iron particles (e.g., Hapke 2001; Noble et al. 2007; Pieters and Noble 2016).

Space weathering gradually alters unprotected surfaces that are exposed to the harsh space environment to some degree in their chemical composition and physical properties. As illustrated in Fig. 1, there are multiple processes that act simultaneously, at times together, to alter surface materials in different efficiencies. Understanding the causes and the effects, however, is not simple.

Two important parameters that can be found in the space weather-related literature are soil maturity and exposure age. Soil maturity describes the degree to which a given surface material has accumulated space-weathering products (e.g., Morris 1977; Lucey et al. 2000), while the exposure age is a quantitative laboratory measure of how long soil or rock grains have been exposed to space. The latter is ascertained on measurements of accumulated products such as solar wind noble gases or cosmic ray tracks (e.g., Zinner 1980; Berger and Keller 2015). One can group space weathering processes more or less in two broad categories (see Fig. 1) that are related to: i) random impacts by small particles throughout the solar system and ii) irradiation by electromagnetic radiation (e.g., solar X-ray, EUV, flares), and plasma from the Sun (solar wind, Coronal Mass Ejections (CMEs), solar energetic particles (SEPs)), galactic sources (cosmic rays, gamma-ray bursts, etc.), or magnetosphere accelerated ionized particles (magnetic storms, etc.).

Solar X-rays, EUV radiation, solar wind electrons and ions will excite atoms at the surface of airless planetary bodies, which can produce line emission and bremsstrahlung. This makes it possible to infer information on the surface composition from measured X-ray fluorescent spectra. On the Moon, on Mercury, and other solar system bodies, solar-induced X-ray emissions from the surfaces have been used to infer element abundances (e.g., Adler and Trombka 1977; Banerjee and Vadawale 2010; Okada et al. 2009; Starr et al. 2012).

Incident solar wind protons will be implanted in the regolith of an airless body where they can excite and ionize other atoms. Moreover, high-energy particles produce various types of physical and chemical defects and hence cause chemical alteration of the surfaces (e.g. Mura et al. 2009; Tucker et al. 2019). On the Moon it is expected that the diffusion of H atoms is lower when the atoms form metastable bonds with O atoms (Tucker et al. 2019). H atoms that diffuse can also recombine with another H atom, leading to the direct formation of H_2 that is then degassed into the exosphere.

The incident high-energy protons of SEPs ($\sim$MeV) may cause dielectric breakdown of the lunar regolith, in particular in the shadowed regions inside the polar craters (Jordan et al. 2015, 2017; Jordan 2021). The dielectric breakdown may alter the porosity of the subsurface ($\sim$1 mm), facilitating vaporization of volatile elements in the regolith. The same process may also take place at the surface of other airless bodies including Mercury.

1.2 Mercury's Space Environment

The space environment of Mercury is dominated by its interaction with the Sun, which, owing to its close proximity, is the most intense of all the planets in the solar system (Milillo et al. 2020). As the solar wind expands radially outwards throughout the heliosphere, the plasma density and interplanetary magnetic field (IMF) magnitude decrease with distance from the Sun (Russell et al. 1988). This has important consequences on both the plasma conditions at Mercury's orbit as well as the planet's interaction with the solar wind. As Mercury travels through its elliptical orbit between 0.31–0.46 AU distance, it experiences solar wind proton densities that are 5–10 times higher than at the Earth and IMF magnitudes

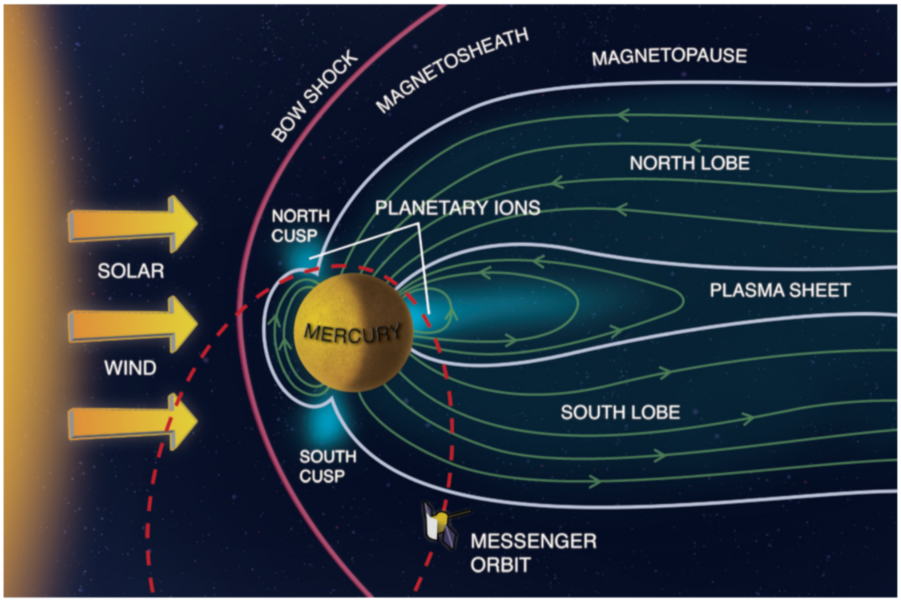

Fig. 2 Mercury's miniature magnetosphere. Figure adapted from Zurbuchen et al. (2011) with permission

that are 3–5 times higher (Masters 2018). Mercury is partially shielded from this interaction by a weak planetary dipole magnetic field of 190 nT-R_M^3, which has an offset northwards by about 490 km (Anderson et al. 2012; Johnson et al. 2012). The magnetic dipole forms a permanent intrinsic magnetosphere similar to that of the Earth, though much smaller in size (Fig. 2). The plasma populations and processes resulting from the interaction between Mercury's magnetic field and the solar wind plasma, leading to the formation of Mercury's magnetosphere, have been reviewed by Seki et al. (2015). The combination of higher solar wind density and IMF strength promotes frequent magnetic reconnection of the IMF with Mercury's planetary magnetic field (DiBraccio 2013; Slavin et al. 2014). Magnetic reconnection is a process that rearranges the topology of magnetic fields, releases magnetic energy and results in the acceleration of plasma; it is the primary mechanism in energizing space plasmas (see book by Gonzalez and Parker 2016). This process brings energy, plasma and magnetic flux into Mercury's magnetospheric system, and produces wide-ranging effects on the surface, exosphere and magnetosphere. The stripping away of the dayside magnetosphere drives Earth-like Dungey cycle plasma convection (Dungey 1963; Slavin et al. 2009) that circulates plasma and magnetic flux into the nightside magnetosphere and drives magnetic reconnection in the magnetotail.

The rate of reconnection at the Earth's magnetopause is very low when the IMF B_Z is positive, but increases rapidly as B_Z becomes strongly negative. The underlying reason for this well-known "half-wave rectifier effect" in the response of Earth's magnetosphere to IMF clock angle is attributed to the relatively high plasma beta, the ratio of kinetic to magnetic pressure, in the magnetosheath. Under these conditions the magnetic field just inside the magnetopause is much larger than that in the magnetosheath and the reconnection rate is reduced relative to situations where the magnetic fields on the inside and outside of the magnetopause are similar (Sonnerup 1974; Koga et al. 2019). The low Alfvenic Mach numbers in the inner heliosphere reduce plasma beta in Mercury's magnetosheath relative to conditions at Earth (Gershman et al. 2013). For this reason, the magnetic fields on the inside and outside of Mercury's magnetopause are similar in contrast to Earth, and the reconnection rates measured by MESSENGER are indeed significantly higher than typically found at Earth (Slavin et al. 2021). As at Earth, magnetopause reconnection rate and related phenomena such as flux transfer events are observed to become more frequent and intense with increasingly negative IMF B_Z at Mercury (DiBraccio 2013; Leyser et al. 2017; Sun et al. 2020). For this reason, the high rates of reconnection at Mercury still drive the injection of large fluxes of solar wind plasma into the magnetospheric cusps and high levels of magnetic flux transfer into the magnetotail even for positive IMF B_Z and more modest IMF clock angles (Slavin et al. 2014; Sun et al. 2020). Overall, however, reconnection at Mercury's magnetopause has been observed to be less sensitive to magnetic shear angle than at Earth (Slavin et al. 2014) primarily due to lower plasma beta values (Gershman et al. 2013; Slavin et al. 2014). High-time resolution magnetic field and plasma measurements from MESSENGER indicate that magnetopause reconnection is dominated by the formation of flux transfer events (FTE)—type flux ropes that channel accelerated solar wind plasma from the reconnection site into the magnetospheric cusps down to the surface (Slavin et al. 2020). FTEs have been observed at Earth before (see Lee and Fu 1985) but occur much more frequent at Mercury. MHD simulations with embedded particle-in-cell computations have shown that FTE-type flux ropes form frequently under the action of highly dynamic reconnection at multiple X-lines at the dayside magnetopauses of planetary magnetospheres even in the presence of only small angular shears between the interplanetary magnetic field and the planetary field (Chen et al. 2017).

Closer to and within the magnetospheric cusps the solar wind plasma takes the form of cusp plasma filaments when channeled downward by the FTE (Slavin et al. 2012; Poh et al. 2016). Multiple FTEs are frequently observed as "showers" with the individual flux rope events separated by only a few seconds and the total number identified while MESSENGER was near the magnetopause reaching 10 to 100 (Slavin et al. 2014). MESSENGER observations have shown that these FTE showers are observed on approximately 50% of the dayside MESSENGER orbits and that the FTE showers contribute up to 85% of the magnetic flux transferred from the dayside to the nightside magnetosphere into the lobes of the magnetotail during Mercury's Dungey cycle (Sun et al. 2020). Examination of MESSENGER FIPS plasma measurements in the vicinity of the northern magnetospheric cusp during FTE showers has revealed the formation of a cusp entry layer with strong enhancements in the downward flux of solar wind protons and Na-group ions (Na through Si) originating from the surface due to sputtering by impacting ions (Sun et al. 2022). The flux of solar wind protons impacting on the surface in and around the cusp is found to increase from order 10^{24} to 10^{25} s^{-1} during FTE showers (Sun et al. 2022).

Magnetic reconnection on the dayside magnetopause allows entry of solar wind plasma which is energized and funneled into the magnetospheric cusps where it travels along magnetic field lines towards the planetary surface. Particles that are injected with sufficiently field-aligned pitch angles (i.e., the angle between the particle velocity direction with respect to the magnetic field) will not be reflected away by the increasing magnetic field strength closer to the planet, but will instead impact on Mercury's surface. Orientations in the $-B_Y$ or $+B_Y$ directions will act to shift the cusp dawnwards or duskwards, respectively (Massetti et al. 2003; Jasinski et al. 2017). Continuous reconnection at $-B_Z$ orientations will act to lower the cusp in latitude, resulting in particle impact on the surface occurring closer to the equator (e.g. Raines et al. 2022). A lower southern extent of the cusp due to reconnection at times of $-B_Z$ would also imply an altogether wider latitudinal extent (e.g., Winslow et al. 2012, 2014, 2017). The IMF magnitude is also important; higher magnitudes will produce higher parallel electric fields, which will accelerate more protons along the magnetic field increasing the fluxes and the energies of the particles impacting on the surface (simulations of reconnection from e.g., Egedal et al. 2012; Li et al. 2017; and Mercury observations e.g.

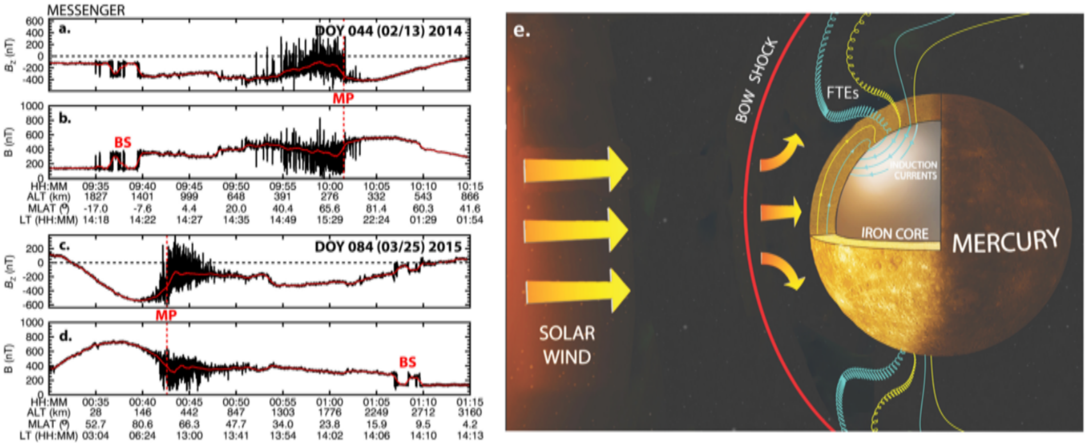

Fig. 3 Total B and the B_z component of the magnetic field measured by MESSENGER during likely ICME intervals in 2014 (panels **a**-**b**) and 2015 (panels **c**-**d**). The black trace displays the full rate magnetometer data (20 s^{-1}), while the red trace depicts the smoothed data. The bow shock and magnetopause crossings are labelled "BS: and "MP." Panel **e**: The solar wind interaction with Mercury during these disappearing dayside magnetosphere (DDM) events is illustrated in the right-hand image. The magnetic field lines due to the core dynamo and the induction currents on the core surface are shown in yellow and green, respectively. The incident solar wind and very near bow shock are shown with yellow-orange arrows and red conic section (adapted from Slavin et al. 2019)

Jasinski et al. 2017). By using MAG and FIPS data on MESSENGER it was observed that weaker IMF magnitudes at Mercury are responsible for ion velocity distributions after reconnection that are more likely to be reflected in the cusp fields and therefore these ions do not impact on the surface of Mercury (Jasinski et al. 2017).

During ICME impacts Mercury experiences very high dynamic pressure from the solar wind and strong southward interplanetary magnetic fields (Slavin et al. 2014, 2019; Winslow et al. 2020). Slavin et al. (2019) reported that the usual $B_z > 0$ closed magnetic flux dayside magnetosphere situated between the north and south cusps is replaced by the most intense showers of FTEs observed by MESSENGER (i.e., the large variance in B-total and B_z just sunward of the magnetopause shown in Fig. 3). The magnetopause is observed only at very high latitudes just sunward of Mercury's terminator plane. The average B_z magnetic field (Fig. 3 red trace) becomes positive nowhere indicating, consistent with the very high latitude magnetopause crossings, that MESSENGER did not observe closed dayside magnetic flux even though it reached altitudes as low as ∼300 to 400 km. The magnetic flux removed from the dayside is split between the flux compressed into the crust by the extremely high solar wind pressure and an intensified Dungey circulation of mostly FTE-type flux ropes forming near the magnetopause and the nightside magnetosphere. It is important to note that MESSENGER observed the bow shock to be very close to the Mercury during these DDM events (see Fig. 3e) implying direct solar wind impact and absorption over nearly the entire dayside hemisphere of Mercury (Slavin et al. 2019).

MESSENGER observations of weaker IMCEs and high-speed solar wind interactions with Mercury's magnetosphere have been investigated with global MHD simulations. The results reproduced the measured magnetic field and found that solar wind compression, the generation of induction currents on the surface of Mercury's iron core and reconnection-driven magnetic flux transfer into the tail are all important to understanding these interactions under extreme solar wind forcing (Jia et al. 2015). Similar simulations have been done by Heyner et al. (2016) and follow-up studies were done by Jia et al. (2019). Further global simulations are planned or are underway for these very strong ICMEs reported by Slavin et al. (2019) and Winslow et al. (2020). As suggested by the DDM illustration in Fig. 3, these simulations are expected to provide new windows into the effect of intense solar wind and interplanetary magnetic fields on magnetized planets in close orbits about their stars everywhere. A three-dimensional ten-moment MHD multifluid model which incorporates the nonideal effects including the Hall effect, electron inertia, and tensorial pressures was used for investigating collisionless magnetic reconnection in Mercury's magnetotail and at its magnetopause (Dong et al. 2019).

On the nightside in Mercury's magnetotail, reconnection-driven convection causes plasma impact on the surface there as well (Kallio and Janhunen 2003; Fatemi et al. 2020). Transport of plasma and magnetic flux from the dayside loads the magnetotail, until it is released by reconnection in the tail (Slavin et al. 2021; Imber and Slavin 2017). This process accelerates plasma toward the nightside of the planet, where a fraction of it may impact the surface. Based on models from Earth (Suszcynsky et al. 1993; Shiokawa et al. 1993) the impacting particles, mostly protons and electrons originating from the solar wind, are thought to be deflected by the planetary magnetic field and reach the surface near the open-closed field line boundary in the plasma sheet horns (see also review by Raines et al. 2015). Evidence of this flow braking and subsequent flux pileup has been inferred from analysis of magnetic dipolarization signatures (Dewey et al. 2020). Furthermore, a pattern of X-ray emissions originating from this region were attributed to electrons impacting on the surface (Lindsay et al. 2016), later corroborated by observations of energetic electrons that could be mapped to the same location (Dewey et al. 2017). These bands of impacts on the surface are analogous to the auroral regions at Earth. The latitudinal center and extent of these bands vary considerably, most likely due to space weather conditions and appear to be mostly protons and electrons. In extreme cases, plasma accelerated toward the nightside surface may not be deflected at all and impact broadly on the surface there. The conditions under which this may happen are not fully understood, though there are several measures of the state of the magnetosphere which are part of the puzzle. The magnetic flux content of the magnetotail, which can be observed through the rise and fall in the lobe magnetic field strength, provides some evidence of mis-matched dayside and nightside reconnection rates (Slavin et al. 2021; Imber and Slavin 2017). Several signatures of magnetic reconnection are associated with magnetic dipolarizations (Sun et al. 2016; Dewey et al. 2017), suprathermal protons (Sun et al. 2017, 2018), the substorm current wedge (Poh et al. 2017) and fast plasma flows (Dewey et al. 2018). Regardless of how it is controlled, particle impact on the nightside (see Fig. 15 below) likely contributes to Mercury's exosphere most of the time, possibly significantly under some circumstances.

High solar wind pressures, especially during CMEs, can compress the magnetosphere. Due to Mercury's large internal iron core, variations in the solar wind pressure drive induction currents inside the planet core that act to increase the strength of the dipole field (Slavin et al. 2014). Increases of up to 30% of the magnetic dipole field have been observed during CME events where the dynamic pressure can reach up to $\sim$90 nPa in comparison to typical values of 10–15 nPa (Jia et al. 2019). This induction effect produces additional magnetic flux to the magnetosphere. In contrast, dayside magnetic reconnection acts to erode the magnetospheric flux. Therefore, the location of the magnetopause and subsequent size of the magnetosphere is the result of the balance between dayside magnetic reconnection and magnetic induction.

Models have been able to shed significant light on the system and reproduce some of the observed behavior. In general, two types of simulation models have been applied to study the global structure of the Hermean magnetosphere: magnetohydrodynamics (MHD), where both ions and electrons are considered as fluid, and hybrid model of plasma, where ions are treated as kinetic macro-particles and electrons are considered as a charge neutralizing fluid. These models have been used to study the Hermean magnetospheric response to the solar wind plasma and IMF configurations, and have found that the structure of the Hermean magnetosphere is highly dynamic and controlled by the upstream solar wind variations (e.g., Kabin et al. 2000; Ip and Kopp 2002; Kallio and Janhunen 2004; Trávnícek et al. 2007; Müller et al. 2012; Jia et al. 2015; Fatemi et al. 2018; Exner et al. 2018). In agreement with observations and theoretical investigations, both MHD and hybrid simulations have suggested that the magnetospheric cusps are the main channels where the solar wind plasma impacts on the surface at high latitudes of Mercury while the closed field lines at low latitudes considerably limit the access of plasma to the surface (Kabin et al. 2000; Ip and Kopp 2002; Kallio and Janhunen 2003; Massetti et al. 2007; Benna et al. 2010; Trávnícek et al. 2010; Schrijver et al. 2011; Richer et al. 2012; Varela et al. 2015; Hercík et al. 2016; Fatemi et al. 2020). Both of these fundamentally different numerical models have also suggested that the magnetic reconnection, especially during a southward oriented IMF, facilitates the access of plasma to the surface through magnetospheric cusps on the dayside, and to the mid- to high-latitudes on the nightside (e.g., Kallio and Janhunen 2003; Massetti et al. 2017; Mura et al. 2005; Richer et al. 2012; Varela et al. 2015; Hercík et al. 2016; Fatemi et al. 2020).

1.3 Lunar Space Environment

Because of the absence of global shielding by a thick atmosphere or by an intrinsic magnetic field of internal dynamo origin, the bulk of the lunar surface is directly exposed to the ambient space environment. The formation of the lunar exosphere is driven by incoming fluxes of mass and energy from space, including those of meteorites, photons, and charged particles, which will be discussed in Sects. 2–6 below. The bombardment by these drivers may not be homogeneous nor stable in time, with each driver exhibiting different spatial and temporal variabilities. Therefore, the lunar surface is very vulnerable to surface weathering processes, and in fact, the lunar surface is the best place to study the full range of space weathering effects in situ, because of its relatively easy access with spacecraft for detailed observations. The lunar surface might serve as a proxy for space weathering for the many planetary objects that are equally unprotected against space weathering, and which are only observed spectroscopically.

The influx of charged particles to the lunar surface is determined by the plasma surrounding the Moon. The Moon is exposed to plasma environments with very different plasma characteristics as it orbits around the Earth. While the Moon spends nearly three quarters of its orbit in the solar wind, the Moon is also exposed to the terrestrial magnetosheath and magnetotail plasmas. The solar wind (e.g., Marsch 2006) covers much of each lunation and is often thought of as one of the major drivers for the lunar exosphere. The solar wind is tremendously variable in all its properties even at 1 AU, with flow speeds of $\sim$250–1000 $\text{km}\,\text{s}^{-1}$, densities of $\sim$0.1–200 cm^{-3}, and ion and electron temperatures of $\sim$0.1–500 eV (Gosling et al. 1971; Crooker et al. 2000; Wilson et al. 2018). Some of the most extreme solar wind conditions are seen during coronal mass ejections, which typically have high speed and density but low temperature plasma, often surrounded by a hotter "sheath" Lepri and Zurbuchen (2004, 2010). These events can strongly alter the lunar environment, including the near-surface electrostatic characteristics (Farrell et al. 2012). The heavy ion content of the solar wind also varies tremendously during such events (Wurz et al. 2001, 2003), with potential implications for sputtering (Killen et al. 2012).

A notable subset of the upstream region is the terrestrial foreshock, which is the portion of the solar wind magnetically connected to the terrestrial bow shock and thus filled with ions and electrons back-streaming from the shock, which drive a variety of plasma waves (e.g., Eastwood et al. 2005). Downstream of the bow shock exists the magnetosheath (e.g., Lucek et al. 2005), which contains compressed, decelerated, deflected, and heated solar wind plasma. Though slowed, the magnetosheath flow typically remains supersonic at lunar distance since the shock is highly oblique in the flank. Around the full Moon, the Moon is located within the terrestrial magnetotail, in which tenuous plasmas of both solar wind and ionospheric origins are present, with energy spectra that can vary substantially depending on geomagnetic activities and on the Moon's position with respect to the terrestrial plasma sheet and tail lobes.

The incident charged particle fluxes can vary markedly between the dayside and nightside of the Moon. Much of the incoming plasma is absorbed and/or neutralized on the upstream side of the lunar surface (corresponding to the dayside in the solar wind and magnetosheath), resulting in the formation of a plasma void and wake structure downstream of the Moon (e.g., Halekas et al. 2015). Because of the release of photoelectrons, the lunar dayside charges up positively, to $<+20$ V, and on the lunar night side in the absence of the photons the surface charges up negatively because the plasma electrons from the tenuous plasma in the wake dominate the charging interaction with the surface (Stubbs et al. 2007). In the wake the surface potential is up -200 V (up to -600 V in the plasma sheet), forming a negative potential structure, thereby decelerating and partly reflecting the electrons directed to the surface (Halekas et al. 2005, 2008a, 2011). In general, ions in a supersonic flow do not have direct access to the near-Moon wake, though a variety of entry mechanisms are discussed (Nishino et al. 2009a, 2009b; Futaana et al. 2010, Dhanya et al. 2013, Halekas et al. 2014a). Thus, the nightside of the Moon is generally subject to much lower (but not completely zero) incident fluxes of ions and electrons compared with those on the dayside when the Moon, which is located in the solar wind and magnetosheath, as has been observed in energetic neutral atom reflection ratios (Vorburger et al. 2016). The situation is more complicated in the terrestrial magnetotail, where both sunward and anti-sunward flows commonly exist (Troshichev et al. 1999; Øieroset et al. 2002).

Additionally, the velocity distributions of impacting ions and electrons can be modified by local shielding effects of the crustal magnetic fields (e.g., Dyal et al. 1974) and by wave-particle interactions (e.g., Harada and Halekas 2016; Nakagawa 2016). As evident from orbital observations of enhanced fluxes of reflected electrons and ions (Anderson et al. 1975; Lue et al. 2011; Saito et al. 2010, 2012) and decreased fluxes of surface-scattered neutral atoms (Vorburger et al. 2012, 2013) above lunar magnetic anomalies, strongly magnetized areas of the lunar surface are shielded from some fraction of the incident particle fluxes, while proton fluxes may be enhanced in the surrounding regions by the solar wind deflection (Wieser et al. 2010; Futaana et al. 2013). Some observations suggest that the velocity distributions of downward-travelling particles are altered from those of the pristine ambient plasma by interactions with plasma waves in the near-Moon space (Halekas et al. 2012; Harada et al. 2014a, 2014b) and possibly with a shock driven by reflected protons (Halekas et al. 2014b). Details of electron and ion fluxes at the Moon are described in Sects. 5.3 and 6.6, respectively.

2 Thermal Release

2.1 Theoretical Description

Thermal desorption will be responsible for the release volatile species present on the surface into the exosphere. In that case the sublimation rate of the species at the prevailing temperature of the surface will determine the amount of released material, if the reservoir on the surface is not exhausted. Which species is volatile is determined by the surface temperature and the corresponding sublimation rate. For the sublimation flux, Φ_{th}, often the expression:

$$\Phi_{th} = \nu s(T) C_i \exp\left(\frac{-U}{k_B T}\right) \tag{1}$$

is used (Hunten et al. 1988), where $\nu \approx 10^{13}\ \mathrm{s}^{-1}$ is the assumed vibration frequency of a species at the surface, $s(T)$ is the total surface number density, C_i is the fraction of species i on the surface, U is the activation energy, k_B the Boltzmann constant, and T the surface temperature. Equation (1) is derived from the residence time, τ, of an adsorbate atom or molecule on a surface (Bernatowicz and Podosek 1991):

$$\tau = \frac{h}{k_B T} \exp\left(\frac{-U}{k_B T}\right) \tag{2}$$

with h the Planck constant. The vibration frequency of a species at the surface is $\nu = \frac{k_B T}{h}$ and is only a function of temperature in Eq. (2). For Mercury υ is in the range from $2.2 \cdot 10^{12}\ \mathrm{s}^{-1}$ to $1.5 \cdot 10^{13}\ \mathrm{s}^{-1}$, and for the Moon υ is in the range from $2.2 \cdot 10^{12}\ \mathrm{s}^{-1}$ to $9.4 \cdot 10^{12}\ \mathrm{s}^{-1}$. Moreover, all the energetics of the release is captured in the surface activation energy U. Unfortunately, Eq. (1) is a severe simplification of sublimation rate, and can be off by orders of magnitude. It is much better to use the measured sublimation data, which are given in the form

$$\ln(p_i) = A_0 + \sum_{j=1}^{n} \frac{A_j}{T^j}, \tag{3}$$

where p_i is the equilibrium vapor pressure of species i, at the temperature T, and the A_j are constants determined experimentally for a substance (e.g. Fray and Schmitt 2009).

Note that the sublimation data are mostly given for pure substances. If the amount of material to evaporate becomes less than a monolayer, the range of binding energies, also referred to as activation energies, to the underlying material has to be considered. If the binding energy changes, the ratio U/T in the exponential term changes (see Eq. (1)), resulting in significant change in the sublimation flux. The underlying surface material ideally is an atomically flat surface, but much more realistically the surface has steps, voids, cracks, defects, and other structures on the surface, which will have different activation energies, likely higher than for the pure substance. These different binding energies, or their range, are not known for any realistic planetary surfaces. Possible ranges for these binding energies (0.6–1.2 eV) have been simulated for solar wind implantation of H, its diffusion, and final release as H_2 from a surface (Farrell et al. 2007).

From the vapor pressure we get of the flux of released volatile species from the surface

$$\Phi_{th} = n_i \frac{1}{4} \sqrt{\frac{8 k_B T}{\pi m_i}} = \frac{p_i}{\sqrt{2\pi k_B T m_i}} \quad \text{with} \quad n_i = \frac{p_i}{k_B T} \tag{4}$$

where n_i is the corresponding number density of the exospheric species i at the surface.

Of course, the reservoir of volatile species on the surface must be able to support this sublimation flux, either by its volume, or by fluxes to the surface, via diffusion from below the surface and the return fluxes from the exosphere. If the sublimation flux cannot be supported, then the actual released volatile flux is source limited to whatever is available at the surface for sublimation. For example, all Ar is in the lunar exosphere on the dayside, but it condenses out on the lunar surface on the lunar nightside (Stern 1999). To maintain a constant Ar density in the lunar or hermean exosphere the Ar lost from the exosphere by escape and ionization has to be replenished by diffusion from the interior (Killen 2002).

Given the large range of surface temperatures on the Moon (Williams et al. 2017), and the even larger range on Mercury (Chase et al. 1976), governed by solar illumination on the dayside and radiation to cold space on the nightside, the thermal release is highly variable with local time. For a rocky body the day-side temperature follows a "1/4" law in a good approximation, with $T_{\max}$ the temperature at the sub-solar point and $T_{\min}$the night-side temperature all the way to the terminator. Thus, we can write the local surface temperature as

$$T_0(\phi,\theta) = \begin{cases} T_{\min} + (T_{\max} - T_{\min})(\cos\phi\cos\theta)^{1/4}, & \text{for } 0 < |\theta| < \frac{\pi}{2} \\ T_{\min}, & \text{for } \frac{\pi}{2} < |\theta| < \pi \end{cases} \tag{5}$$

with the longitude θ being measured from the planet-Sun axis and the latitude ϕ measured from the planetary equator. The simple "1/4" law, presented in Eq. (5), neglects the thermal inertia of the lithosphere and local albedo and emissivity variations. To determine the effective temperature at the subsolar point, $T_{\max}$, we use the Stefan–Boltzmann law for blackbody radiation to obtain

$$T_{\max} \approx T_{Sun}\left[\left(\frac{R_{Sun}}{R_{orb}}\right)^2 \frac{1-\alpha}{\varepsilon}\right]^{1/4} \tag{6}$$

where $T_{\max}$ is the effective temperature of the surface, R_{orb} is the distance to the Sun, R_{Sun} is the solar radius, $T_{Sun} \approx 5778$ K is the effective solar surface temperature, α is the bond albedo, with $\alpha_{Mercury} = 0.07$ (Mallama et al. 2002) and $\alpha_{Moon} = 0.14$ (Matthews 2008), and ε is the emissivity, with $\varepsilon_{Mercury} = 0.9$ (Murcray et al. 1970; Saari and Shorthill 1972; Hale and Hapke 2002) and $\varepsilon_{Moon} = 0.9$ (Gaidos et al. 2006).

Typical volatile species released thermally considered for the Moon (Stern 1999) and Mercury (Killen et al. 2007) are H, He, Ar, Ne, H_2, O_2, N_2, H_2O, OH, and CO_2. Some of these volatile species freeze out on the night side of the Moon and Mercury, like H_2O and CO_2 and are released again at dawn. Given the high temperatures at and near the sub-solar point also species like Na or K can be considered volatile.

Diffusion of volatile species to the surface that were trapped in solids, for example noble gases, will contribute to the available inventory of volatiles to be released into the exosphere. Probably H, H_2, He and Ne in the exosphere of the Moon and Mercury originate mostly from the solar wind being implanted into the surface material. Given the typical exposure of the surface to solar wind it will be saturated with solar wind material, which means that the implanted flux of ions matches the released flux of volatiles by diffusion. This was suggested for the Moon already a while ago (e.g., Hinton and Taeusch 1964; Johnson 1971; Hodges 1973, 1980). For example, assuming this scenario in a calculation the obtained H_2 density was 2100 cm^{-3} (Wurz et al. 2012), which was confirmed later by measurements from the LAMP UV spectrograph on the Lunar Reconnaissance Orbiter (Stern et al. 2013). A detailed study of the solar wind proton implantation into the regolith, the diffusion of H inside the regolith, possible chemical reactions of the H to form H_2 and OH, and the diffusion of these volatiles to the surface were presented by Tucker et al. (2019).

We assume a complete thermal accommodation of the sublimating volatile species with the local surface, thus a Maxwell-Boltzmann velocity distribution, $f(v)$, describes the release of sublimated particles.

$$f(v) = 4\pi \left(\frac{m}{2\pi k_B T}\right)^{\frac{3}{2}} v^2 e^{\frac{-mv^2}{2k_B T}} \tag{7}$$

The angular dependence is constant in azimuth angle and has the sine-dependence on the polar angle. For particles falling back to the surface and being re-released (no permanent sticking), the Maxwell-Boltzmann velocity distribution is also valid, even if the particles were initially released by a non-thermal process, because of the fast thermal accommodation at the surface (see Eq. (2)). The reason for the thermal accommodation is that the surface material is a fine-grained soil, regolith, with high porosity and particles sizes of 100 µm and less (Langevin 1997; Cooper et al. 2001), causing the particles to undergo multiple collisions with the highly structured regolith grains, making a thermal accommodation very likely.

One can use Gaussian deviates to sample the Maxwell-Boltzmann distribution for numerical analysis of exospheric particles, at a given temperature, i.e., the local surface temperature or at an elevated temperature. A set of three Gaussian deviates is needed to determine the components of a velocity vector for the thermal particle release at the surface. The Gaussian deviates, denoted G_i, are calculated by using the relation given in (Zelen and Severo 1965; Hodges 1973):

$$G_i = \sqrt{-2\ln(p_i)}\cos(2\pi q_i) \tag{8}$$

where p_i and q_i are uniform deviates for the three spatial directions, ranging between 0 and 1. The variance of each G_i is 1 (for $i = 1, 2, 3$). The initial velocity vector, $\vec{v}_0 = (v_1, v_2, v_3)$, at the start of the particle trajectory on the surface is

$$\vec{v}_0 = \sqrt{\frac{m}{k_B T_0}}\vec{G} + \vec{r} \times \vec{\Omega} \tag{9}$$

with particle mass m, the Boltzmann constant k_B, T_0 the main temperature of the released particle, $\vec{r}$ the release location on the surface, and $\vec{\Omega}$ the rotation vector of the planet. The particle velocity v_0 at the point of origin on the surface is $\sqrt{\vec{v}_0^{\,2}}$. The main temperature T_0 is taken either as local surface temperature at the particle release site or as characteristic temperature of the release process as discussed below.

Equation (4) assumes an infinite reservoir of the volatile material at the surface to support their sublimation. For Mercury and the Moon, the reservoir of volatiles on the surface is very limited, at least on the dayside, perhaps even less than a monolayer, thus the released flux from the surface is limited by fluxes of material to the surface. Most of the species released thermally will fall back onto the surface and thus return to the reservoir on the surface. Depending on species, the population of the surface reservoir is different, there are contributions by diffusion of volatiles from the interior (Killen 2002; Wurz et al. 2012), atoms being liberated from the mineral compound (Mura et al. 2009), and infall of volatile material, e.g. from comets (Stern 1999). Also, the sticking of these species on the surface, or the residence time of a volatile on the surface, must be considered. Details of the processing of volatile species between the exosphere, the surface, and the interior are presented by Grava et al. (2021) and will not be discussed further here.

2.2 Thermal Escape

Particles with thermal energies, the Maxwell-Boltzmann velocity distribution (Eq. (7)), rise in altitude against the gravitational force. Since there is no upper limit in velocity in the Maxwell-Boltzmann distribution, there will be a few particles that have initial energies that exceed the escape speed of the planet. The escape speed, v_∞, from the surface (assuming a surface-bound exosphere) is given by

$$v_\infty = \sqrt{\frac{2GM}{R}} \tag{10}$$

where G is the gravitational constant, M the mass of the planet, and R the radius of the planet. The most probable thermal speed is

$$v_0 = \sqrt{\frac{2k_BT}{m}} \tag{11}$$

where T is the temperature of the exospheric gas and m the mass of the species. To calculate the thermal escape (also called Jeans escape) we define the parameter X:

$$X = \left(\frac{v_\infty}{v_0}\right)^2 = \frac{2GM}{R}\frac{m}{2k_BT} = \frac{R}{H} \tag{12}$$

with H the scale height of the exospheric gas. The fraction of gas exceeding the escape speed is given by Lammer and Bauer (2004):

$$f_{esc} = \frac{1}{2\sqrt{\pi}}(1+X)\,e^{-X} \tag{13}$$

The smaller the value of X the larger the escape fraction f_{esc} will be. The rule of thumb is that for $X < 15$ the species is lost from the exosphere. For example, the escape of H from Titan's exosphere is close to hydrodynamic escape (Hedelt et al. 2010). From Eq. (13) we can calculate the flux of escaping particles for a species i

$$\phi_{esc,i} = \Phi_{th} f_{esc} = \frac{v_0}{2\sqrt{\pi}} n_i\,(1+X)\,e^{-X} \tag{14}$$

with n_i the number density of species i at the exobase. In the following we estimate the thermal escape for a few know volatile species on the Moon and Mercury.

Table 1 presents the X parameter (Eq. (12)), the escape fraction f_{esc} (Eq. (13)), the escape flux $\phi_{esc,i}$ (Eq. (14)), and the escaping mass flux for each of several volatile species considered for the exospheres of the Moon and Mercury (Stern 1999; Wurz et al. 2019). There are some significant differences between Mercury and the Moon: on Mercury only the light gases, up to ^{4}He, escape from the exosphere, whereas on the Moon there is significant escape even up to species as heavy as water. Heavier species will remain bound to their object, form permanent gases in the exosphere, if they do not condense at the night side or

Table 1 Thermal escape calculated for volatile species from the Moon and Mercury, with exospheric abundances at the surface from Stern (1999) and Wurz et al. (2019), respectively

Mercury

Species	H	H_2	^{3}He	^{4}He	OH	H_2O	Ne	N_2	O_2	Ar	CO_2
mass	1	2	3	4	17	18	20	28	32	40	44
n_i [m^{-3}]	2.29E+07	9.40E+12	2.95E+06	5.90E+09	1.40E+09	2.70E+11	6.00E+09	5.00E+09	1.6E+11	4.40E+10	4.0E+9
v_0 [m/s]	2995.90	2118.42	1729.68	1497.95	726.61	706.14	669.90	566.17	529.60	473.69	451.65
X	2.012	4.025	6.037	8.049	34.209	36.221	40.246	56.344	64.393	80.492	88.541
f_{esc}	1.14E-01	2.53E-02	4.74E-03	8.15E-04	1.38E-14	1.95E-15	3.87E-17	5.48E-24	2.00E-27	2.54E-34	8.91E-38
$\phi_{esc,i}$ [s^{-1}]	7.79E+09	5.04E+14	2.42E+07	7.21E+09	1.41E-02	3.72E-01	1.55E-04	1.55E-11	1.69E-13	5.29E-21	1.61E-25
$\phi_{esc,i}$ [kg/s]	2.08E+05	2.70E+10	1.94E+03	7.70E+05	6.39E-06	1.79E-04	8.31E-08	1.16E-14	1.45E-16	5.66E-24	1.89E-28

Moon

Species	H	H_2	^{3}He	^{4}He	CH_4	OH	H_2O	Ne	N_2	Ar	CO_2
mass	1	2	3	4	16	17	18	20	28	40	44
n_i [m^{-3}]	2.40E+07	9.00E+09	3.64E+06	7.27E+09	1.00E+10	1.60E+12	2.70E+11	1.00E+09	8.00E+08	1.00E+11	1.00E+09
v_0 [m/s]	2578.46	1823.24	1488.67	1289.23	644.61	625.37	607.75	576.56	487.28	408.20	388.72
X	0.848	1.697	2.545	3.394	13.575	14.423	15.272	16.969	23.756	33.853	37.331
f_{esc}	2.23E-01	1.39E-01	7.85E-02	4.16E-02	5.23E-06	2.37E-06	1.07E-06	2.17E-07	3.36E-10	1.95E-14	6.63E-16
$\phi_{esc,i}$ [s^{-1}]	1.38E+10	2.29E+12	4.25E+08	3.90E+11	3.37E+07	2.37E+09	1.76E+08	1.25E+05	1.31E+02	7.97E-01	2.58E-04
$\phi_{esc,i}$ [kg/s]	3.69E+05	1.22E+08	3.40E+04	4.17E+07	1.44E+04	1.08E+06	8.45E+04	6.67E+01	9.82E-02	8.52E-04	3.03E-07

in cold traps (like some permanently shadowed polar craters). Of course, all species are also subject to loss from the exosphere via photo-ionization and photo-dissociation.

With regards to the efficiency and type of thermal escape we have to look at the role of the X parameter (see Eq. (12)) in Eq. (13) in detail. Escape from an atmosphere is considered significant for situations where $X \lesssim 15$. Escape increases exponentially for smaller X, up to the point where the escape velocity equals the most probable velocity of the Maxwell-Boltzmann distribution at $X = 3/2$. For $X < 3/2$ the formalism presented above does not apply anymore, and for classical atmospheres escape would transition to hydrodynamic escape (often referred to as blow-off regime), with velocity distributions different from Maxwell-Boltzmann, being a shifted Maxwellian or a modified Maxwellian. The transition to the blow-off regime is not a step function at $X = 3/2$, but it is more gradual and becomes important already for $X < 2$–3 according to a study by Benedikt et al. (2000). According to Volkov et al. (2011) and Erkaev et al. (2015) the thermal escape regime changes to blow-off over a narrow range of the critical escape parameter X_{crit}: the escape is purely hydrodynamic for $X_{crit} \leq 2$–3, and for $X_{crit} \geq 6$ it is purely Jeans escape. Therefore, for Mercury and the Moon we can assume that for $X \lesssim 6$ any outgassed elements are lost immediately to space.

3 Micrometeorite Impact Vaporization

Micrometeorites impacting an unprotected planetary surface cause a range of processes including impact gardening, exospheric generation, surface contamination, and electrostatic effects on surface processes (Szalay et al. 2018). A global, direct consequence of the meteoroid bombardment is the formation of ejecta clouds of solids and gases. Escaping, unbound ejecta becomes a source of planetary or interplanetary meteoroids. We will focus on the contribution to the exosphere in the following.

Micrometeorite impacts on a solid rock or regolith surface result in an impact plume consisting of mostly surface material of broken fragments of minerals or rock, melt, all the way to atoms and molecules. Thus, with each impact, micrometeorites contribute to the production of exospheric densities, including also the low-volatile and refractory species. The details of the loss and source processes of volatiles and refractories in the exosphere are discussed by Grava et al. (2021). The steady flow of micrometeorites causes a steady contribution of particles to the exosphere. At quiet solar times, i.e., without energetic ions from the magnetosphere or the solar wind hitting the surface, it might dominate the particle release process acting over the whole planetary surface, at least for refractory species. During the night it may be the only particle release process acting over the whole planetary surface.

3.1 Theoretical Description

Since the impact of a micrometeorite on the surface creates an impact plume it is natural to model the volatile material of the plume by a thermal velocity distribution. The measured time-averaged temperature in the micrometeorite produced vapor cloud is in the range of 2500–5000 K (Eichhorn 1976, 1978a). Collette et al. (2013) reproduced the time-resolved measurements of dust impacts. Eichhorn (1978a, 1978b) studied the velocities of impact ejecta parameters during hypervelocity particle impacts and found that the velocity of the ejecta increases with increasing impact velocity and decreasing ejection angle, with the ejection angle measured with respect to the plane of the target surface, but the ratio of the maximum ejecta velocity to the primary impact velocity decreases with increasing impact speed.

At Mercury, impact plume temperatures are up to a factor ten higher than Mercury's dayside surface temperature. At the Moon, impact plume temperatures are even higher compared to dayside temperatures. However, the corresponding characteristic energies for micrometeorite impact are still lower than for particles that result from surface sputtering, see below.

For the simulation of trajectories for released particles that have their origin in micrometeorite vaporization a Maxwellian-Boltzmann velocity distribution, as described above (Eq. (7)), is used but with an average temperature of the released material of about 3000–4000 K (Wurz and Lammer 2003; Leblanc and Johnson 2013; Mangano et al. 2007; Gamborino et al. 2019).

The impact of micrometeorites and meteorites will evaporate a certain volume from the lunar or hermean surface, from rocks or from the regolith covered surface, to contribute to the exospheric gas at the impact site. Cintala (1992) calculated impacts for Mercury and the Moon and gave an analytical formula for the release of volatile material. The volume of surface material, V_v, being released into the vapor phase is given by

$$V_v = \frac{m_P}{\varrho_P}\left(c + d v_P + e v_P^2\right) = V_P\left(c + d v_P + e v_P^2\right) \tag{15}$$

where m_P is the projectile's mass, ϱ_P its mass density, V_P its volume, and v_P is the projectile's velocity. The constants c, d, and e are determined for the combination of surface material and projectile composition (Cintala 1992). Note that the released material is highly dependent on the composition and density of both the target and projectile, the heat capacities and enthalpies of melting and vaporization playing a large role. About one to two orders of magnitude more material than that of the impactor is released as vapor phase because of the high impact speed for meteorites at Mercury (Cintala 1992).

Alternatively, the impact of micrometeorites, all the way to large bolides, can be calculated from scaling laws (Holsapple 1993), which are based on a large experimental data set. The scaling laws apply from for impactor speeds from about 3 km/s upwards to much higher velocities (Holsapple and Housten 2020). The scaling laws provide the crater size, the mass of the excavated material, and the vapor mass, among much other data.

Having the volume of material released from the surface as volatiles for an impactor of mass m_P and velocity v_P of from Eq. (15) we can derive the total flux of particles released by micrometeorite impact. Using the formalism from Cintala (1992) we derive:

$$\Phi_{MIV} = \frac{\varrho_{surf}}{\langle\mu\rangle}\frac{1}{\varrho_P}\left(\frac{dm_P}{dAdt}\right)\left(c + d v_P + e v_P^2\right) \tag{16}$$

where ϱ_{surf} is the mass density of the surface material, $\langle\mu\rangle$ is the average atomic weight of the surface material, and $(dm_P/dAdt)$ is the mass flux of micrometeoritic bombardment on the surface. See Table 2 for typical values for the micrometeorite mass flux on Moon and Mercury. Note that the range of the micrometeorite mass fluxes cover a significant range, both for the Moon and Mercury, which has a direct influence on the contribution of this release process to the exosphere (see Eq. (16)).

3.2 Overview of Micrometeorite Fluxes at Mercury and Moon

For larger impacts, one can calculate the temporary contribution to the exosphere for a single impact using the scaling laws (Holsapple 1993), or Eq. (15) (Cintala 1992). Mangano et al. (2007) have shown such calculations where the impact plumes reach their maximum extent after about 1000 s in Mercury's exosphere.

Table 2 Survey of reported micrometeorite fluxes onto the surface of the Moon and Mercury

Object	MIV flux	Size range	Comments	Reference
Mercury	$2.82 \cdot 10^{-16}\ \mathrm{g\,cm^{-2}\,s^{-1}}$	$m < 0.1$ g Size range 5–100 µm	Modelling	Cintala (1992)
Mercury	10.7–23.0 t/day, corres. (1.66–3.56)$\cdot 10^{-16}\ \mathrm{g\,cm^{-2}\,s^{-1}}$	$m < 1$ g	Modelling, aphelion – perihelion	Müller et al. (2002)
Mercury	$2.9 \cdot 10^{-16}\ \mathrm{g\,cm^{-2}\,s^{-1}}$	Size range 10^{-8}–0.1 m		Bruno et al. (2007)
Mercury	$2.382 \cdot 10^{-14}\ \mathrm{g\,cm^{-2}\,s^{-1}}$	$m < 0.1$ g Size range 5–100 µm	Modelling	Borin et al. (2009)
Mercury	$8.982 \cdot 10^{-15}\ \mathrm{g\,cm^{-2}\,s^{-1}}$	$m < 0.1$ g Size range 5–100 µm	Modelling	Borin et al. (2010)
Mercury	12.6 ± 3.5 tons/day, corres. $(1.95 \pm 0.54) \cdot 10^{-16}\ \mathrm{g\,cm^{-2}\,s^{-1}}$	Diameters from 10 µm to 2000 µm	Modelling, averaged over Mercury's orbit	Pokorný et al. (2018)
Moon	$5.12 \cdot 10^{-17}\ \mathrm{g\,cm^{-2}\,s^{-1}}$	$m < 0.1$ g	Modelling	Cintala (1992)
Moon	2.7 t/day, corres. $8.36 \cdot 10^{-17}\ \mathrm{g\,cm^{-2}\,s^{-1}}$	Diameters from 10 nm to about 1 mm	Interplanetary meteorites	Grün et al. (2011)
Moon	1.4 t/day, corres. $4.27 \cdot 10^{-17}\ \mathrm{g\,cm^{-2}\,s^{-1}}$	Diameters from 10 µm to 2000 µm, depending on source populations	Modelling, averaged over lunar orbit	Pokorný et al. (2019)

Since larger impacts are very rare compared to the residence time of atoms and molecules in the exosphere, e.g. the impact frequency of 1-m meteoroids is only 2 events per Earth year on Mercury (Mangano et al. 2007), we are more interested in the steady contribution to the exosphere by the continuous flux of micro-meteorites. A survey of these fluxes is given in Table 2. More detailed information on the micrometeorite fluxes onto the Moon and Mercury is given in the accompanying paper (Janches et al. 2021).

Table summarizes observations of impacts rates on Mercury and the Moon. Each year the Moon is bombarded by about 10^6 kg of interplanetary micrometeoroids of cometary and asteroidal origin. For Mercury, the bombardment is about $(4-20)\cdot 10^6$ kg per year, although the meteoroid impact rates at very small distances from the Sun are not very well known (see also Table 2). Most of these projectiles range from 10 nm to about 1 mm in size and they impact the lunar surface at speeds of 10–72 km/s (Marchi et al. 2009). Some meteoroid populations are calculated to have higher energies (Pokorný et al. 2018), which is important since the vaporized volume is proportional to the square of the impact speed (see Eq. (15)). The mean impact velocity on Mercury is about 20 $\mathrm{km\,s^{-1}}$, and on the Moon it is about 14 $\mathrm{km\,s^{-1}}$ (Langevin 1997).

The impactors are delivering their kinetic energy to a point below the surface down to a depth comparable to the size of the impactor (Holsapple 1993). The total yield of excavated material, $Y = M_{ej}/M_{imp}$, from a hypervelocity impact (and the impact speed larger than the sound speed of the sample material) where M_{ej} is the total ejected mass created in an impact and M_{imp} is the impactor mass, can be anywhere from $Y = 10^3$ to 10^6 depending on the sample material properties. Impacts into solid rock result in lower yields and higher ejecta velocities than impacts into unconsolidated sand or powder (Housen et al. 1983; Hartmann 1985; Holsapple 1993).

Pokorný et al. (2018) developed a model that combined four distinctive sources of meteoroids in the solar system: main-belt asteroids, Jupiter-family comets, Halley-type comets, and Oort Cloud comets to characterize the meteoroid environment around Mercury. From this model of meteorite fluxes impinging on the surface they derived the contribution to the planet's exosphere. For Mercury's year they obtained good agreement with previously reported Ca observations in Mercury's exosphere by the MESSENGER spacecraft during the primary and first extended missions (March 2011–March 2013) (Burger et al. 2014).

3.3 Exospheric Escape via Mircometeorite Vaporization

Like the volatile species, also a fraction of the vaporized material from micrometeorite impact vaporization (MIV) will be lost from the exosphere. We can use the same formalism as for thermal escape to estimate the exospheric loss from MIV.

Table 3 presents the X parameter (Eq. (12)), the escape fraction f_{esc} (Eq. (13)), the escape flux $\phi_{esc,i}$ (Eq. (14)), and the escaping mass flux for several species released from the regolith via micro-meteorite impact vaporization. As discussed above, MIV is modelled as thermal release with temperatures of 3500 K. Exospheric abundances at the surface are taken from Wurz et al. (2010) for Mercury, and for low-Ti mare soils composition of the Moon from Wurz et al. (2007). Because of the high temperature of the vapor plume the X parameter is low, resulting in a larger fraction of escaping particles compared to thermal escape of volatiles. Moreover, there is a strong mass dependence, with a preferred loss of light species, and heavier species more likely to fall back onto the respective surfaces. As discussed above (Sect. 2.2), particles with $X_{crit} \leq 6$ will be immediately lost into space. For the Moon, because of the low gravity there, basically all species released by MIV are immediately lost into space, for Mercury only the species up to O are lost immediately, but a large fraction of the heavier elements returns to the surface. Thus, over geological time scales, there are chemical changes of Mercury's regolith resulting from MIV, but for the Moon these changes are much less. In addition, all species are subject to loss from the exosphere via photoionization and photo-dissociation, which has been discussed earlier (Wurz and Lammer 2003; Wurz et al. 2010).

3.4 Key Observations of Micrometeorite Impact Vaporization

Since the release processes are often operating at the same time, it is difficult to find observations of exospheric populations that can be solely attributed to micrometeorite bombardment. The estimates of the meteoritic flux range cover more than two decades (see Table 2) which directly scales the produced species in the exosphere (see Eq. (16)), making MIV possibly a dominating process or unimportant release process for a species, depending which meteorite flux is chosen for the data interpretation. In the following we give a few examples where this was possible or likely.

Kameda et al. (2009) studied the Na exosphere over a Mercury year via ground-based telescopic observations. Results of past observations have revealed that the atmospheric Na density has no or low correlation with the solar flux, sunspot number, heliocentric distance, or solar radiation pressure. Kameda et al. (2009) showed that the variability of Mercury's atmospheric Na density depends strongly on the IPD distribution. Since Mercury's orbit plane is inclined by 7° to the symmetry plane of the interplanetary dust particles (IPD) they found a corresponding temporal variability of the Na density in Mercury's atmosphere, that is, the Na density is low when Mercury is far away from the symmetry plane of IPDs and is high when Mercury is close to the symmetry plane. Actually, the authors could infer the IPD distribution near Mercury orbit from the temporal variability of Na density in Mercury's atmosphere. Exospheric Ca observed by MESSENGER could partly be explained by Mercury moving in and out the dusk disk (Killen and Hahn 2015).

Table 3 Thermal escape calculated for species from released from the Moon (low-Ti mare soils) and Mercury via micrometeorite impact vaporization, with exospheric abundances at the surface from Wurz et al. (2007) and Wurz et al. (2010), respectively

Mercury

Species	C	O	OH	Na	Mg	Al	Si	S	K	Ca	Ti	Fe
mass	12	16	17	23	24	27	28	32	39	40	48	56
n_i [m^{-3}]	3.87E+06	7.77E+07	8.84E+04	2.12E+06	2.50E+07	4.33E+06	2.95E+07	1.07E+06	7.61E+04	3.51E+06	3.07E+05	2.01E+06
v_0 [m/s]	2201.78	1906.79	1849.86	1590.38	1556.89	1467.85	1441.40	1348.31	1221.33	1205.96	1100.89	1019.22
X	3.726	4.967	5.278	7.141	7.451	8.383	8.693	9.935	12.108	12.419	14.902	17.386
f_{esc}	3.21E-02	1.17E-02	9.04E-03	1.82E-03	1.38E-03	6.06E-04	4.59E-04	1.49E-04	2.04E-05	1.53E-05	1.51E-06	1.46E-07
$\phi_{esc,i}$ [s^{-1}]	2.74E+08	1.74E+09	1.48E+06	6.13E+06	5.39E+07	3.85E+06	1.95E+07	2.16E+05	1.90E+03	6.48E+04	5.11E+02	2.99E+02
$\phi_{esc,i}$ [kg/s]	8.78E+04	7.42E+05	6.72E+02	3.77E+03	3.46E+04	2.78E+03	1.46E+04	1.84E+02	1.98E+00	6.92E+01	6.56E-01	4.48E-01

Moon

Species	O	Na	Mg	Al	Si	S	K	Ca	Ti	Cr	Mn	Fe
mass	16	23	24	27	28	32	39	40	48	52	55	56
n_i [m^{-3}]	1.52E+08	7.90E+05	1.54E+07	1.57E+07	5.06E+07	1.98E+06	1.98E+05	1.59E+07	2.52E+06	5.08E+05	3.30E+05	2.47E+07
v_0 [m/s]	1906.79	1590.38	1556.89	1467.85	1441.40	1348.31	1221.33	1205.96	1100.89	1057.70	1028.45	1019.22
X	1.551	2.230	2.327	2.618	2.715	3.103	3.782	3.879	4.654	5.042	5.333	5.430
f_{esc}	1.53E-01	9.80E-02	9.16E-02	7.45E-02	6.94E-02	5.20E-02	3.07E-02	2.85E-02	1.52E-02	1.10E-02	8.63E-03	7.95E-03
$\phi_{esc,i}$ [s^{-1}]	4.42E+10	1.23E+08	2.20E+09	1.72E+09	5.06E+09	1.39E+08	7.43E+06	5.46E+08	4.21E+07	5.92E+06	2.93E+06	2.00E+08
$\phi_{esc,i}$ [kg/s]	1.89E+07	7.57E+04	1.41E+06	1.24E+06	3.79E+06	1.19E+05	7.75E+03	5.83E+05	5.41E+04	8.22E+03	4.30E+03	3.00E+05

Optical spectroscopy measurements of Na in Mercury's exosphere near the subsolar point by MESSENGER Mercury Atmospheric and Surface Composition Spectrometer Ultraviolet and Visible Spectrometer, MASCS/UVVS (Cassidy et al. 2015). These observations have been interpreted Monte Carlo (MC) exosphere model (Wurz and Lammer 2003) to calculate the subsolar Na content of the exosphere for the observation conditions *ab initio*. The observed Na tangential column density profile as a function of altitude could be reproduced by the model using two components (Gamborino et al. 2019): i) below 500 km altitude, the dominant release mechanism of Na is thermal desorption with the local surface temperature of 594 K, and ii) at altitudes above the contribution by MIV prevails up to the observed 4000 km characterized by a temperature of about 3500 K.

However, one has to be careful with the interpretations of Na observations in Mercury's exosphere, because Na is released into the exosphere by all release processes considered (i.e., thermal release, PDS, sputtering, micrometeorite impact vaporization) and furthermore Na is affected by radiation acceleration, which explains a large fraction of the variability of the Na signal observed by ground-based telescopes (Potter et al. 2007). Usually, a mix of the release processes is occurring and the attribution of the Na signal, or a part of the Na signal, to a single release process is often difficult. The observations of Na and K at Mercury and the Moon, and their interpretation, are discussed in detail by Leblanc et al. (2022).

Burger et al. (2012, 2014) explained their Ca observations with the UVVS instrument on MESSENGER being the result of MIV. They observed very high temperatures of the Ca atoms of $>$ 50'000 K, which cannot be the direct result of meteoritic impact release of Ca atoms. The authors argue that the high energy might result from the CaO being released by MIV and dissociated into Ca and O atoms in the exosphere, but they admit that the excess energies of these species upon dissociation are not well understood (Burger et al. 2014).

Merkel et al. (2018) found good correlation between Mg observations in the exosphere with the Mg abundance in the terrain on the underlying surface being the result of MIV. They also observed high temperatures of the Mg atoms in the range between 5000 to 10 000 K, which cannot be the direct result of meteoritic impact release of the Mg atoms, using the same argument of MgO being the initial species released by MIV and the additional energy arises from the breakup into atomic constituents. From the regularity in the year-to-year variations, and no short time variations, they conclude that sputtering is an unimportant contributor at these latitudes, and MIV is the likely source for the observed Mg in the exosphere.

More information on the micrometeorite fluxes, and their temporal variation over the year, onto the surface of the Moon and Mercury is given in the accompanying paper (Janches et al. 2021).

4 Photon Stimulated Desorption

Photon Stimulated Desorption (PSD) has been discussed as a release process mostly for Na and K for the exospheres of Mercury and the Moon. Several processes promote Na and K into these exospheres, and it has been difficult to isolate the PSD release process from the other processes in the observations. Note, from laboratory experiments we know that PSD only releases atoms or molecules adsorbed on the surface, i.e., species which are not chemically bound within a mineral.

4.1 Mechanism of Photon Stimulated Desorption

Photon stimulated desorption (PSD) using photon energies just above the bandgap of the lunar and Mercury regolith surfaces can occur due to direct photon absorption and subsequent stimulated desorption of excited surface states. Typically, photon energies have to be

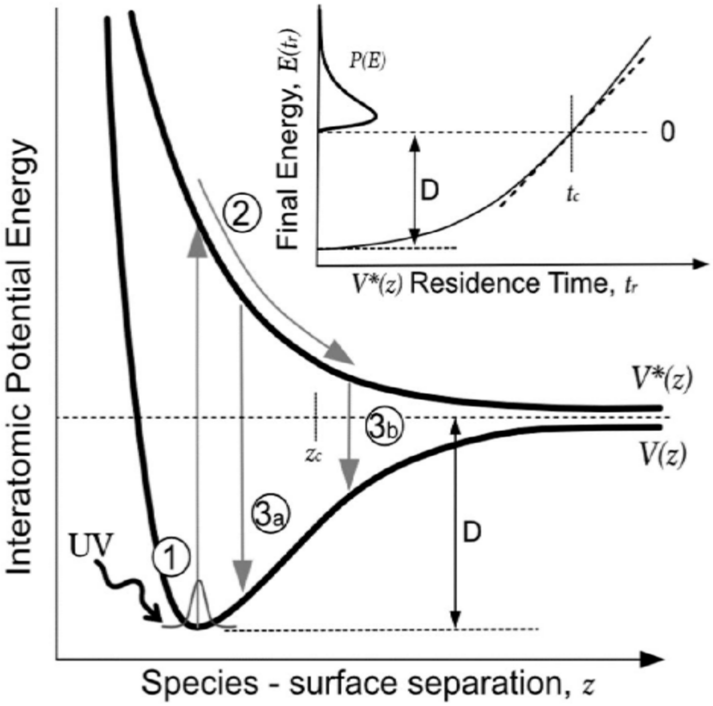

Fig. 4 The PSD processes can be explained by 1) a single-photon absorption and Frank-Condon transition of the surface species to a repulsive excited state potential $V^*(z)$, 2) motion of the excited species along the potential energy curve, and finally quenching of the excited state and either 3a) return to the ground state $V(z)$ or 3b) desorption. The inset shows the final $E(t_r)$ energy as a function of excited state resonance time, t_r. Figure reproduced from Schaible et al. (2020) with permission

in the range of about 4–10 eV. Photo-excitations invoke an electronic transition, which must be localized at the surface, leading to an anti-bonding state that results in the release of the excited atom (Na, K, …) or molecule (e.g. H_2O) from the surface, with non-thermal release energies of the desorbed species. For single centered excitons, self-trapping will occur at the surface mainly at defect sites with the ejection force primarily along the surface normal.

A qualitative diagram depicting the PSD process is shown in Fig. 4. PSD of neutral atoms or molecules residing on the surface of a substrate, often referred to as adatoms or molecules, is initiated by 1) a single photon excitation of a Franck-Condon transition from a ground state $V(z)$ to an excited surface state $V^*(z)$. As a result, 2) the excited atom or molecule gains kinetic energy by moving away from the surface along the excited state potential energy surface. The excited state is quenched and depending on the quenching rate, either 3a) the absorbed energy is dissipated and lost to the bulk or 3b) the displacement reaches a critical point z_c, corresponding to an excited state residence time t_c, which supplies sufficient kinetic energy to overcome the surface bond energy D and the atom or molecule desorb. The translation energy distribution of the desorbing atom(s) depend(s) upon the final energy and excited state residence time as shown in the inset of Fig. 4. The energy of the surface species after the excitation-quenching process is given by

$$E(t_r) = \frac{p(t_r)^2}{2m} + V(z(t_r)) \tag{17}$$

where $V(z)$ is the ground state potential energy curve and $p(t_r)$ is the momentum, which is determined by solving the classical equations of motion on the excited state potential $V^*(z)$. Though the potential energy surfaces are not generally known, the translational energy distribution can be approximated classically by evaluating the energy dependence on excited state residence time near t_c with a linear approximation (dotted line in inset of Fig. 4). This approximation holds for strongly quenched systems where the probability of the system remaining in the excited state beyond t_c decays exponentially (Zimmermann and Ho 1994).

4.2 PSD Velocity Distribution

Using the linear approximation for $E(t_r)$ near t_c and assuming the angular distribution of ejected particles is large compared to the detection cone for the velocity distribution, the velocity distributions for PSD of water can be approximated by a flux weighted Maxwellian of the form:

$$P_v(v, T_{trans}) = \left(\frac{m}{\langle E(t_r)\rangle}\right) v^3 \exp\left(\frac{-mv^2}{\langle E(t_r)\rangle}\right) \tag{18}$$

where v is the velocity, $\langle E(t_r)\rangle$ is the mean translation energy and m is the mass of the desorbing species. Note the temperature is related to the mean translation energy through $\langle E(t_r)\rangle = 2k_B T_{trans}$, where k_B is the Boltzmann constant, and T_{trans} is the apparent translation temperature of the distribution that results from a convolution of the surface temperature and the repulsive potential of the desorbing electronic state (see Fig. 4). Experimental data for H_2O desorption can be fit using this form with a bi-modal distribution consisting of a low temperature thermal component (matching the substrate temperature) and a high temperature 'suprathermal' component due to direct desorption along the normal component (Bennett et al. 2016; DeSimone and Orlando 2014; Zimmermann and Ho 1994; Schaible et al. 2020). Since this distribution function includes the intrinsic physics of the desorption process, this is often used as an experimental fitting procedure in addition to the Weibull distributions discussed below.

One of the few experimental results in the laboratory studying the Na release processes happening on regolith surfaces are the experiments by Yakshinskiy and Madey (2000, 2004), which are relevant for the Moon and Mercury. These authors studied the desorption induced by electronic transitions (DIET) of Na adsorbed on model mineral surfaces and lunar basalt samples, where the laboratory experiments included PSD and Electron-Stimulated Desorption (ESD) as release processes. In particular, they measured velocity distribution functions (VDF) of Na released via ESD from SiO_2 surfaces and found it to be "clearly non-thermal" with respect to the surface temperature, somewhat resembling a Maxwell-Boltzmann distribution at 1200 K, but with a high-energy tail and a positive offset above zero for the lowest velocities. Thus, Eq. (18) derived for PSD measurements of water cannot be used here. A range of distributions, thermal and non-thermal, have been used in the literature to model the particle release by PSD. However, none of these distributions replicates all the features as they are observed in the laboratory experiments: i) non-thermal distribution peaking at energies much higher than the surface temperature, ii) a high energy tail extending to speeds beyond what is possible from non-thermal Maxwell-Boltzmann distributions, iii) an offset in velocity so that there is a minimum release velocity. The details of this have been reviewed by Gamborino et al. (2019).

Gamborino et al. (2019) presented an improved VDF for the PSD process satisfying the mentioned features from the observations. To mathematically best describe the published laboratory measurements (Yakshinskiy and Madey 2000, 2004) and planetary observations (e.g. Cassidy et al. 2015) the sought-after VDF has to have a characteristic energy significantly higher than what corresponds to the surface temperature and that tails towards higher speeds. The second goal of the sought-after VDF is a parametrization that allows for its applications at other surface temperatures than the measured ones in the laboratory, in particular for the surfaces of Mercury and the Moon.

Gamborino et al. (2019) presented an empirical energy distribution function, for PSD at Mercury and the Moon, namely the Weibull distribution, which allows for a wide range of shapes using only two parameters for its definition. The normalized Weibull distribution for the random variable υ is defined as:

$$f\left(\upsilon;\lambda,\kappa\right)=\begin{cases}\frac{\kappa}{\lambda}\left(\frac{\nu}{\lambda}\right)^{\kappa-1}e^{-(\nu/\lambda)^{\kappa}} & :\nu\geq 0\\ 0 & :\nu<0\end{cases}$$

where κ is the dimensionless shape parameter and $\lambda > 0$ is the scale parameter of the distribution (in m/s). The scale parameter λ is obtained after calculating the mean of the probability distribution function (first central moment):

$$\overline{\nu}=\int_{-\infty}^{+\infty}\nu f\left(\upsilon;\lambda,\kappa\right)d\nu=\int_{0}^{+\infty}\nu\frac{\kappa}{\lambda}\left(\frac{\nu}{\lambda}\right)^{\kappa-1}e^{-(\nu/\lambda)^{\kappa}}d\nu=\lambda\Gamma\left(1+\frac{1}{\kappa}\right) \tag{19}$$

with Γ the Gamma function. The surface, which is the starting point of the desorbed atoms, has a given temperature T_S. This surface temperature will cause an energy broadening of the electronic transition induced by the adsorption of the UV photon (Gamborino et al. 2019). Therefore, the related kinetic energy of the desorbed atom of $\frac{1}{2}m\overline{\upsilon}^2=\frac{3}{2}k_BT_S$ folds into the Weibull distribution. Since we consider the one-dimensional case, we have

$$\overline{\upsilon}=\sqrt{\frac{3k_BT_S}{m}}$$

with m being the mass of the desorbed atom. Thus, we get for the scale parameter the expression:

$$\lambda=\frac{\overline{\upsilon}}{\Gamma\left(1+\frac{1}{\kappa}\right)}=\sqrt{\frac{3k_BT_S}{m}}\frac{1}{\Gamma\left(1+\frac{1}{\kappa}\right)} \tag{20}$$

The normalized Weibull distribution is then:

$$\begin{aligned}f\left(\upsilon,\upsilon_{0,}\kappa\right)=\kappa\Gamma\left(1+\frac{1}{\kappa}\right)\left(\frac{m}{3k_BT_S}\right)^{\frac{1}{2}}\left(\left(\upsilon-\upsilon_0\right)\sqrt{\frac{m}{3k_BT_S}}\Gamma\left(1+\frac{1}{\kappa}\right)\right)^{\kappa-1}\times\\ \times\exp\left(-\left(\left(\upsilon-\upsilon_0\right)\sqrt{\frac{m}{3k_BT_S}}\Gamma\left(1+\frac{1}{\kappa}\right)\right)^{\kappa}\right)\end{aligned} \tag{21}$$

where υ_0 is the offset speed, and κ is the shape parameter, which is an implicit function that is usually determined by numerical means (see Bhattacharya and Bhattacharjee 2010). υ_0 and κ are the only free parameters for this velocity distribution, λ is derived from Eq. (21) using the actual the surface temperature T_S, with the best fits calculated for all available experimental data sets with a single set of parameters using $\kappa = 1.7$ and $\upsilon_0 = 575$ m/s. Even though the Weibull distribution with the given parameters is currently the best available presentation of the velocity distribution for PSD, it is based on little data from laboratory studies.

4.3 Released Particle Flux by PSD

We can calculate the flux of released atoms from a surface by photon-stimulated desorption of Na atoms Φ_{PSD} for a species i from

$$\Phi_{PSD,i}=f_iN_S\int\phi_{ph}\left(\lambda\right)Q_i\left(\lambda\right)d\lambda\approx\frac{1}{4}f_iN_S\phi_{ph}Q_i \tag{22}$$

where f_i is the fraction of species, N_S is the surface density of the regolith, $\phi_{ph}(\lambda)$ is the incident photon flux, $Q_i(\lambda)$ is the PSD cross section, the factor 1/4 gives the surface-averaged value. The regolith surface density is estimated as $N_S = 7.5 \cdot 10^{14}$ cm−2, and the average photon flux at 1 AU is $\phi_{ph} \approx 2 \cdot 10^{15}\ \text{cm}^{-2}\,\text{s}^{-1}$ for the relevant UV wavelength range, as discussed below.

PSD with solar photons is an important low-energy release process when sufficient UV flux is present and free Na or K is available on the surface. For Mercury and the Moon only Na and K have significant release rates due to PSD. The experimentally determined PSD cross-section for Na is $Q_i = (3 \pm 1) \times 10^{-20}\ \text{cm}^2$ in the wavelength range of 400–250 nm (Yakshinskiy and Madey 2000), and for K it is $Q_i = 2 \cdot 10^{-20}\ \text{cm}^2$ (Madey et al. 1998). Note that these cross sections are for Na and K atoms physically bound on a mineral surface, i.e., already freed from the mineral bonds because solar photons lack sufficient energy to release alkaline earth atoms from minerals. Direct PSD of Na or K from minerals has not been observed in laboratory experiments (Yakshinskiy and Madey 2004; Bennett et al. 2013). Thus, neither PSD nor thermal release are primary release mechanisms, meaning that they cannot eject the Na or K atoms that are still bound in the mineral of the rock.

4.4 Exospheric Escape via Photon-Stimulated Desorption

Figure 5, left panel, shows the PSD velocity distribution (Eq. (21)) for Na and K for a surface temperature of 540 K, the case for the sub-solar point Mercury near apocenter. The distribution for the Moon looks similar to the one for Mercury, since the surface temperature only has small effect on the VDF (see Eq. (24)). The VDF for PSD is clearly non-thermal, and it is tailed toward higher velocities. For calculating the escape, we need to estimate the part of the VDF above the escape speed, υ_∞, which is easily done numerically. Figure 5, right panel, shows the cumulative function of the PSD velocity distribution for Na and K, which tends to 1 because the function is normalized. The escape fraction is then 1 minus the cumulative function evaluated at the escape speed, υ_∞, which is also shown in Fig. 5, right panel. For Mercury $\upsilon_\infty = 4250\ \text{m}\,\text{s}^{-1}$ and for the Moon $\upsilon_\infty = 2375\ \text{m}\,\text{s}^{-1}$. This means the escape fraction for Mercury for PSD is below 10^{-3} and for the Moon it is below 10^{-2}. Thus, for a PSD process of Na and K, photoionization is the dominating loss process from the exosphere for both objects.

However, there is radiation pressure acting on the Na and K atoms in the exosphere that accelerate these atoms away from the Sun, resulting in non-Keplerian particle trajectories, thus complicating the situation. Simulations by Schmidt et al. (2012) demonstrate that both photon-stimulated desorption and micrometeoroid impacts can result in an about 20% loss of Mercury's sodium atmosphere, depending on Mercury's orbital phase, and together the two release processes are responsible for the observed comet-like tail as driven by solar radiation pressure.

4.5 Experimental Observations of PSD

In the laboratory, the experiments by Madey et al. (1998) and Yakshinskiy and Madey (1999, 2000, 2004) have been fundamental to the understanding of the PSD release process for Mercury and the Moon. These authors deposited Na or K atoms onto SiO_2 surfaces and lunar basalt and measured the PSD cross sections, the temperature dependence, and the velocity distribution of released Na and K atoms. Among other things, they clearly demonstrated that PSD is a non-thermal process, the desorption of an alkali atom is the result of an electronic excitation resulting from the absorption of a UV photon at the surface.

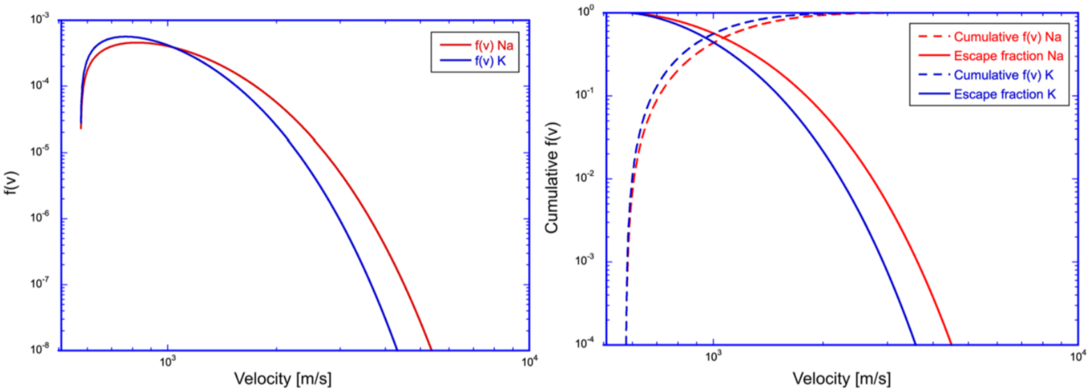

Fig. 5 Left: PSD velocity distribution for Na (red line) and K (blue line). Right: Cumulative velocity distribution for Na (dashed red line) and K (dashed blue line), and escape fraction for Na (red line) and K (blue line)

Bennett et al. (2016) studied PSD of Ca from CaS powder samples, with CaS considered as an analogue material for oldhamite ((Mg,Ca)S), which the authors considered to be a possible component of the Mercury surface, particularly within the hollows identified within craters, and could therefore serve as a source of the observed exospheric calcium of Mercury. They measured cross sections for PSD using 3.4 eV photons for neutral Ca as $Q_i(\mathrm{Ca}^0) = (1.1 \pm 0.7) \cdot 10^{-20}\ \mathrm{cm}^2$ and for ionized Ca as $Q_i(\mathrm{Ca}^+) = (3.2 \pm 0.9) \cdot 10^{-24}\ \mathrm{cm}^2$. They also observed non-thermal velocity distributions for Ca, which they fitted with a sum of two Maxwell-Boltzmann distributions, that support PSD as the release process. Therefore, for interpreting Ca observations in the exosphere also PSD must be considered, at least at provinces with a significant oldhamite fraction on the surface.

Schaible et al. (2020) studied PSD of S from powder samples of MgS. They measured cross sections for PSD using 6.42 eV photons for neutral S^0 as $Q_i = 4 \cdot 10^{-22}\ \mathrm{cm}^2$. Also these authors observed non-thermal velocity distributions for the released S atoms, which they fitted with a sum of two Maxwell-Boltzmann distributions, that support PSD as the release process. Although the MgS (niningerite) used in these experiments is not considered the major sulfur-bearing mineral of Mercury's surface, but is considered similar to sulfur-bearing minerals such as CaS (oldhamite) and FeS (troilite) that were considered for Mercury's surface (Wurz et al. 2010; Nittler and Weider 2019).

The process of photon-stimulated desorption (PSD) has been considered for generating Na and K exospheric species as measured at Mercury and the Moon, when the flux of solar photons is high, e.g. on the dayside. However, since the release processes compete with each other it is often not easy to assign an observation to a single release process. For PSD it is clear that the maximum of the released flux should be located at the sub-solar point. However, since thermal release has also its maximum there, there is a direct competition and since fluxes from evaporation are much higher for Na and K for the temperatures at the sub-solar point of Mercury and the Moon, thermal release wins over PSD there. Since evaporation is an exponential function of the surface temperature (see Sect. 2.1), its importance drops fast for larger solar zenith angles (SZA) and PSD becomes important since it scales only with the cosine of the SZA when going towards higher latitudes. However, the activation energy for thermal release will increase for sub-monolayer coverages of Na and K on the surface, as discussed above. At least for Mercury, higher latitudes are where the solar wind ions have access to the surface because of the structure of its magnetosphere sputtering is contributing to the exospheric particle populations. Thus, the source process of Na and K in the hermean exosphere must be investigated carefully for each observation. The situation is less complicated at the Moon because of the lack of a lunar magnetosphere. For example, Sarantos et al. (2008) have concluded that PSD is responsible for the observed Na in the lunar exosphere when the Moon is in the solar wind.

Although of lesser importance for the exospheres of Mercury and the Moon, there is release of H_2O via PSD, and laboratory work on the PSD of water molecules from lunar surface material has also been reported (DeSimone and Orlando 2014, 2015). PSD of H_2O ($\nu = 0$) and O ($^3P_{J=2,1,0}$) was measured with resonance-enhanced multiphoton ionization following 157-nm photon irradiation of adsorbed water on a lunar mare basalt or an impact melt breccia. Water removal cross sections and time-of-flight (TOF) distributions were measured at exposures between 0.1 and 10 Langmuir ($1\ \text{L} = 1.33 \cdot 10^{-6}$ mbar s). The average cross section for H_2O ($\nu = 0$) removal and destruction at 0.1 Langmuir H_2O exposure was measured to be $(7.1 \pm 1.9) \cdot 10^{-19}\ \text{cm}^2$ and then decreased with increasing coverage. The cross sections were similar for lunar impact melt breccias and mare basalt samples. Additionally, non-resonant ionization was employed to detect photofragments of vibrationally excited H_2O. The OH^+ fragment of H_2O (ν^*) and the $O(^3P_J)$ photoproducts increased in intensity during prolonged irradiation as hydroxyl groups accumulated on the surface and then recombined. The formation of excited water molecules via this process simulates the probable water formation during localized meteoroid impact events. For an initial exposure of 5 L H_2O, after reaching maximum signal, the cross sections for H_2O (ν^*) and $O(^3P_2)$ depletion were measured to be $1.2 \cdot 10^{-19}\ \text{cm}^2$ and $6.7 \cdot 10^{-20}\ \text{cm}^2$, respectively. These photo-desorption, photo-destruction and photo-formation cross sections are relatively high and indicate that surficial water will not persist in Sun-lit regions of Mercury and the Moon unless a persistent source term exists. More discussion on the formation of H_2O, its distribution and migration over the planet, and its contribution to the exosphere are given in (Schörghofer et al. 2021).

4.6 Photon Fluxes at Mercury and the Moon

The Sun emits a continuous flux of photons (i.e., the solar spectrum), where most energy is contained in the visible (VIS), the infrared (IR), and the ultraviolet (UV) energy range, with relatively small additions in the X-ray and the gamma-ray region. Figure 6 shows the solar spectrum as measured by the SOLar SPECtrometer (SOLSPEC) instrument, part of the SOLAR payload on board the International Space Station (Meftah et al. 2018). The total solar power received at Earth, also referred to as the total solar irradiance (TSI), is on average $1360.96\ \text{W}\,\text{m}^{-2}$.

The total solar power received at Earth, also referred to as the total solar irradiance (TSI), follows closely the Sun's 11-year Schwabe cycle (Fröhlich 2013), as is clearly evident in Fig. 7, with minimum and maximum values of $1357.08\ \text{W}\,\text{m}^{-2}$ and $1363.25\ \text{W}\,\text{m}^{-2}$, respectively. Thus, the TSI variation with solar cycle is small compared to the absolute value ($<1\%$). Integrating over the solar photon spectrum, the TSI average value of $1360.96\ \text{W}\,\text{m}^{-2}$ corresponds to a total photon flux of $6 \cdot 10^{17}\ \text{cm}^{-2}\,\text{s}^{-1}$, at solar minimum to a flux of $5.99 \cdot 10^{17}\ \text{cm}^{-2}\,\text{s}^{-1}$, and at solar maximum to a flux of $6.01 \cdot 10^{17}\ \text{cm}^{-2}\,\text{s}^{-1}$.

Since the absorbed photon must overcome the binding energy of an atom on the surface there is a minimal necessary photon energy for the release via PSD (see discussion in Sect 4.1). Yakshinskiy and Madey (1999) found that only photons with energies larger than about 4 eV are capable of inducing PSD of Na atoms from surfaces that simulate lunar silicates, as discussed in Sect. 4.1. It is thus only the part of the solar spectrum with $\lambda < 300$ nm that is relevant for PSD. Of all solar photons available only a photon flux of about $\phi_{ph} = 2 \cdot 10^{15}\ \text{cm}^{-2}\,\text{s}^{-1}$ exhibits energies larger than 4 eV (see also the blue arrow in Fig. 6).

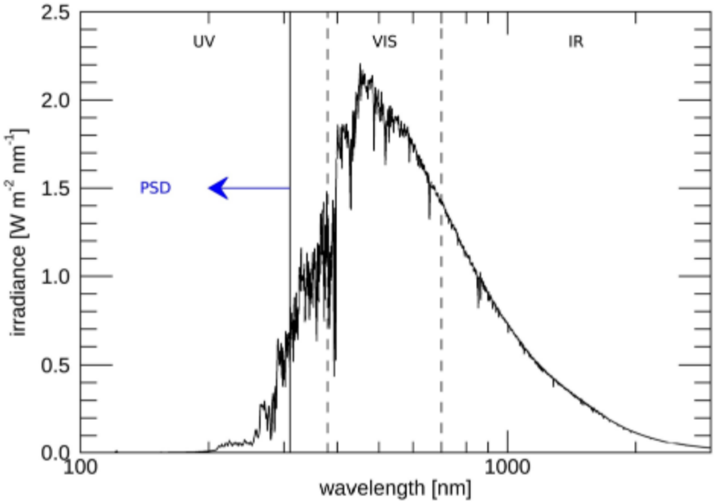

Fig. 6 The solar spectrum as measured by SOLSPEC on board the ISS (Meftah et al. 2018). The wavelength range in the UV that contributes to PSD is indicated

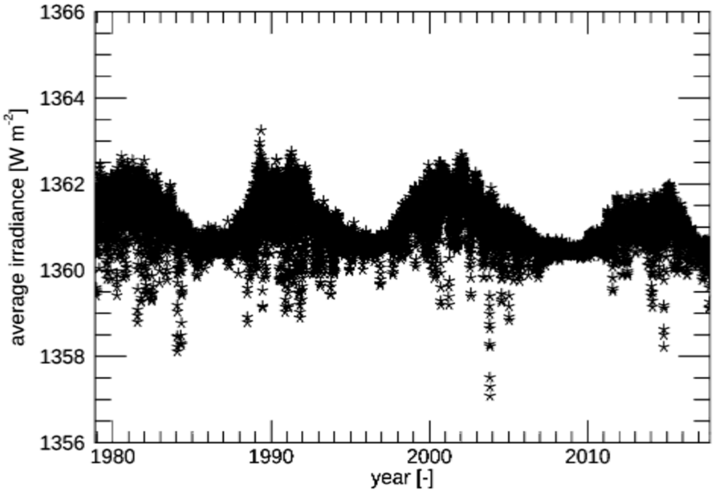

Fig. 7 TSI variation from 1979 until 2017, based on Fröhlich (2013). Data are obtained from PMOD/WRC, Davos, Switzerland, of the updated dataset version 42_65_1709 with new data from the VIRGO Experiment on the cooperative ESA/NASA Mission SoHO

The TSI values measured by SOLSPEC and presented above are valid for a Sun distance of 1 AU (where AU is the astronomical unit, about $1.5 \cdot 10^{11}$ m). As the photon flux expands into space it decreases with $1/R^2$, where R is the distance to the Sun. To determine the flux at the Moon and Mercury, one thus has to factor in these bodies' distances from the Sun.

The Moon's distance to the Sun is close to 1 AU, i.e., the average flux of photons with energies $>$4 eV at the Moon is close to the $2 \cdot 10^{15}$ cm^{-2} s^{-1} mentioned above. As Earth (and the Moon) orbit the Sun, the Moon's distance to the Sun varies by $\sim 6 \cdot 10^9$ m, introducing a photon flux variation of $\sim 1.5 \cdot 10^{14}$ cm^{-2} s^{-1}. This variation is relatively small (7.5%) compared to the total photon flux of $2 \cdot 10^{15}$ cm^{-2} s^{-1}.

Mercury, being located at a solar distance of $(4.60–6.98) \cdot 10^9$ m, is much closer to the Sun, resulting in Mercury receiving a much higher photon flux than the Moon. On average, the total flux of photons with energies $>$4 eV at Mercury amounts to $1.34 \cdot 10^{16}$ cm^{-2} s^{-1}, i.e., almost 10 times the photon flux the Moon receives. With Mercury's orbit being quite eccentric, the variation in the photon flux due to the variation in distance between Mercury and the Sun is quite substantial. During one Mercury year, the PSD-relevant solar photon flux (with $E > 4$ eV) varies from $9.2 \cdot 10^{15}$ cm^{-2} s^{-1} at aphelion to $2.12 \cdot 10^{16}$ cm^{-2} s^{-1} at perihelion, i.e., the variation is of the same order as the total photon flux itself. For the Moon, the PSD-relevant solar photon flux (with $E > 4$ eV) varies from $1.93 \cdot 10^{15}$ cm^{-2} s^{-1} at aphelion to $2.08 \cdot 10^{15}$ cm^{-2} s^{-1} at perihelion.

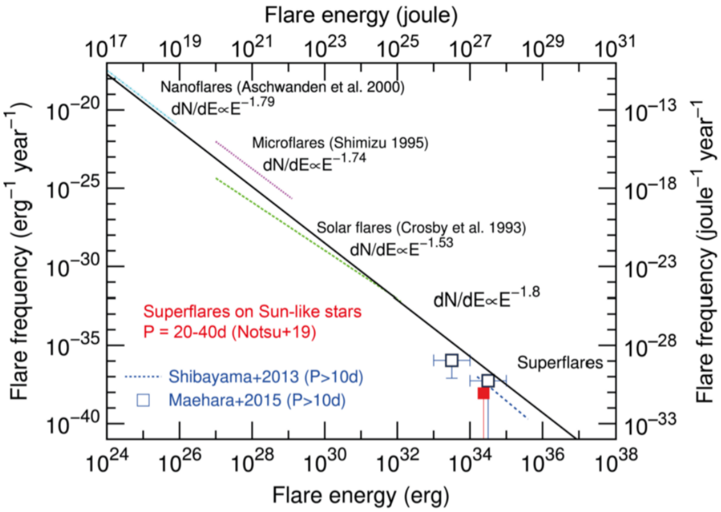

Fig. 8 The figure illustrates various frequency distributions for so-called nano-, micro- and normal solar flares, but also for different types of stellar flares. Figure is adapted from Notsu et al. (2019) with permission

The Sun's photon flux only reaches the sunlit hemisphere of a planetary body and, at the surface, its irradiance scales with the cosine of the zenith angle. The variation in photon flux from the equator to the terminator is thus substantial. On the microscopic scale of individual regolith grains, the variation of the solar irradiance will probably be even larger.

4.7 Fluxes from Solar and Stellar Flares

Flares are energetic events on the Sun and on other stars that are generated when magnetic energy is released through a sudden rearrangement of stressed magnetic field lines on active regions on the star (see e.g. Benz and Güdel 2010; Fletcher et al. 2011; Hudson et al. 2011; Shibata and Magara 2011; Benz 2017 for comprehensive reviews on flares and their underlying physics). When happening, charged particles are accelerated toward the lower solar atmosphere, where they heat the plasma and generate a broad range of intense electromagnetic radiation, ranging from gamma rays to hard and soft X-rays, to UV and optical wavelengths, and up to the radio spectrum. Over their duration of tens of minutes, flares on the Sun were observed to release a total energy of up to 10^{25} J (Emslie et al. 2005, 2012; Moore et al. 2014), and even more on extremely rare occasions (Schrijver et al. 2012) such as the famous Carrington event in 1859 (Carrington 1859).

The occurrence rate of flares decreases with increasing total energy, with flares of the largest energies generally occurring only at solar maximum, and even then less than once a year (e.g., Benz and Güdel 2010). The frequency distribution of flares can be described as a power law function of E_f as $N\left(E_f\right) dE_f \propto E_f^{\alpha} dE_f$, where dE_f is the respective energy range, and α is the number of flares per time within dE_f. For instance, Schrijver et al. (2012) found a value of $\alpha = -2.3 \pm 0.2$, and $N\left(E_f\right)$ and a break in the frequency spectrum for energies above $\sim 10^{25}$ J. Figure 8 illustrates different flare frequencies, including some from stellar flares (see below).

Flares are categorized by observations of the peak brightness in the X-ray range through the NOAA/GOES definition by letters from A ($<10^{-7}$ $\mathrm{W\,m^{-2}}$), B (10^{-7}–10^{-6} $\mathrm{W\,m^{-2}}$), C (10^{-6}–10^{-5} $\mathrm{W\,m^{-2}}$), M (10^{-5}–10^{-4} $\mathrm{W\,m^{-2}}$) to X ($>10^{-4}$ $\mathrm{W\,m^{-2}}$) followed by numbers from 1 to 9.9, specifying the peak intensity within each range (e.g., Fletcher et al. 2011; Schrijver et al. 2012). They are partitioned into two distinct phases, the impulsive phase, and the gradual phase. The impulsive phase is the initial explosive release of energy mainly characterized by the hard X-ray (HXR; below ∼0.1 nm) enhancement, which generally lasts for a few minutes, while the gradual phase peaks shortly after the impulsive phase in soft X-ray (SXR; $\sim$0.1–10 nm) and Hα emission and then gradually declines within up to several hours The impulsive phase is accompanied by strong enhancements in the continuum emission of UV and EUV. Observations of the respective UV continuum of solar flares between 100 and 300 nm—the relevant wavelength range for PSD, however, are surprisingly rare but do exist (e.g., Dominique et al. 2018).

The highest irradiation for flares can be found in the short wavelengths with flux enhancements of over 5 orders of magnitude during flares, while for $\lambda \sim 27$–120 nm it can still be as high as a factor of 100 during the impulsive phase for a few transition region emissions, but only up to a factor of 2 for the gradual phase (e.g., Woods et al. 2004, 2005, 2006). The longer wavelengths generally show lower variations, with the EUV (27–120 nm) and FUV (120–195 nm) having low to very low variations (Woods et al. 2004, 2006). For the X17 flare investigated by Woods et al. (2004), for instance, the EUV and FUV ranges only contribute to the change in total solar irradiance (TSI) by 1.4% and 2.3%, respectively. Woods et al. (2006) further found that for four X-class flares with a total energy of about 10^{25} J each, about 50% of the change in the total TSI is related to flux enhancements above 200 nm in the NUV, optical and infrared (Woods et al. 2006), which was later confirmed by, e.g., Warmuth and Mann (2016). For so-called white light flares that are visible in the optical Kretzschmar (2011) found that wavelengths below 50 nm only contribute between 10% and 20%, while the visible and NUV constitute the bulk of the released flare energy. However, an important part of this energy release might come from $\lambda > 300$ nm, since an increase of the emission from the Balmer continuum at 350 nm by a factor of 2.3 to 5.5 was measured during an X-class flare (Kotrč et al. 2016). The NUV wavelength range is the most relevant for PSD, thus only moderate increases in the PSD releases are expected as a direct result of flares.

Chamberlin et al. (2018) investigated the fluxes from solar flares during the intense September 2017 storm period and compared the radiation from the quiet Sun with the emission from several flares for $\lambda < 190$ nm. They did not find a strong increase for the UV from about 150 nm up to 190 nm. Heinzel and Kleint (2014) were the first to measure the increase in the Balmer continuum during a white-light flare between $\lambda \sim 280$–300 nm and found an enhancement of the observed X1 flare by 100%–200%. The first detection of a solar flare emission in the MUV around 200 nm was finally reported by Dominique et al. (2018), who found an insignificant increase at 190–220 nm of only 0.35% from $6.901 \cdot 10^{-5}\ \mathrm{J\,s^{-1}\,cm^{-1}}$ to $6.926 \cdot 10^{-5}\ \mathrm{J\,s^{-1}\,cm^{-1}}$. Similarly, the Lyman α emission only increased by 0.97%. Figure 9 illustrates the flare investigated by Dominique et al. (2018).

Besides the moderate increase in the relevant wavelength range during a flare, there might be another effect related with flares that could increase the photon-stimulated desorption yield. Energetic flares, at least at the Sun, are often occurring together with CMEs (e.g., Schrijver et al. 2012). Since the photon-stimulated desorption yield increases with an increase in the incident particle flux (Mura et al. 2009; Sarantos et al. 2008, 2010), this could have a recognizable effect on PSD, for surface regions of airless bodies (i.e., Mercury, Moon, asteroids, etc.) that are not protected by a magnetic field.

Whether flares at other stars are also often related with CMEs is yet a matter of debate, and they might at least be restricted for magnetically very active stars (e.g. Moschou et al. 2019). Stellar flares, however, can reach energies of up to more than 10^{30} J (e.g. Wu et al. 2015) and were frequently observed on stars observed by the Kepler (Wu et al. 2015; Davenport et al. 2016) and TESS (e.g. Doyle et al. 2020; Günther et al. 2020; Howard et al. 2020) space missions. Flares with such high energies, also called superflares, are not restricted to

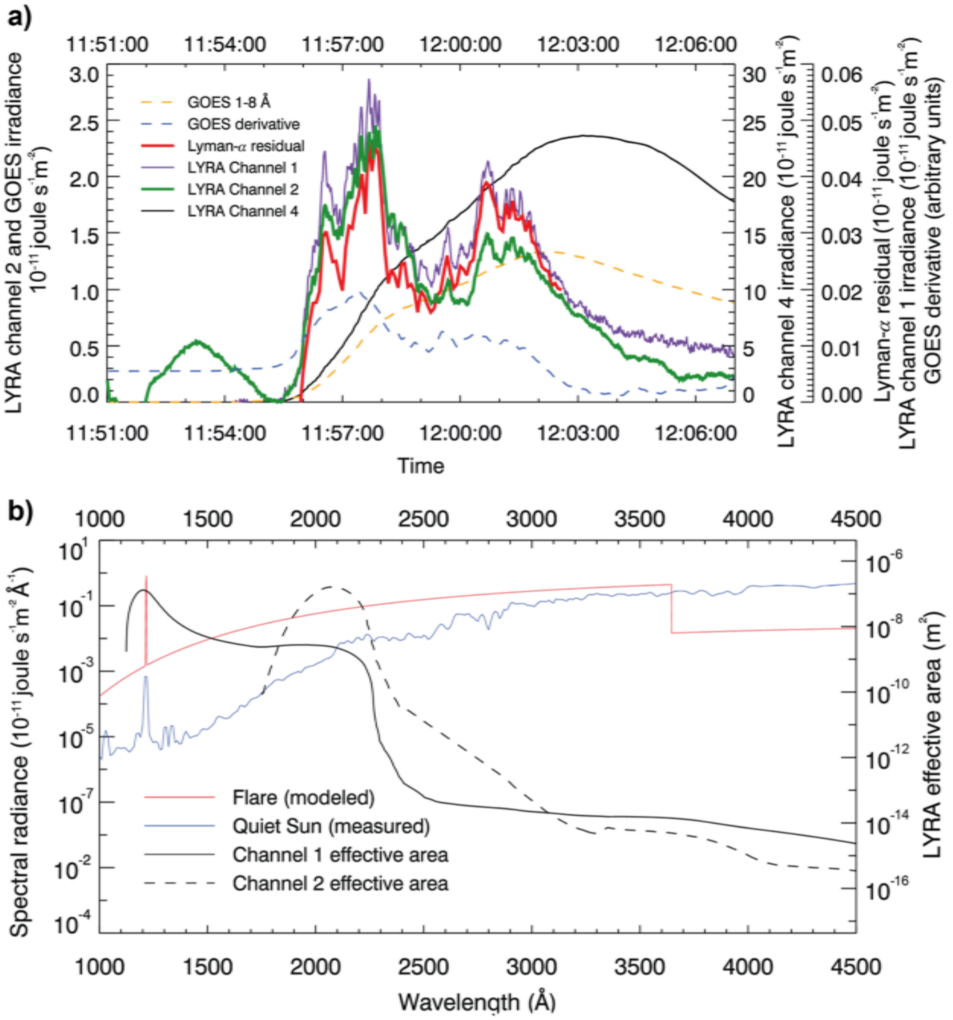

Fig. 9 A typical X-class flare as observed on 6 September 2017. Panel **a**) Solar irradiance during the X9.3 flare with the pre-flare irradiance subtracted, as observed by the GOES satellite (orange), by different channels of the Large-Yield Radiometer (LYRA). LYRA 1 shows 120–123 nm, LYRA 2 shows 190–222 nm, and LYRA 4 shows 0.1–20 nm. Panel **b**) shows the UV wavelength ranges as modeled and observed. Figure is reproduced from Dominique et al. (2018) with permission

magnetically active M-dwarfs (Yang et al. 2017) but can also frequently be found around K- and G-dwarfs (Maehara et al. 2012, 2015; Shibayama et al. 2013, Candelaresi et al. 2014a, 2014b; Namekata et al. 2017; Doyle et al. 2020). However, there seems to be a trend of stars with faster rotation periods ($P_{\mathrm{Rot}} < 10$–12 days) exhibiting stronger superflares (e.g. Notsu et al. 2019; Howard et al. 2020), even though some were also found at stars rotating as slowly as the Sun (Nogami et al. 2014; see also Fig. 8). Shibata et al. (2013) further discuss the occurrence rate of superflares at the Sun, and found that superflares with an energy of $\sim 10^{27}$ J could also occur at the Sun about once in 800 years.

Such superflares might also have a pronounced effect on the planetary space weather of airless bodies. Welsh et al. (2006), for instance, investigated stellar flares in the UV (135 nm–275 nm) with NASA's GALEX satellite and found an average UV flare energy of $2.5 \cdot 10^{13}$ J, thereby increasing the UV irradiation of the respective stars by up to 2.7 magnitudes.

5 Electron Stimulated Desorption

5.1 Theoretical Description

Electron Stimulated Desorption (ESD) and PSD are considered to be very similar processes, where desorption of an atom or molecule from the surface is caused by an electronic excitation of the atom or molecule to be desorbed, leading to an anti-bonding state of the atom or molecule, and eventual release of it from the surface (Yakshinskiy and Madey 2000, 2003, 2004, 2005). The desorption cross-sections for ESD are higher than for PSD, for atomic Na it is $Q_i \approx 1 \cdot 10^{-19}$ cm^2 at 11 eV (Yakshinskiy and Madey 2000, 2005), and atomic K it is $Q_i \approx 2 \cdot 10^{-19}$ cm^2 at 11 eV (Yakshinskiy and Madey 2003). However, the ESD desorption cross-sections first increase and then decrease with increasing coverage of the alkali atoms on the surface, with a maximum ESD yield when 0.3 monolayer of the alkali metal is present on the surface. This yield dependence is explained by the formation metallic clusters on the surface at increasing alkali metal coverage. Also, energy thresholds were observed at 3 eV and 4 eV for Na and K, respectively (Yakshinskiy and Madey 2000, 2005).

Since ESD is a charge transfer process leading to electronic excitations similar to PSD, with comparable cross sections and comparable excitation threshold (Yakshinskiy and Madey 2000), the Velocity Distribution Function (VDF) of released Na are quite similar, so that ESD measurements can be substituted for the desorption processes caused by UV photons. The desorbing Na atoms were found to be ‘hot’ compared to the surface temperature, with suprathermal velocities and non-Maxwellian tails (Yakshinskiy and Madey 2000). The VDF of Electron Stimulated Desorption (ESD) from a lunar basalt sample was found to be similar to that of SiO$_2$, both for offset speed and the peak of the VDF (Yakshinskiy and Madey 2004), and similar to the VDFs measured for PSD. Therefore, we can use the same VDF as used for PSD, Eq. (21).

For the flux of atoms release via ESD for a species i we have to consider

$$\Phi_{ESD,i} = f_i N_S \int \phi_e(E_e)\, Q_i(E_e)\, dE \tag{23}$$

where f_i is the fraction of species, N_S is the surface density of the regolith, $\phi_e(E_e)$ is the incident electron flux as function of electron energy, and $Q_i(E_e)$ is the ESD cross section. This equation cannot be easily simplified since typically there is a wide electron spectrum in the relevant space plasmas, as discussed below, that must be folded with the energy dependent ESD cross section.

5.2 Experimental Observation of ESD

In the laboratory, ESD is widely known for the release of atoms, molecules, and molecular fragments from a variety of adsorbate/substrate systems, see review by Ramsier and Yates (1991). For Mercury and the Moon again the experiments by Madey et al. (1998) and Yakshinskiy and Madey (1999, 2000, 2003, 2004, 2005) have been fundamental to the understanding of the ESD release process. These authors deposited Na or K atoms onto SiO$_2$ surfaces and lunar basalt and measured the ESD cross sections, the temperature dependence, coverage dependence, and the velocity distribution of released Na and K atoms. Among other things, they clearly demonstrated that also ESD is a non-thermal process, the desorption of an alkali atom is the result of an electronic excitation resulting from the absorption of an energetic electron at the surface. In addition to the release of adsorbed species

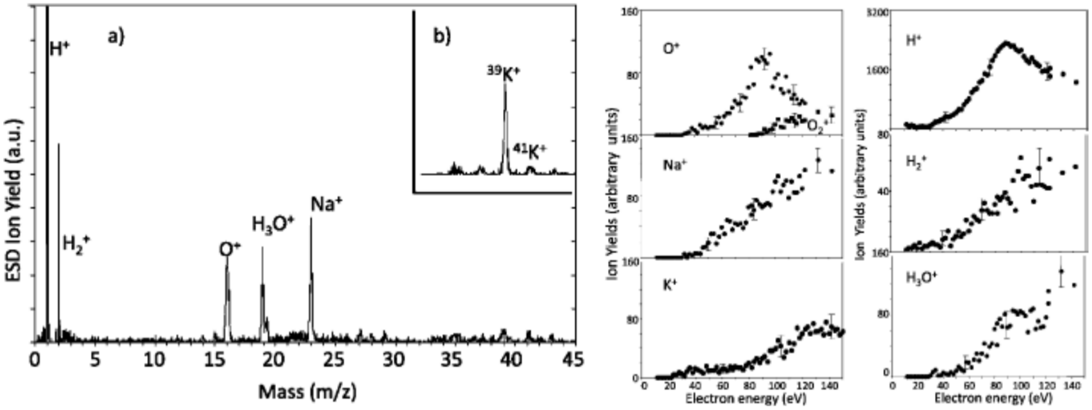

Fig. 10 Left: The 200 eV ESD mass-per-charge (m/z) spectrum of ion yields in arbitrary units (a.u.) obtained during pulsed electron beam irradiation of Na and K bearing glasses. Right: The H^+, H_2^+, H_3O^+, Na^+, K^+, O^+ and O_2^+ yields as a function of incident electron energy. Figure reproduced from McLain et al. (2011) with permission

from the surface by ESD, there are also few reports on the release of neutral atoms from alkali earth surfaces (Wurz et al. 1989, 1991) or ions from silicates (McLain et al. 2011).

ESD has been discussed as a potentially important mechanism for releasing material to the exospheres of the Moon and Mercury. When considered for the Na and K contribution to the lunar exosphere (Madey et al. 2002; Wilson et al. 2006) it was found that contributions ESD cannot be separated from PSD, given the much larger fluxes of solar UV photons compared to solar wind electrons, and the joint presence of relevant populations of electrons and ions in the magnetotail plasma. Similarly, for Mercury's exosphere ESD is considered as one possible source process contributing to the Na exosphere (McClintock et al. 2009), but again in competition with the PSD release process.

The ESD of ionic species from synthetic Na and K silicate glasses have been compared to data from the Fast Imaging Plasma Spectrometer (FIPS) on the MESSENGER spacecraft. From laboratory measurements of ESD ion yields it was concluded that most ions observed by FIPS (Zurbuchen et al. 2008, 2011) can be formed and released by initial single electron scattering events with simple mineral analogs, the from the glassy silicates (McLain et al. 2011). The yields of water group ions are also high, particularly at very low water coverage and the formation and release of O_2^+ (see Fig. 10, middle panel) and Si^+ are very low (McLain et al. 2011); requiring significant surface damage. These ions are less likely to be produced via ESD under the typical flux conditions on Mercury's surface. Thus, any signal at amu/e = 32 in FIPS the data is more likely due to S^+. This is consistent with the proposed stimulated desorption of S^+ from CaS and MgS (Bennett et al. 2016; Schaible et al. 2020).

The ESD ion yields exhibit significant and reversible dependencies as a function of the temperatures present on Mercury. This reversible temperature dependence can be explained by changes in the density and location of defect sites on the surface that become more ESD active, which is also consistent with lattice expansion and increased hole localization at surface defects or defect and vacancy diffusion to the surface. ESD ion yields as function of incident electron energy shown in Fig. 10, right panel, indicate that ion desorption proceeds via ionization of shallow core levels. It is well known that inner shell vacancies (holes) of these shallow core levels decay via Auger electron emission producing two-hole final states that Coulomb explode and eject ions with kinetic energies of several eV. Since the desorption of ions requires a two-hole localized state or an ionized state in the vicinity of an ionized defect or vacancy, increased energy localization and vacancy diffusion will result in increased cross-sections for ion desorption. Under conditions where the impinging electron energy exceeds 15–20 eV, direct ejection of ions or molecules via ESD is highly likely. This may be a higher probability process than neutral desorption followed by photo- or impact ionization and could be a dominant source term for populating exospheres of airless bodies such as the Moon and Mercury with complex ions. Interestingly, the cross sections for ionic desorption from regolith materials also depend on the amount of irradiation damage. A substantial increase in the Na^+ yield is observed with increasing electron dose due the creation of surface defect sites, and these "activated" surface conditions are expected to be present at the surface of the Moon and Mercury.

5.3 Electron Fluxes at Moon and Mercury

5.3.1 Electron Fluxes at the Moon

The Moon is exposed to variable electron fluxes during its orbit as demonstrated in Fig. 11a, which shows the mean electron energy flux at lunar distance as a function of energy and lunar phase compiled from 8 years of ARTEMIS data. The different plasma regions (solar wind, magnetosheath, and magnetotail) are clearly visible in the electron energy spectra. We note that the various magnetotail plasma populations (such as the plasma sheet and the tail lobes) are combined and averaged in Fig. 11a. Additionally, occasional solar transient events temporarily enhance the fluxes of energetic electrons. Most of these transients are smoothed out in the time averaged spectra, but some transients remain identifiable as vertical spikes during the solar wind phase. Figure 11b shows the mean electron energy spectra in units of distribution function for these different plasma environments, providing average electron spectra incident upon the upstream side of the Moon. The incident electron fluxes can be locally modified by multiple processes such as deceleration by the wake potential formed downstream of the plasma flow, deceleration or acceleration by the lunar surface potential, shielding by crustal magnetic fields, and wave-particle interaction. The black arrow and the dashed curve in Fig. 11b show a demonstration of electrostatic deceleration through a -200 V potential, resulting in a 200 eV energy shift to lower energies, conserving the distribution function.

5.3.2 Electron Fluxes at Mercury

The electron environment at Mercury is considerably less well characterized, because only two spacecraft have been able to make in situ measurements to date and electron detection has only been possible at high (>1 keV) electron energies.

During its three flybys of Mercury, Mariner 10's electron spectrometer made observations of several bursts of electrons with unexpectedly high energies. Simpson et al. (1974) reported fluxes of protons with energies of $\sim$550 keV and electrons with energies of $\sim$300 keV, which exceed approximately 10^4 and 10^5 $cm^{-2}\,s^{-1}$, respectively, that have been recorded in the magnetosphere of Mercury during the first Mariner 10 flyby. An alternate explanation of these bursts, suggesting that instrument pile-up was likely responsible, was published soon afterwards (Armstrong et al. 1975). This debate was reviewed in detail (Wurz and Blomberg 2001) but for about 30 years the Mariner 10 data were the only observations available of Mercury's plasma environment.

The MESSENGER mission carried an electron and particle spectrometer (EPS) with a lower detection threshold of 25 keV, which detected bursts of electrons with energies up to 100 keV (Ho et al. 2011a). Electrons of lower energies were detected by repurposing data

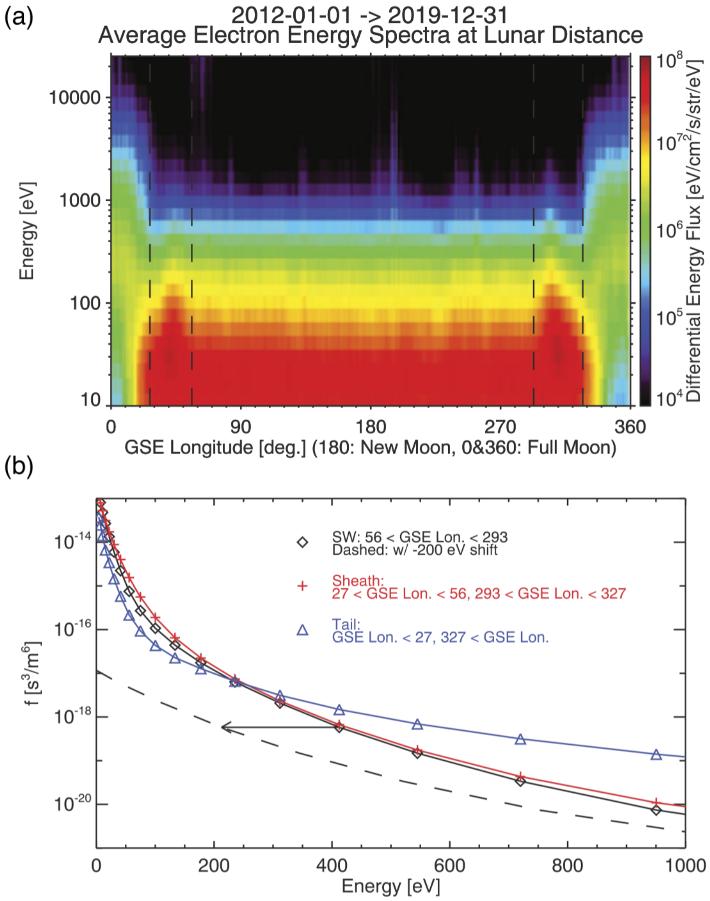

Fig. 11 (**a**) The mean electron energy flux at lunar distance as a function of energy and lunar phase. Spacecraft potential correction was performed in units of distribution function. Possible disturbances of ambient electrons by the Moon and lunar wake are filtered out to first order by using data acquired at $(X_{SSE}^2 + Y_{SSE}^2 + Z_{SSE}^2)^{1/2} > 2R_L$ and $(X_{SSE}^2 + Y_{SSE}^2 + Z_{SSE}^2)^{1/2} > 1.5R_L$. The dashed lines denote the locations of plasma boundaries (bow shock and magnetopause) observed in ion data (Poppe et al. 2018) for reference. (**b**) The mean electron energy spectra for the different plasma environments averaged over the indicated ϕ_{GSE} ranges. A constant background (equivalent to $7 \cdot 10^3$ eV/cm^2/s/str/eV) was subtracted before conversion to distribution function. The dashed curve shows the average solar wind spectrum with -200 eV energy shift, demonstrating electrostatic deceleration by typical wake and nightside surface potentials (*e.g.*, Halekas et al. 2005, 2008a). The ARTEMIS data used to generate this figure are publicly available at http://artemis.ssl.berkeley.edu

from several other instruments, which observed effects driven by electron interactions with matter.

During every one of MESSENGER's three Mercury flybys in January and October 2008 and September 2009, the spacecraft's X-ray Spectrometer (XRS) observed in situ energetic electrons through X-ray fluorescence induced in the instrument's Mg and Al filters, and Cu collimators (Schlemm et al. 2007). These energy spectra are described by a kappa distribution peaking at 0.7–1 keV and with shape factor $\kappa = 7$–8 (Ho et al. 2011b). These electrons were consistently observed throughout MESSENGER's orbital mission, were located in latitudinal groups, and exhibit dawn-dusk asymmetries (Ho et al. 2016).

XRS also observed X-ray fluorescence emitted from the surface of Mercury, stimulated by electrons impacting the surface (Starr et al. 2012). These electrons impact preferentially on the dawnward sector of the nightside of the planet, in aurora-like patterns just equatorward of the open-closed field line boundary at both poles (Lindsay et al. 2016). The energy spectrum of these electrons cannot currently be well characterized, although their energies must exceed 1.9 keV and 4 keV to produce the observed X-ray fluorescence in Si and Ca.

MESSENGER's gamma ray spectrometer (GRS) detected electrons interacting with its anticoincidence shielding (Lawrence et al. 2015), and electrons originating from dipolarization events within the magnetotail (Dewey et al. 2017). These electrons have much higher energies than those detected by XRS either in situ or on the surface, with energies exceeding 100 keV; nevertheless, their spatial distribution matches well with those observed by XRS.

5.3.3 Comparison Between Moon and Mercury

The fundamental differences in electron behaviors and fluxes at the surfaces of Mercury and the Moon stem from the fact that Mercury has an intrinsic global magnetic field, while the Moon does not.

The surfaces of both Mercury and the Moon are accessible to electron impact without an intervening collisional atmosphere, although neither are simply exposed directly to the solar wind at all times in the manner of smaller planetary bodies. At Mercury the locations, energies and fluxes of electron impact are controlled by the structure and processes of the planet's magnetosphere, while at the Moon the dominant driver is the Moon's location within the Sun-Earth-Moon system, and transient variations in solar wind velocity and density. The electron environment at the Moon is also affected by the Earth's magnetosphere; it passes through Earth's current sheet and magnetotail, where the electron energy spectrum increases in energy and hardens. The bulk of the surface is accessible to electron impact, although local crustal magnetic anomalies are very likely to shield small parts of the surface from electron impact.

Acceleration of particles within the Mercury magnetosphere by reconnection and dipolarization events means that electrons impacting at its surface can have significantly higher energies than those typically seen at the Moon, although similar energized electron populations are observed as the Moon passes through Earth's magnetotail.

6 Sputtering by Ion Impact

6.1 The Velocity Distribution of Sputtered Particles

The impact of energetic ions, or neutral atoms, will cause the release of atoms and molecules from the top-most layers of a solid surface, even though the impacting particles will penetrate much deeper. This process is called sputtering, and has been studied in detail in solid state physics for many decades. Recent reviews on sputtering induced by ion bombardment are provided by Sigmund (2012) and Baragiola (2004). For most materials sputtering is the result of the nuclear interaction of the projectile ion with the target material (Betz and Wien 1994), which is the case for the rocks and regolith on Mercury's and the Moon's surface. However, for water also the electronic interaction between the projectile ion with the water ice results in sputtering, with significantly higher sputter yields at higher ion energies (Baragiola et al. 2003).

The sputter yield, Y, is the ratio of the flux of released atoms to the flux of impinging ions. The sputter yield in the nuclear interaction regime has a maximum at an energy around 1 keV/nuc of the impacting ions (Wurz 2012). Towards lower and lower energies, the sputter yield goes to zero because the deposited energy by the impacting ion is not sufficient to overcome the binding energy of atoms at the surface; for energies much higher, the sputter yield also goes to zero because the ions penetrate deeper into the solid without depositing significant energy at and near the surface to cause the release of particles. The energy of 1 keV/nuc corresponds to a velocity of about 440 km/s, which is a typical solar wind velocity. Thus, solar wind plasma, when impinging on a planetary surface, will cause sputtering.

The energy distribution for particles sputtered from a solid, $f(E_e)$, with the energy E_e of the sputtered particle, has been given as Sigmund (1969), Thompson et al. (1968):

$$f(E_e) = 2E_B \frac{E_e}{(E_e + E_B)^3} \quad \text{with} \quad \int_0^\infty f(E_e)\, dE_e = 1 \tag{24}$$

and is known as Sigmund-Thompson energy distribution. Written here in normalized form, where E_B is the binding energy of the sputtered particle, with E_B usually assumed to be the heat of sublimation. Note that the maximum of the energy distribution in Eq. (24) is at $E_{\max} = E_B/2$. At higher energies the distribution falls off with E^{-2}, which was observed experimentally (e.g., Thompson et al. 1968; Husinsky et al. 1985). Since the binary collision between the impinging ion and the surface atom is the limiting case for the energetics of sputtering, this limitation has to be considered in the energy distribution (Wurz and Lammer 2003) and results in a cut-off of the energy distribution at higher energies:

$$f(E_e) = \frac{6E_B}{3 - 8\sqrt{E_B/E_{BC}}} \frac{E_e}{(E_e + E_B)^3} \left(1 - \sqrt{\frac{E_e + E_B}{E_{BC}}}\right) \quad \text{with} \quad \int_0^\infty f(E_e)\, dE_e = 1 \tag{25}$$

where the maximum energy, E_{BC}, that can be transferred in a binary collision is given by

$$E_{BC} = E_{in} \frac{4m_{ion}m_{surf}}{\left(m_{ion} + m_{surf}\right)^2}$$

with m_{ion} the mass of the impacting ion, m_{surf} the mass of the sputtered atom, and E_{in} is the energy of the incident ion. Since in planetary sputtering the sputter agents are mostly H^+ and He^{++} ions, which have low mass compared to the species of a mineral surface, and typical ion energies are keV/nuc, the limit imposed by the maximum transferred energy has to be considered. At low impact energies E_{in} the energy distribution of sputtered atoms will deviate from the E^{-2} dependence, and will peak at lower energies, given by Eq. (25). This deviation of the energy distribution from the E^{-2} for low impact energies has been observed experimentally (e.g., Brizzolara et al. 1988; Goehlich et al. 2000).

The average release velocity, $\langle v \rangle$, is derived from the sputter distribution (Eq. (25)) as

$$\langle v \rangle = \frac{\int v f(v)\, dv}{\int f(v)\, dv} = \frac{1}{2} v_1^2 v_2 \left(\frac{-3v_1^2 + 5v_2^2}{\left(v_1^2 + v_1^2\right)^2} + \frac{3\arctan(v_2/v_1)}{v_1 v_2} \right) \tag{26}$$

with the abbreviations

$$v_1 = \sqrt{\frac{2E_B}{m_{surf}}} \quad \text{and} \quad v_2 = \frac{v_{ion}}{m_{ion} + m_{surf}}$$

The limit of the binary collision imposes a high energy cut-off of the energy distribution of the sputtered particles. Given that the solar wind plasma consists mostly of H and He, this high-energy cut-off is significant and has to be considered in the calculations.

The energy distributions of sputtered atoms from monoatomic samples are very well understood, there is good agreement between the theoretical formulation (Eq. (24)) and the experimental results, see for example reviews by Betz and Wien (1994) and Behrisch and Eckstein (2007). For multicomponent samples fewer experimental data are available. For metal alloys, there are small changes the surface binding energies of elements observed, as inferred from the peak of the energy distribution of sputtered species (Behrisch and Eckstein 2007). Also for alkali-halides and earth alkali-halides the energy distributions of sputtered atoms are described by typical binding energies, however, at elevated temperatures an additional thermal component is observed (Betz et al. 1987; Betz and Husinsky 1988). The most dramatic changes of the energy distribution are observed for oxidized surfaces where a broadening of energy distribution has been observed, which can be fitted with Eq. (24) or Eq. (25) very well, if a large E_B is used (Husinsky 1985). The larger E_B for oxides has been attributed to the larger binding energy of atoms in the oxide (Dullni 1984; Kelly 1986).

Not only atoms are sputtered by ion impact, but also polyatomic compounds and clusters. It is found that for sputtered metallic clusters the energy distributions peak at slightly lower energies than for atoms, and their energy spectrum falls off more steeply towards higher energies (Wahl and Wucher 1994; Behrisch and Eckstein 2007). From the sputter release the polyatomic compounds also have substantial internal temperatures, i.e., rotational and vibrational excitation, of several 1000 K (Behrisch and Eckstein 2007), which will result in the unimolecular decay of these polyatomic compounds and thus limit their life time in a planetary exosphere.

Sputtered ions, usually called secondary ions in the literature, are used in surface science for analytics of surfaces a lot, in Secondary Ion Mass Spectrometers (SIMS) for surface chemical analyses (see Benninghofen et al. 1987; van der Heide 2014). In addition to the physical release, i.e., the actual sputtering of the neutral atoms or ions, the sputtered ions can undergo a charge exchange process when leaving the surface, which is energy dependent, thus it modifies the ion sputter yield and the energy distribution. Faster ions survive more likely the charge exchange process, thus the resulting peak of the energy distribution of sputtered ions moves to higher energies. The variations of the secondary ion yield can span five orders of magnitude or more (see Benninghofen et al. 1987; van der Heide 2014). Since the sputter yield of ions is strongly correlated with the oxidation state of the surface (Wurz et al. 1990) the higher binding energy of oxidized species on the surface will also result in an energy distribution peaking at higher energies. The higher energies of sputtered ions are very well known in surface science community for decades (Benninghofen et al. 1987; Chatzitheodoridis and Kiriakidis 2002; van der Heide 2014). The energy distribution of sputtered ions can be written as

$$f(E_e) \propto \frac{E_e}{\left(E_e + E_{B,i}\right)^{3-2x}} \tag{27}$$

with $E_{B,i}$ the releavant binding energy to characterize the energy distribution of the sputtered ions, and x a numerical value less than 0.15 characterizing the screened Coulombic interaction potential (van der Heide 2014). The observed $E_{B,i}$ are often higher than their neutral counterparts (e.g. Pahlke et al. 1982; Tolstogouzova et al. 2002). The exponent in the denominator of Eq. (27) being less than 3 characterizes the wider tails in the energy distribution of sputtered ions compared to sputtered neutrals (see Eq. (24)). The higher energy of sputtered ions has been observed also in studies relevant to planetology (Dukes and Baragiola 2015).

The angular distribution of the sputtered particles is given in general (Wurz and Lammer 2003) as

$$f(\alpha) = \frac{n\Gamma(n/2)}{\sqrt{\pi}\Gamma\left(\frac{1+n}{2}\right)} \cos\alpha^n \text{ with } \int_{-\pi/2}^{+\pi/2} f(\alpha)\, d\alpha = 1 \tag{28}$$

with α the polar angle, and symmetry in the azimuth angle is assumed. This assumption is well justified because exospheric observations are at a much larger distance from the surface than the typical grain size of regolith particles, thus asymmetries in the azimuth distribution, which do exist (Betz and Wien 1994), are averaged out very well. The exponent n, a real number, is a matter of debate in the planetary science literature. In laboratory measurements of polycrystalline samples often values larger than 1 are found (Betz and Wien 1994), e.g. $n = 2$ by Hofer (1991), or a range of n (Ait El Fqih 2010). However, for modelling of sputtering of planetary surfaces, i.e., the porous regolith with its microscopic roughness, $n = 1$ is often used (Cassidy and Johnson 2005), which gives $f(\alpha) = \cos\alpha$.

6.2 The Total Sputter Yield

The total sputter yield, Y_{tot}, is the ratio of sputtered atoms and the incoming ions. The total sputter yield can be calculated analytically (e.g. Behrisch and Eckstein 2007; Lammer et al. 2003; and references therein). The total sputter yield, Y_{tot}, is given by (Sigmund 1969)

$$Y_{tot} \approx \frac{3\alpha}{\pi\sigma_D E_b} \frac{\left(\frac{2m_{SW}}{m_{SW}+m_{surf}} Z_{SW} Z_{surf} e^2\right)^2}{\gamma E_{in}} 2\varepsilon s_n(\varepsilon) \tag{29}$$

where $s_n(\varepsilon)$ is the nuclear elastic stopping cross-section at the reduced energy, ε of the incident ion, E_b is the surface binding energy, σ_D is the average diffusion cross-section, e is the elementary charge, and α is a collision parameter. The reduced energy, ε, is given by

$$\varepsilon = \frac{\gamma E_{in}}{2e^2} \frac{1}{\frac{2m_{SW}}{m_{SW}+m_{surf}} Z_{SW} Z_{surf}} \frac{0.8853 a_0}{Z_{SW}^{0.23} + Z_{surf}^{0.23}} \tag{30}$$

where E_{in} is the energy of the incident particle, m_{SW} is the mass of the incident ion, m_{surf} the mass of the sample atom, and $\gamma = (4m_{SW}m_{surf})/(m_{SW}+m_{surf})^2$, Z_{SW} and Z_{surf} are the nuclear charges of the incident and sample particles, respectively, and a_0 is the Bohr radius of the hydrogen atom. The nuclear elastic stopping cross-section, $s_n(\varepsilon)$, is given for $\varepsilon < 30$ as

$$s_n(\varepsilon) = \frac{1}{2\varepsilon} \frac{\ln(1 + 1.138\varepsilon)}{1 + 0.0132\varepsilon^{-0.787} + 0.196\varepsilon^{0.5}} \tag{31}$$

and for $\varepsilon > 30$ as

$$s_n(\varepsilon) = \frac{1}{2\varepsilon} \ln(\varepsilon) \tag{32}$$

The analytical expression for the total sputter yield (Eq. (29) through Eq. (32)) contains parameters from the incident ion (E_{in}, m_{SW}, Z_{SW}), which are well known, parameters from the sample atoms (m_{surf}, γ, Z_{surf}), which are also well known, and parameters from the solid that is formed from the sample atoms (E_b, σ_D, α, s_n). The latter parameters are more difficult to obtain, and some are not known at all from experiments. An important parameter of this group is the surface binding energy $E_b$that inversely affects the sputter yield (Eq. (29)) for which often the sublimation energy of the solid is taken. A problem with this theoretical formulation is that it is only given for single element solids. Compounds, which are the normal samples of interest in planetary science, are not covered by this formulation. Another problem are the values of the surface binding energy for the elements contained in compound samples, like minerals, which are not known. This is also a problem for the numerical methods discussed below. To obtain these binding energies for Na Morrissey et al. (2022) performed molecular dynamics calculations of sputtering of Na bearing minerals to derive these binding energies and obtained a range from 2.6 to 8.4 eV for the studied minerals. Considering only minerals that are part of mineral groups relevant to Mercury, jadeite (pyroxene), albite (feldspar) and nepheline (feldspatoid), reduces binding energies to range from 4.8 to 8.4 eV. These minerals are the Na-endmembers of their respective mineral group and therefore very unlikely to appear on the lunar or hermean surface. As the mineral structure of the less Na-bearing pyroxenes, feldspars, and feldspatoids are similar to their Na-endmember, the binding energies could be applicable for less Na-rich minerals, but the binding energies from molecular dynamics likely express an upper limit to their respective mineral group. Moreover, the calculated surface binding energies are for the perfect crystal, but the surfaces of the regolith grains are severely space weathered, such that the top layer of about 100 nm has amorphous fractions, nano-phase iron, and agglutinates (Pieters and Noble 2016). Thus, more work on these surface binding energies is needed.

Modern computer codes give more accurate results for the sputter yield, especially considering compound materials. For example, the TRIM software, today known as SRIM (Ziegler et al. 2010), which uses the Binary Collision Approximation (BCA) to calculate the interaction of the projectile atoms with the atoms of the sample material. TRIM is often used in simulations for planetary science problems because it is simple to use. SRIM includes a graphical user interface that allows for anyone with knowledge of the system they wish to simulate to run a TRIM simulation. It is a relatively old code, based on earlier versions of TRIM (Biersack and Haggmark 1980), and is very well tested against experiment and other simulation methods (Ziegler et al. 2010), however, is not the most accurate BCA code that is available. While the simulation tools TRIM and SDTrimSP have shown good accuracy for yields from monatomic substrates, simulation inputs for sputtering from compounds requires further research.

Because the sputter yield, Y_{tot} is a fundamental parameter for the quantitative interpretation of measurements in the exosphere we briefly review a few of the established tools that can be used to derive these parameters. The TRIM software is publicly available and has been widely used in a planetary context to estimate sputter yields of mineral surfaces since relevant laboratory experiments are scarce (see Sect. 6.8). The few available laboratory results on planetary analog surfaces do indicate, however, that TRIM overestimates sputter yields for light ions impacting composite materials at solar wind energies because of unknown surface binding energies and because TRIM does not account for composition changes in the surface introduced by sputtering (Schaible et al. 2017; Szabo et al. 2018, 2020a). To correct for these limitations, improved versions of TRIM have been developed in the past, the TRIDYN code (Möller and Eckstein 1984), and the SDTrimSP, SDTrim-2D, and SDTrimSP-3D codes (Mutzke et al. 2009, 2011, 2019). The SDTrimSP code predicts the stopping and range of ions in matter as in SRIM but considers the change in composition of the kinetically sputtered sample. The 2D version further considers surface roughness whereas the 3D one introduces also spatial variability of concentrations (Stadlmayr et al. 2018; von Toussaint et al. 2017). The OKSANA (Shulga 2018) code addresses the same limitations of TRIM as SDTrimSP does. Cupak et al. (2021) found that the governing parameter for description of the sputtering behavior is the mean value of the distribution of surface inclination angles, rather than the commonly used root mean square roughness. This finding is the basis for an analytical treatment of the effect of surface roughness on the sputter yield (Szabo et al. 2022).

6.3 Released Particle Flux by Sputtering

Combining the total sputter yield with the angular and energy distribution, we obtain

$$Y\left(E_e,\alpha\right)=Y_{tot}\cdot f\left(E_e\right)\cdot f\left(\alpha\right) \tag{33}$$

With the sputter yield, Y_{tot}, we can proceed to calculate the sputtered flux, Φ_{sp}, resulting from an ion flux, Φ_{ion}, impinging onto the surface:

$$\Phi_{sp}=\Phi_{ion}Y_{tot}$$

For a species i in the surface material we get its sputter flux as

$$\Phi_{sp,i}=\Phi_{ion}Y_{tot,i}=\Phi_{ion}C_iY_{rel,i} \tag{34}$$

with C_i the concentration of species i on the surface and $Y_{rel,i}$ the relative sputter yield. The sputtered flux, $\Phi_{sp,i}$, released from the surface results in a density profile in the exosphere, which can be observed remotely with optical telescopes providing line-of-sight column densities, or in situ by mass spectrometers providing local densities of species. Having measurements of densities in the exosphere one can invert Eq. (34) to obtain the concentration of a species on the surface

$$C_i=\frac{1}{\Phi_{ion}}n_i\left(r\right)\left(\frac{n_i\left(0\right)}{n_i\left(r\right)}\right)\left\langle v_i\right\rangle\frac{1}{Y_{rel,i}} \tag{35}$$

where Φ_{ion} is the flux of ions onto the surface during the observation (obtained either from a measurement or a model), $n_i\left(r\right)$ is the measured density of species i at an altitude r, the ratio $\left(n_i\left(0\right)/n_i\left(r\right)\right)$ relates density to the surface using a model, and $\left\langle v_i\right\rangle$ is the average velocity from the release process (Eq. (26)). Similarly, one can use the measurement of a column density to derive the concentration of a species on the surface

$$C_i=\frac{1}{\Phi_{ion}}NC_i\left(r\right)\left(\frac{n_i\left(0\right)}{NC_i\left(r\right)}\right)\left\langle v_i\right\rangle\frac{1}{Y_{rel,i}} \tag{36}$$

where $NC_i\left(r\right)$ is the measured column density of species i at an altitude r, and the ratio $\left(n_i\left(0\right)/NC_i\left(r\right)\right)$ relates the column density to the surface density using a model.

Since the sputtered flux reflects the bulk composition of the solid quite well, after an equilibrium has been established (Behrisch and Eckstein 2007), the measurement of species in the exosphere resulting from sputtering can be used to infer the chemical composition of the surface.

In practice this deriving the surface concentrations is difficult because of usually there is an unknown mix of release processes that contribute to a given density of an exospheric species. In addition to the mix of processes, there are uncertainties in the flux of ions, the sputter yield of the compound(s) at the surface, a possible latitude and longitude dependence of processes, and the actual global distribution of the exosphere. Therefore, one has to select observations carefully where one or several release processes can be excluded from contributing significantly to the exospheric signal, and assure that the necessary input parameters for the inversion are available, with the selection being different for different species.

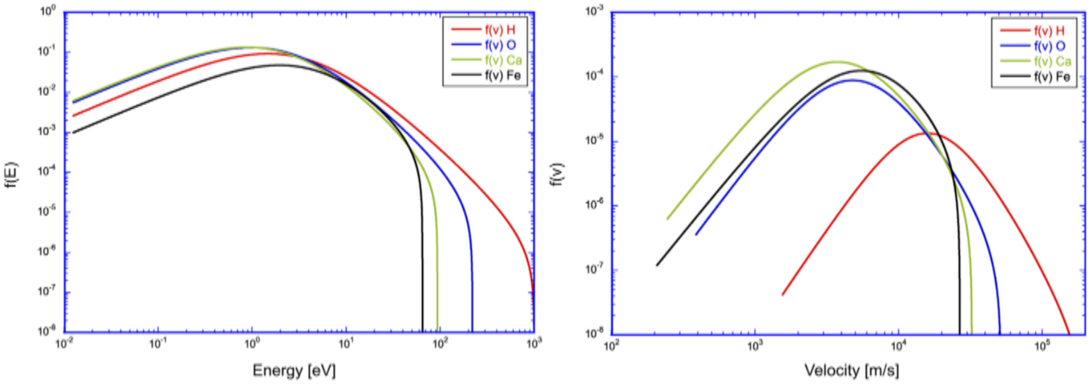

Fig. 12 Left: Sputter energy distribution for H, O, Ca, and Fe from Eq. (25) using a solar wind speed of 440 km s^{-1}. Right: Sputter velocity distribution for H, O, Ca, and Fe

6.4 Exospheric Escape of Sputtered Particles

Figure 12, left panel, shows the energy distribution for sputtered atoms according to Eq. (25) for H, O, Ca, and Fe atoms. Clearly the effect of the high-energy cutoff can be seen, which truncates the energy distribution to lower energies for higher mass atoms. For calculating the escape, it is more convenient to look at the velocity distribution of sputtered atoms, which is shown in Fig. 12, right panel. Because sputtering imparts comparable energies to the different sputtered atoms, they disperse when plotted in velocity space. For the escaping fraction we need to estimate the part of the VDF above the escape speed, which is for Mercury $v_\infty = 4250\ \mathrm{m\,s^{-1}}$ and for the Moon $v_\infty = 2375\ \mathrm{m\,s^{-1}}$.

Figure 12, right panel we immediately see that a considerable fraction of the sputtered atoms is escaping, for Mercury and more so for the Moon. For Mercury, escape fractions range from 31% for Fe to 65% for O, and for the Moon from 90% for Fe to almost 100 % for the light species. To first order there is a mass dependence resulting from the cutoff energy and of course the mass, and to second order there is a species dependence because of the energy distribution is also a function of the binding energy (Eq. (25)). In addition to the direct losses from sputtering, there is also photoionization of the species contributing to the escape.

Note that the energy distributions for the species depend on the binding energy of the atoms on the surface (see Eq. (24) and Eq. (25)), and thus also the calculated escape fractions depend on the binding energy. The binding energies for all species for the range of minerals on the lunar and hermean surface are not known and often binding energies for mono-elemental solids are used or other approximations. Morrissey et al. (2022) performed molecular dynamics calculations of sputtering of Na bearing minerals to derive these binding energies as discussed above. Using these binding energies, they calculated also escape rates for Na, and got similar escape rates as mentioned above. Since they used Eq. (24) rather than Eq. (25) for the energy distributions, their escape rates for Na tend to be somewhat too high.

Comparing the Moon and Mercury, we notice a significant difference: whereas most sputtered atoms escape from the lunar exosphere, a considerable fraction of the sputtered atoms fall back onto Mercury's surface. Since the escape on Mercury is species dependent there will be a change in Mercury's surface composition such that light species are preferentially lost, in particular oxygen, leading to a chemical reduction of the visible surface. Thus, the space weathering is different on the Moon and Mercury.

6.5 Ion Fluxes at Mercury

As described above, plasma regularly impacts Mercury's surface that is primarily by controlled magnetic reconnection and the dynamics of magnetospheric circulation. Early in the MESSENGER mission, Winslow et al. (2014), estimated impact fluxes of protons in the northern and southern magnetospheric cusps as part of proton reflectometry study which estimated the surface magnetic field in those places. Using averages for loss cone and proton properties (density and temperature), they obtained fluxes of $9.8 \cdot 10^3$–$3.9 \cdot 10^8\ \mathrm{cm}^{-2}\,\mathrm{s}^{-1}$ impacting on the surface. Those authors also made a rough estimate of the ion impact flux in the southern cusp, finding about 4 times the northern value, which is a result of the northward shift of the magnetic dipole (Anderson et al. 2012). MESSENGER's highly elliptical orbit with northern hemisphere periapsis, kept it much farther away from the southern cusp than the ∼200–1000 km altitudes of northern cusp crossings. This estimate is consistent with one made from small, plasma-filled magnetic structures termed plasma filaments, that were observed passing through the northern cusp (Poh et al. 2016). They estimated the total rate of impacts on the surface from all cusp filaments to be $(2.70 \pm 0.09) \cdot 10^{25}\ \mathrm{s}^{-1}$. With the entire mission dataset available, Raines et al. (2022) located about 2800 cusp crossings from plasma data enhancements, out of the 4106 orbits containing plasma data. They computed orbit-by-orbit estimates of proton impact flux in the northern cusp ranging from $10^4\ \mathrm{cm}^{-2}\,\mathrm{s}^{-1}$ to $10^8\ \mathrm{cm}^{-2}\,\mathrm{s}^{-1}$, with an average of $\sim 1 \cdot 10^7\ \mathrm{cm}^{-2}\,\mathrm{s}^{-1}$. They found that impact fluxes varied on timescales as low as the 10 s plasma measurements, with peaks up to $\sim 1 \cdot 10^9\ \mathrm{cm}^{-2}\,\mathrm{s}^{-1}$. Applying the same technique to the plasma sheet horn, preliminary estimates of proton impact fluxes in the range of 10^4–$10^7\ \mathrm{cm}^{-2}\,\mathrm{s}^{-1}$ (Raines et al. 2022).

Model estimates of plasma impact fluxes on the surface are at the higher end of the observed range. Kallio and Janhunen (2003) used their hybrid model to simulate proton impact across Mercury's entire surface for a wide range of solar wind conditions. They found ion fluxes impacting on the surface ranging 10^7–$10^9\ \mathrm{cm}^{-2}\,\mathrm{s}^{-1}$ across the dayside, concentrated in the cusp region in most cases, and about an order of magnitude lower fluxes on the nightside, along the open-closed field line boundary. MHD simulations (e.g., Benna et al. 2010) and test particle calculations in analytical fields (Massetti et al. 2003) have reported similar ion fluxes to the surface. Solar wind conditions mainly changed the area over which the highest fluxes were spread, with strongly southward IMF B_Z conditions opening the entire dayside to direct impact by the solar wind. These conditions may have been observed by MESSENGER during intense CMEs (Slavin et al. 2019; Winslow et al. 2020) but only in less than 10 of the over 4100 orbits. A later hybrid modelling study was able to reproduce the relative insensitivity of dayside reconnection at Mercury to the IMF direction (Fatemi et al. 2020), producing fluxes in the same range for both fully southward and northward IMF configurations. A unique aspect of Mercury's interaction with the solar wind arises from the large ratio of the scale of the planet to the scale of its magnetosphere and the presence of a large-size core composed of highly conducting material. This results in strong feedback between the induction field of the planetary interior and the magnetosphere. Especially under conditions of strong external forcing the global magnetospheric structure is affected changing the extent to which the solar wind directly impacts on the surface, which has been studied in recent MHD simulations (Jia et al. 2015; Dong et al. 2019).

Furthermore, Kallio et al. (2008) studied the impact of multiply charged solar wind Fe^{9+} and O^{7+} ions on Mercury's surface by using a quasi-neutral hybrid model. The results of their simulations showed that these heavy multiply charged ions impacted the surface non-homogenously. The highest flux was near the magnetic cusps, similar to the impacting solar wind protons. However, in contrast to protons, the multiply charged ions did not create high ion impact flux regions near the open-closed magnetic field-line boundary (Kallio et al. 2008), instead there is a dawn–dusk asymmetry and the total ion impact rates increased with respect to the increasing mass per charge ratio for ions. The reason is that the gyroradii for the highly charged ions become relevant with respect to the size of the magnetosphere, with the asymmetry resulting from the gradient and curvature drifts that drive positive ions clockwise when viewed from above the North Pole. This asymmetry indicates that Mercury's magnetosphere acts as a kind of "mass spectrometer" for heavy solar wind ions. Impacting multiply charged heavy ions are energy sources that can result in the generation of ion pairs, electrons and soft X-rays as well as EUV-photons in the upper surface layer. The associated energy release from the neutralization of the multiply charged heavy ions occurring at or in the vicinity of the surface can result in an additional release of ions, electrons, neutrals and photons from the planet's surface, which may contribute to its non-isotropic space-weathering.

6.6 Ion Fluxes at Moon

While the Moon is in the solar wind, it is exposed to the solar wind ions that are composed mainly (∼90–95%) of ∼0.5–2 keV protons with minor contributions from multiply charged heavy elements, e.g., He^{2+}, O^{6+}, O^{7+}, Si^{8+}, Fe^{9+}, and others (e.g., Bame et al. 1975; von Steiger et al. 2000; Wurz 2005; Bochsler 2007; Kallio et al. 2008). The solar wind is mainly supersonic and super-Alfvenic and it usually has a non-Maxwellian velocity distribution function (e.g., Marsch et al. 1982; Demars and Schunk 1990; Matteini et al. 2012). The Moon also interacts with the terrestrial bow shock and magnetosheath during its inbound and outbound orbit of the Earth magnetosphere. Plasma composition in those regions is similar to those in the solar wind, but the plasma is highly thermalized (e.g., Halekas et al. 2015). In the magnetotail, the Moon is interacting with earthward and anti-earthward subsonic flow of the solar wind (i.e., H^+ and He^{+2}) and terrestrial ions (mainly O^+, O_2^+, and N_2^+) (e.g., Christon et al. 1994; Seki et al. 1996; Poppe et al. 2016b). The flux of these ions is several orders of magnitude smaller than the solar wind ion flux (e.g., Vaisberg et al. 1996; Poppe et al. 2016b; Artemyev et al. 2017). However, during intense geomagnetic storms and substorms, highly energetic ions have been observed at Moon's distance and beyond (e.g., Zong et al. 1998).

Outside the terrestrial magnetosphere, the Moon may also be exposed to the terrestrial foreshock ions (e.g., Gosling et al. 1978; Greenstadt et al. 1980), foreshock bubbles and cavities (e.g., Sibeck et al. 2002; Turner et al. 2013, 2020; Omidi et al. 2010, 2013; Archer et al. 2015), and hot flow anomalies (HFAs) (e.g., Schwartz et al. 1985; Schwartz 1995; Thomas and Brecht 1988; Eastwood et al. 2008; Zhang et al. 2013; Wang et al. 2013). The foreshock ions, which are the backstreaming particles from the terrestrial bow shock, form three different types of distribution functions: a reflected beam of narrow angular extent, as the kidney-bean shaped distribution, and as a nearly isotropic and diffuse distribution (see review by Eastwood et al. 2005, and references therein). Foreshock bubbles and HFAs have similar characteristics: they have low density plasma with low magnetic field strength in the core, surrounded by high density and thermalized plasma and enhanced field strength. The main difference between them is the HFAs are transient phenomena that move along the bow shock at the intersection between the bow shock and magnetic discontinuity (e.g., Turner et al. 2013).

Nearly 60 years ago, Luna 2 and Explorer X satellites provided the first observation of solar wind ion flux around the Moon in the range of 10^8 to 10^9 $cm^{-2}\,s^{-1}$ (Gringauz et al. 1961; Bridge et al. 1962). Since then, the solar wind plasma parameters around the Moon have been observed by several spacecraft (e.g., Ogilvie et al. 1996; Lin et al. 1998; Halekas et al. 2008b, 2011; Poppe et al. 2014, 2018). Poppe et al. (2018), have statistically provided the most complete picture of the ion fluxes around the Moon. Thanks to the long-period observations of lunar plasma and electromagnetic environment by the ARTEMIS dual-probe mission, Poppe et al. (2018), calculated mean ion energy flux in near-lunar space by averaging over 5 years of ARTEMIS observations. They separated the data set into periods with and without solar energetic particle (SEP) events. They found that SEP events comprised approximately 15% of the data set, while the remaining 85% of the time is without SEPs. Figure 13 shows the average ion energy spectrogram as a function of lunar Geocentric-Solar-Ecliptic (GSE) longitude, i.e., lunar phase. Figure 13a and Fig. 13b show the low and high energy ion spectrum for non-SEP times, respectively, and Fig. 13 c and Fig. 13d show the low and high energy ion spectrum for SEP times, respectively. The vertical dashed lines in Fig. 13a and Fig. 13b indicate the terrestrial bow shock and magnetopause boundary crossings (Poppe et al. 2018). As a result of the tidal locking of the Moon's rotation with its orbit, the highest cumulative solar wind proton implantation on the lunar surface is located on the lunar farside while the most energetic protons impact on the nearside, and the total ion impact rate was found to be smallest when the Moon is deep in the magnetotail (Kallio et al. 2019).

Figure 14 shows the ions' differential flux at different plasma environments the Moon encounters during its orbit around the Earth (Poppe et al. 2018). The averaged differential flux of all different environments (black curve with diamonds) shows the flux peaks at $\sim 10^4$ $\mathrm{cm^{-2}\,s^{-1}\,sr^{-1}\,eV^{-1}}$ near 600 eV. We see the ions cover a broad range of energies, but in general, the most dominant ion fluxes have energies between ~0.1–10 keV.

In addition to the different plasma regimes, lunar crustal magnetic fields (also known as crustal magnetic anomalies) add an extra level of complexity to the ion fluxes that impact the lunar surface. Lunar crustal fields are extensively spread over the entire lunar surface with various field intensities, but they are mostly clustered on the southern hemisphere of the lunar far side (Richmond and Hood 2008; Mitchell et al. 2008; Tsunakawa et al. 2010). The fields are mainly non-dipolar and have complex structures and the maximum strength of the fields on the lunar surface is expected to be at least a few hundred nanotesla (Dyal et al. 1974; Hood et al. 2001; Mitchell et al. 2008). Depending on the strength, geographical location, and the plasma properties that interact with the crustal fields, the access of the plasma to the lunar surface can be substantially altered.

In general, the access of the ions and electrons into the lunar nightside surface is considerably blocked by the plasma absorption on the lunar dayside (e.g., Lyon et al. 1967; Whang 1968; Bale 1997; Harada et al. 2010; Fatemi et al. 2012). However, different mechanisms may facilitate the access of the solar wind ions into the low altitude lunar wake, and eventually the lunar surface. Vorburger et al. (2016) observed that the ion impact on the lunar night side reaches from the terminator to up to 30° beyond the terminator. These mechanisms include (1) The gyrating solar wind protons enter the lunar wake perpendicular to the direction of the IMF as a result of ambipolar processes (Nishino et al. 2009a), (2) Scattered protons from the lunar day side are picked-up by the solar wind and enter deep into the wake (Nishino et al. 2009b; Dhanya et al. 2018), (3) The scattered protons at lower deflection angles on the day side are accelerated close to the polar terminator and enter the lunar night side perpendicular to the magnetic field lines (Wang et al. 2010), (4) The solar wind protons intrude into the wake along the magnetic field lines perhaps due to the ambipolar acceleration (Futaana et al. 2010), (5) The high energy solar wind protons from the tail of the proton velocity distribution function can enter deep into the lunar wake even during parallel IMF conditions (Dhanya et al. 2013). Furthermore, a small fraction of solar wind ions

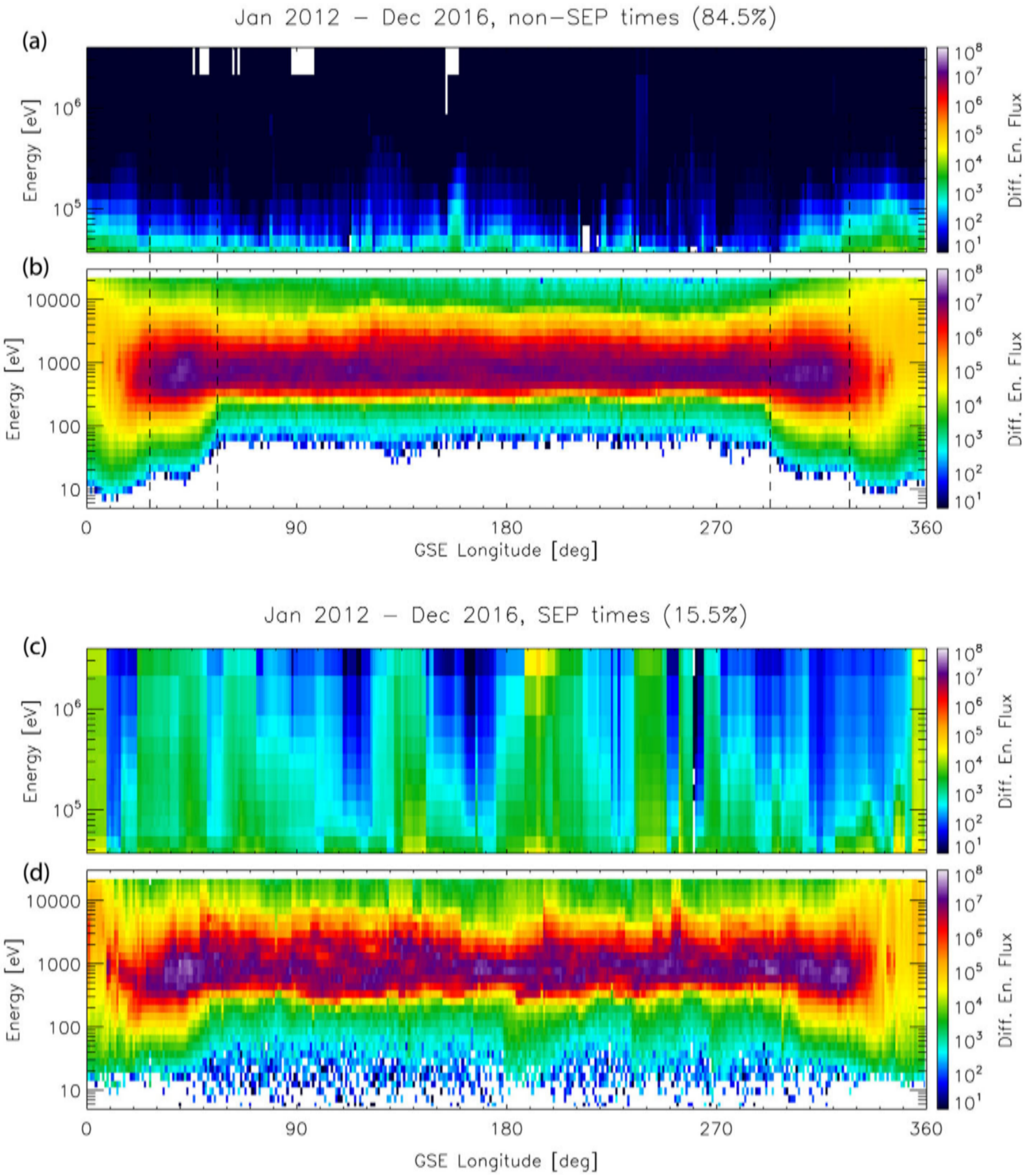

Fig. 13 The mean differential ion energy flux as a function of energy and lunar GSE longitude, where the longitude 0/360° is the "full moon" and 180° is the "new moon". Panels (**a** and **b**) are for non-SEP times and panels (**c** and **d**) SEP times. The dashed lines in panel a and panel b denote observed plasma boundaries (bow shock and magnetopause) as described in the text. Figure reproduced from Poppe et al. (2018) with permission

is reflected at the Earth's bow shock and accelerated to go back to the upstream region along the IMF forming the foreshock (e.g. Eastwood et al. 2005). The typical energy of the reflected ions ranges from several keV to MeV (which is included in the red curve in Fig. 14). When the Moon is located in the foreshock, these high-energy ions backstreaming from the bow shock can directly access the lunar surface (Benson et al. 1975; Nishino et al. 2017). The high-energy ion bombardment on the lunar surface may facilitate sputtering of volatile species there. We still do not exactly know which fraction of these ions impact the nightside lunar surface.

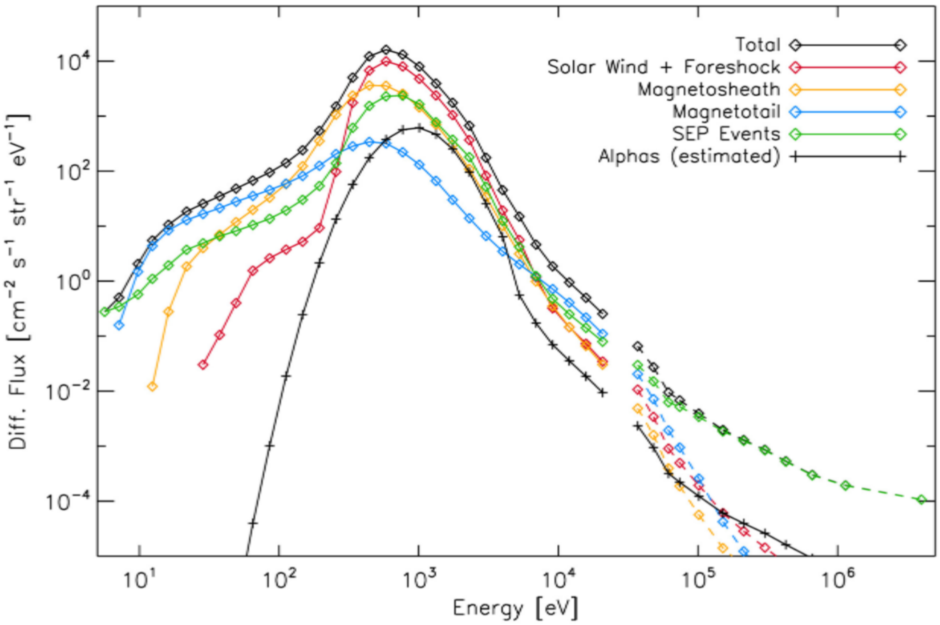

Fig. 14 The mean energy spectrum of ions at the Moon as calculated from the ARTEMIS observations (black diamonds). Colored curves denote the contributions to the mean flux from the solar wind and terrestrial foreshock (red), magnetosheath (orange), magnetotail (blue), and SEP events (green). The fraction of the observed flux due to alpha particles (He^{++}) is estimated as shown by the black crosses. The gap near 30 keV results from the transition of the ESA instrument (1–25,000 eV) to the SST instrument (30 keV–3 MeV). Figure reproduced from Poppe et al. (2018) with permission

6.7 Space Weathering and Sputtering by CME Plasma

Solar wind interacting with exposed surfaces produces energetic exospheric components of sputtered surface minerals (e.g., Lammer and Bauer 1997; Killen and Ip 1999; Wurz and Lammer 2003; Milillo et al. 2005; Killen et al. 2007, 2012; Pfleger et al. 2015), as discussed above. Comparing regular slow solar wind and CME exposure indicates strong enhancements of sputter yields caused by an increased abundance of He and O ions in the CMEs (Kallio et al. 2008). Killen et al. (2012) calculated that CME exposure can enhance the source rates of sputtered elements from the surface such as Ca or Mg from the Moon up to 50 times, depending on the CME plasma parameters, compared to normal solar wind sputtering. Additionally, these researchers found that the released surface minerals have a high probability of escaping the Moon by leaving its Hill sphere either via direct escape or by photoionization.

Due to Mercury's magnetosphere, the usual solar wind plasma is mostly deflected around the planet and does not reach the whole planetary surface on the dayside. During nominal solar wind conditions most of the release of atoms from surface minerals is from the cusp regions where the magnetic field is weakest and particle impact is common (Zurbuchen et al. 2011; Winslow et al. 2012, 2014; Raines et al. 2014; Poh et al. 2016). The release of sputtered atoms from the cusps via sputtering by solar wind ions has been modelled by Mura et al. (2005) in preparation of their direct measurement by the SERENA instrument on BepiColombo (Orsini et al. 2021). As one can see Fig. 15, when a CME collides with Mercury, the magnetosphere gets so compressed that the CME-plasma can reach the surface, releasing surface minerals more efficiently from the planet's surface than during quiet solar wind conditions. Winslow et al. (2017) estimated that during the passage of roughly 30% of CMEs, Mercury's dayside magnetosphere reaches the planet's surface, thereby leaving it

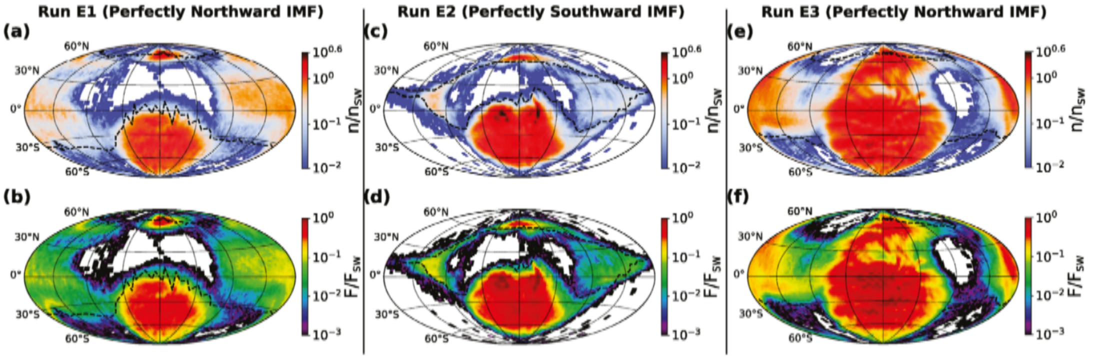

Fig. 15 Contour maps of the solar wind proton impact on the surface of Mercury from hybrid simulations. The density of impacting protons is normalized to the upstream solar wind density (panels **a**–**c**), and the flux of impacting protons normalized to the upstream solar wind flux (panels **d**–**f**). The subsolar point is at the center of each panel at latitude 0° and longitude 12 hr. The open-closed magnetic field line boundaries are calculated from magnetic field from the hybrid simulations and are shown by dashed black lines in each panel. For all panels, the IMF magnitude is $B_{IMF} = 18$ nT, solar wind speed is $600\ \mathrm{km\,s^{-1}}$, and the Mach number is $M_S = 9.2$. For runs E1 and E2 the solar wind density is $70\ \mathrm{cm^{-3}}$, the dynamic pressure is $P_{SW} = 42.2$ nPa, plasma beta $\beta = 2.1$, and Alfvenic Mach number is 12.8. For run E3 the solar wind density is $120\ \mathrm{cm^{-3}}$, the dynamic pressure is $P_{SW} = 72.3$ nPa, plasma beta $\beta = 3.6$, and Alfvenic Mach number is 16.7. Figure reproduced from Fatemi et al. (2020) with permission

temporarily open to bombardment by CME plasma and the interplanetary medium. Slavin et al. (2019) selected four such events in the MESSENGER data and the flux transfer events associated with the passage of a CME. Winslow et al. (2020) provided a thorough analysis of MESSENGER FIPS plasma and the MAG magnetic field data during periods of CME plasma at Mercury, presenting strong evidence for the compression of the magnetopause toward the surface and a simultaneous enhancement in Na^+-group ion densities on the whole dayside. Photoionization of sputtered Na is effective (Wurz et al. 2019), allowing to observe this response in sputtering at the foot-point of the cusp. Orsini et al. (2018) compared ground-based Na images taken at the time of the MESSENGER FIPS and MAG data noticing that the Na exospheric emission during CME passage on 20 September 2013 extended over the whole dayside, while under nominal solar wind conditions the distributions mostly had the usual double peaks at mid latitudes.

Figure 16 shows modelled column densities of Mg and Ca (Pfleger et al. 2015). The column densities increase with increased IMF and plasma parameters. One can see that they become significantly larger for stronger particle exposures. In the latter scenario the entire dayside of Mercury experiences intense ion sputtering which results in column densities that are more than an order of magnitude enhanced in comparison with nominal solar wind conditions. Strong ion density enhancement associated with CMEs have been observed for Na-group ions (Winslow et al. 2020), but not for Mg and Ca ions. Such an efficiency enhancement of the sputter yield can be compared with the findings for the Moon by Killen et al. (2012) mentioned above.

Because the Sun was more active in its past, during the first hundreds of million years of their history Mercury and also the Moon experienced frequent CME, SEP and also flare events that may have led to a depletion of moderately volatile elements during their history (Saxena et al. 2019).

These authors reconstructed the possible CME frequency of the young Sun by using the rotation-flare rate relation for Sun-like stars observed by the Kepler satellite (Notsu et al. 2013) for three classes of assumed rotational histories of the young Sun. One should note that the rotational history of the Sun is unknown, but it would control the amount of magnetic

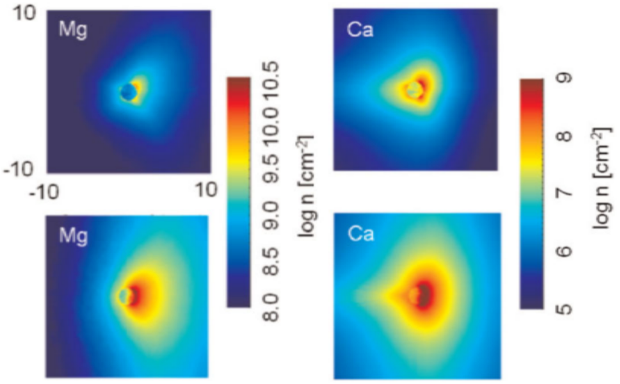

Fig. 16 Modelled column densities for the usual solar wind and CME exposure scenarios described in Fig. 15 obtained by passing the planet along a line parallel to the Sun-planet direction at 10 Mercury radii and projecting the density integrated along the lines of sight onto the noon-midnight plane of Mercury. Each image displays a region of 20 × 20 Hermean radii. Figure adapted from Pfleger et al. (2015) with permission

Fig. 17 Reconstructed CME collision number with Earth per day for three different young Sun rotational evolutions. CME-rates correspond to X10 and X100 flare energies and frequencies inferred from Kepler-based rotation-flare (Notsu et al. 2013) relationships. Figure reproduced from Saxena et al. (2019) with permission

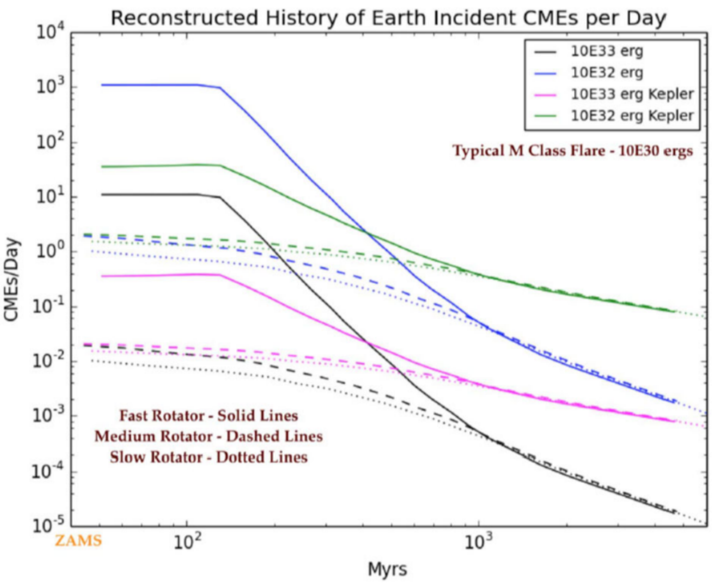

flux emitted and hence the flare and CME activity (Tu et al. 2015; Saxena et al. 2019). Figure 17 shows the reconstructed history of collisions of CMEs with the Earth over time for different evolutionary paths of the Sun (Saxena et al. 2019).

Saxena et al. (2019) concluded that the lunar crust may have stored space weather related evidence from the young Sun due to the expected energetic CMEs and SEPs that interacted with the Moon during the first few hundred million years after its origin. SEPs associated with these CMEs may have induced spallation, the formation of chemical elements from the impact of energetic particles, which could have been recorded in fission tracks, and should be searched for in future samples.

Enhanced spallation effects caused by energetic protons early in the history of the solar system have been discovered in meteoritic grains. High-sensitivity noble gas mass-spectrometric analyses of meteorite grains including solar flare heavy ion tracks show large enrichments of spallation-produced ^{21}Ne and ^{38}Ar when compared to non-irradiated grains from the same meteorite (Caffe et al. 1987; Kööp et al. 2018). These findings can be explained by solar flare irradiation in the early solar system with a proton flux several orders of magnitude higher than contemporary solar flares.

Saxena et al. (2019) suggest that it may be possible to constrain the activity and rotation history of the young Sun by careful analysis of specific samples from different regions of the Moon. We note that similar processes caused by an early period of an even more intense and increased space weather compared to that at the Moon's surface should also have affected Mercury. Orsini et al. (2014) estimated that Sun-induced erosion processes in early times, a combination of ion sputtering, PSD, and enhanced diffusion, caused an erosion of Mercury's top-20 m surface layer, thereby also depleting the moderately volatile element Na.

6.8 Laboratory Experiments for Sputtering of Planetary Surfaces

Laboratory experiments are crucial to verify theoretical predictions for sputtering and to provide models with the required input parameters for yield, angular distribution, energy distribution, and chemical composition of sputtered ejecta (see Sects. 6.1–6.3). First sputter investigations on lunar and lunar analogue material by solar wind ions date back to the early times of lunar exploration (Wehner et al. 1963a, 1963b; Wehner and Kenknight 1967) where lunar solar wind sputter rates between 0.4 and 1.1 Å/year, depending on material, were found. Later, also the ion emission due to solar wind ion impact on lunar analogue material was studied (Elphic et al. 1991), were the range of relative ion yields covered four decades of variation depending on sputtered ion species.

To perform sputtering experiments under laboratory conditions relevant to the surfaces of the Moon and Mercury, a well-defined sputter sample must be created which can then be irradiated. Two main types of samples have been developed by researchers over the past decades: Thin films (micrometers or thinner) that can be deposited on a microbalance and thick samples ($\gg$ micrometers) of loose mineral powder, mineral grains, or pressed pellets. Thin films have the advantage that the sputter yield can be directly measured as the mass loss rate from the microbalance (see Hayderer et al. 1999 for a description of the method) and the chemical and physical properties are easier to characterize. Studies relevant for the Moon and Mercury surface include e.g., Sporn et al. (1997), Küstner et al. (1998, 1999), Tona et al. (2005), Hijazi et al. (2014), Martinez et al. (2017), Hijazi et al. (2017), Stadlmayr et al. (2018), and Szabo et al. (2018). These studies are summarized in Table 4. Thick samples are closer to actual surfaces on the Moon and Mercury, offering the opportunity to directly compare the optical properties of the sample with space observations and to assess the influence of porosity, crystallinity and surface roughness on the sputtering process. Such approaches have been followed by e.g. Loeffler et al. (2009), Meyer et al. (2011), Dukes and Baragiola (2015), Kuhlman et al. (2015), Vyšinka et al. (2016), and Jäggi et al. (2021). The sputter yield from thick samples can only be measured indirectly by catching the ejected particles on a microbalance, in a mass spectrometer or studying them with an atomic force microscope (see e.g. Christoffersen et al. 2012).

The knowledge from sputter experiments relevant for the Moon and Mercury can be summarized in the following very general terms:

- Sputter experiments in laboratory with mineral samples SiO_2, $CaSiO_3$ (wollastonite), and $(Ca,Mg,Fe)_2Si_2O_6$ augite (Schaible et al. 2017; Szabo et al. 2018, 2020a, 2020b) indicate that TRIM overestimates the true sputter yield of solar wind ions sputtering the surfaces of the Moon and Mercury (see Sect. 6.2). The SDTrimSP code reproduces these experimental results better, but some remaining discrepancies indicate that physical processes are still missing in the numerical simulations. This point is illustrated in Fig. 18.

Table 4 Compilation of experimental studies conducted during the last 25 years that are directly relevant to the sputtering of the surface of the Moon and Mercury. This list is non-exhaustive of course

Sample	Sputter agents	Sputter energy	Measurement method(s)	Reference
SiO_2 grains	Ar^+	2 keV	Ion trap m/q and q determination	Vyšinka et al. (2016)
Si films	Mg, Ca, Cr	1 keV	Sputter depth profiling with white light interferometry	Baryshev et al. (2012)
$CaSiO_3$ film	He^{2+}, Ar^{q+}	1 keV/amu	Microbalance	Szabo et al. (2020a)
Fe film	Ar^+	500 eV	Microbalance, AFM to determine surface roughness	Stadlmayr et al. (2018)
$CaSiO_3$ film	Ar^{q+}	1 keV/amu	Microbalance	Szabo et al. (2018)
Glassy film of SiO-undersaturated feldspatoid	Xe^{15+}, Ni^{24+}	225 keV (low-energy example) to 630 MeV (high-energy example)	XY-TOF-SIMS	Martinez et al. (2017)
Anorthite-like glass film	H^+, He^{2+}, Ar^{q+}	0.25 keV/amu and 0.5 keV/amu	Microbalance, measure sputter yield	Hijazi et al. (2014, 2017)
Orthopyroxene	H^+, He^+	1 keV/amu	scanning transmission electron microscope and Electron energy loss spectra to study nanoparticle iron formation	Kuhlman et al. (2015)
Apollo soil samples	He^+	4 keV	Measured sputtered species and their energy distribution incl. Na^+, Mg^+, Al^+, Si^+, Ca^+, Ca^{2+}, Ti^+, Fe^+, and molecular NaO^+, MgO^+, and SiO^+ with mass spectrometer	Dukes and Baragiola (2015)
Na bearing tectosilicate films and Na layers on albite and olivine films	He^+	4 keV	X-ray photoelectron spectroscopy and secondary ion mass spectrometry to measure ionic composition of ejecta	Dukes et al. (2011)
Lunar regolith simulant	H^+, Ar^+, Ar^{6+}, Ar^{9+}	375 eV/amu	Quad. Mass spectrometer, measure sputter yield	Meyer et al. (2011)
Olivine grains	He^+	4 keV	Measure NIR spectra to study nanophase Fe	Loeffler et al. (2009)
SiO_2 and SiH films	I^{q+} ($q = 15–20$)	$E = q \times 3$ keV	TOF SIMS	Tona et al. (2005)
SiO_2 (among other samples)	Highly charged ions ($q > 9$)	Low energies	Various	Schenkel et al. (1999)
Isotropic and pyrolytic graphite	D^+	2 keV	Investigate dependence of Y on angle and surface roughness	Küstner et al. (1998)
SiO_2, LiF	Ar^{q+} ($q \leq 14+$), Xe^{q+}($q \leq 27+$)	$E = (5–20) \times q$ keV	Microbalance	Sporn et al. (1997)

- The sputter yield is $Y \sim 0.01$–0.1 atoms/ion for H^+ at solar wind energy, and $Y \sim 0.1$–1.0 atoms/ion for He^+ at solar wind (Schaible et al. 2017; Roth et al. 1979; Wehner and Kenknight 1967; Hijazi et al. 2017).
- Higher charge states of ions existing in solar wind increase the sputter yield due to potential sputtering. For He^{++} ions, this enhancement is roughly 50% compared to kinetic sputtering by He only (for wollastonite (Szabo et al. 2020a), for KREEP (Barghouty et al. 2011), and anorthite samples (Hijazi et al. 2017)). This is particularly important as He is the most abundant among multiply charged solar wind ion. For heavier multiply charged ions there is also a significant enhancement in the sputter yield because of potential sputtering, but the abundance of the heavy ions in the solar wind is too low to make a difference for the total sputter yield. Claims for significant, or even dominant, contributions to the sputter yield by multiply charged ions heavier than He (Shemansky 2003; Killen et al. 2004) are not compatible with the experimental data from the laboratory.
- In various experiments, the sputter yield has been measured and tabulated as a function of energy, species, inclination angle, and charge state of impactor, but the influence of the sample material properties (i.e., mineral composition, surface roughness, porosity, crystallinity, and temperature) on the sputter yield are not well constrained.
- The sputter yield is a strong function of the angle of incidence, see Fig. 18, however only for smooth surfaces. Since the regolith grains have a large roughness on the microscopic scale, actually all angles of incidence will occur, independent on the macroscopic angle of incidence of the ions. Thus, for the calculation of the sputter yield an angle of 45° should be chosen, which is representative for rough surfaces (Küster et al. 2000; Wurz et al. 2007).
- The energy distribution of neutral sputtered atoms from monoatomic substrates is well established (Betz and Wien 1994). For multi-component substrates less experimental information is available, see discussion in Sect. 6.1, and review by Behrisch and Eckstein (2007). Typical energies for sputtered atoms are a few eV, and typical energies for sputtered ions are about 10 eV (Benninghofen et al. 1987; Dukes and Baragiola 2015).
- The stoichiometry equivalence of ejecta and irradiated surface is attained in equilibrium because the composition of the sputtered flux has to match the bulk composition of the sample, otherwise the sample would be depleted in a species of disproportionally higher sputter yield (Behrisch and Eckstein 2007). This equilibrium means that the very surface, the top 1–3 atomic layers where the sputtered particles come from, have a different composition than the bulk of the sample. Before equilibrium is reached some species can have a disproportional sputter yield, such as sputtering of oxygen that is augmented by potential sputtering (Szabo et al. 2020a). Also adsorbed layers of material, like Na on minerals, might have a larger sputter yield than if these species would be sputtered from the mineral compound (Dukes et al. 2011).
- Changes in surface properties (porosity, roughness, composition, mineral phases) of analogue samples upon sputtering and the implication for remote sensing of planetary surfaces via reflectance spectroscopy can also be investigated in the laboratory (Jäggi et al. 2021).
- The effects of solar wind electrons (with bulk energy of about 5 eV) on mineral samples have not been investigated in laboratory conditions to our knowledge. However, laboratory studies at higher electron energies (tens to hundreds of eV) resembling electrons in Mercury's magnetosphere showed the release of H^+, H_2^+, O^+, H_3O^+, Na^+, K^+ and O_2^+ from silicate glasses, with the H- and O-bearing species from chemisorbed water on the surface (McLain et al. 2011).

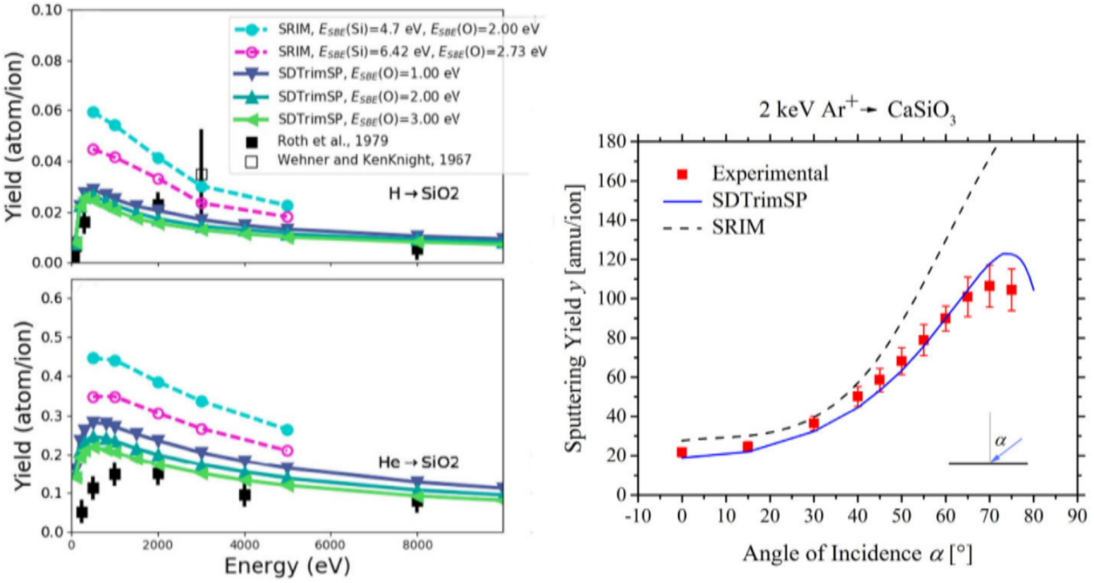

Fig. 18 Measured sputter yields versus numerical predictions. Left panel: Sputter yields of H (top) and He ions (bottom) irradiating a SiO_2 sample. Figure reproduced from Schaible et al. (2017) with permission. Right panel: Ar ions irradiating a $CaSiO_3$ sample as a function of ion incidence angle. Figure reproduced from Szabo et al. (2018) with permission

Although the principles of ion sputtering of minerals are known, there remain several open questions related to sputter processes on the surfaces of the Moon and Mercury, which must be examined in future laboratory experiments. These include determination of sputter yields for mineral species relevant for the Moon and Mercury that have not been investigated, in particular for volatile-rich minerals. Moreover, it should be investigated if and how the sputter characteristics of vapor-deposited mineral films (single minerals, compact, chemically pure) usually preferred in laboratory experiments differ from more 'realistic' samples (i.e., lunar regolith, breccias). On the other hand, more systematic assessments are needed on how accurate laboratory sputter yields can be predicted by numerical simulations in general. This is relevant because we will never have laboratory experiments for every possible configuration needed for surface and exosphere models.

7 Chemical Sputtering

We discussed physical sputtering above, where collisions between a primary particle and the atoms of the solid lead to a collision cascade with the release of atoms from the surface in direct consequence. In contrast, in chemical sputtering the surface is changed by the impact of a primary particle in such a way that an atom or molecule from the surface is released, or its bond to the surface is largely reduced so it can be set free by thermal desorption or by PSD. This can be accomplished by changing the chemical composition (the formation of radiolysis products), by changing the mineralogical composition, by the production of crystal defects and voids, and related processes (Haring et al. 1984; Winters and Coburn 1992). In the context of planetary science, in particular for the surfaces of Mercury and the Moon, Potter (1995) gave this example for chemical sputtering for a simple mineral, sodium silicate:

$$2\mathrm{H} + \mathrm{Na_2SiO_3} \rightarrow 2\mathrm{Na} + \mathrm{SiO_2} + \mathrm{H_2O} \tag{37}$$

where the H atoms in Eq. (36) are solar wind protons being implanted in the near-surface volume, which leads to the formation of silicon oxide, water molecules and atomic Na. Note that the solar wind proton comes with about 1 keV of energy, which is much more than the typical binding energies of atoms in a mineral, facilitating rearrangement of atomic bonds and formation of relocations or dislocations of atoms in the mineral structure. Moreover, the proton is a chemical reactive species contributing to the changes in the mineral. However, the simple sodium silicate presented in Eq. (36) is not a likely mineral to be found on the surface of Mercury or the Moon, but Feldspar is (Wurz et al. 2010), and the chemical equation is then:

$$H + NaAlSi_3O_8 \rightarrow Na + AlO + 3SiO_2 + H_2O \tag{38}$$

again providing the atomic Na on the surface. Similarly, for potassium feldspar (orthoclase, $KAl_3Si_3O_8$) the analog chemical equation can be written with atomic K as one of the end products.

Note that the formulation of the process of chemical sputtering presented as a chemical equation in Eq. (36) and Eq. (37) is a severe simplification of the actual physical and chemical processes induced by the solar wind proton in the near surface volume of the mineral. Nevertheless, processes like this may provide the atomic Na (and K) on the surface needed for the PSD and ESD processes. As a side product, water molecules are produced from the implantation of the solar wind protons in sodium silicate, but the efficiency of this process is likely much lower than 1, with alternative pathways like the production of OH (Tucker et al. 2019).

In summary, chemical sputtering can free alkali atoms (perhaps also other species) from their chemical bounds in the mineral, either on the surface or in the near surface region within the penetration range of the particles. Solar wind protons penetrate about 30 nm depth, energetic protons of a few MeV penetrate to about 0.1 mm (which is a typical regolith grain size), and galactic cosmic rays with GeV energies penetrate to about 1 m. The freed alkali atoms, will diffuse to the surface, given the temperatures on the dayside of Mercury and the Moon. Diffusion of Na and K from the interior to the surface was considered already a while ago to explain the Na and K exosphere observations (Cheng et al. 1987; Tyler et al. 1988). However, the diffusion of Na and K in crystalline matter if not enough by orders of magnitude, and only diffusion enhanced by defects, cracks, voids, … resulting from particle irradiation and micro-meteorite gardening, can explain the observed exospheric densities (Sprague 1990). These alkali metals are the needed supply for the PSD (and ESD) process of releasing Na and K into the exosphere. This concept was successfully used to quantitatively explain the Na observations during Mercury transit in 2004 (Mura et al. 2009).

Alternatively, based on correlations of the ion flux impacting on the surface and the exospheric neutral Na density, Sarantos et al. (2008) concluded for Na observations during the Moon's passage through the magnetotail plasma of the Earth, that the defects created in the surface crystals resulting from the ion bombardment were responsible to enhance other release processes, without invoking the concept of chemical sputtering. As discussed above, these other processes are PSD and thermal desorption. Earlier, Wilson et al. (2006) speculated on a connection between the plasma impact on the lunar surface and the Na in the exosphere observed at some delay.

8 Particle Reflection from Planetary Surfaces

Particle scattering from surfaces has been studied in the laboratory for many years (Niehus et al. 1993). From laboratory experiments it is known that when the ions impact on a surface, a substantial fraction of the ions lose their energies and get absorbed and implanted into the surface. However, depending on the surface composition and roughness as well as the energy of the incident ions, a fraction of them can be backscattered in the form of negative, positive, and/or neutral state particles (McCracken 1975; Niehus et al. 1993; Woodruff 2016). In particular, significant particle reflection is observed for shallow angles of incidence. To first order, the interaction is a binary collision between the projectile ion and the surface atom, moderated by the presence of other atoms on the surface (crystal structure, shadowing, electronic interaction, and other effects). The surfaces used in the laboratory studies were single crystal surfaces, or at least highly polished samples, thus they differ dramatically from the surfaces on the Moon or Mercury made up by regolith, which makes laboratory data often not applicable to the situation on a planetary surface. Thus, we must resort mostly to reports observations from space missions.

Particle reflection from planetary surfaces has been almost exclusively observed for the Moon, because only lunar missions carried the necessary instrumentation for such studies. Particle reflection was observed by the Kaguya, Chandrayaan-1, and IBEX missions, where reflected solar wind ions as well as neutralized solar wind has been reported. In late 2025, the BepiColombo mission will enter Mercury orbit. It also carries instruments for the detection of energetic neutral atoms (Saito et al. 2021; Orsini et al. 2021) so that similar studies will be executed at Mercury. Fortunately, what was learned from the lunar studies on particle reflection applies to other planetary bodies without an atmosphere, for example for Mercury (Lue et al. 2017).

Analysis of observed ENA data from the Chandrayaan-1 mission showed that the directional ENA flux $j_{ENA}(SZA, \theta, \varphi)$ can be described as the product of the solar wind flux j_{SW}, the reflection ratio for perpendicular incidence R_T, and the directional scattering function flux $f_S(SZA, \theta, \varphi)$:

$$j_{ENA}(SZA, \theta, \varphi) = j_{SW} \cdot f_S(SZA, \theta, \varphi) \cdot R_T \tag{39}$$

where φ is the scattering azimuth angle and θ is the scattering polar. R_T is a property of the surface and has to be found experimentally (Vorburger et al. 2013).

Note that while $j_{ENA}(SZA, \theta, \varphi)$ denotes the ENA flux scattered in one angular direction, $j_{ENA}(SZA) = \int j_{ENA}(SZA, \theta, \varphi)\, d\theta d\varphi$ gives the total ENA flux scattered in all directions. The angular distribution of the backscattered solar wind protons as ENAs can be described by the product of four separate ad hoc functions (Schaufelberger et al. 2011; Vorburger et al. 2013):

$$f_S(SZA, \theta) = f_0(SZA) \cdot f_1(SZA, \varphi) \cdot f_2(SZA, \varphi) \cdot f_3(SZA, \theta) \tag{40}$$

where θ is the angle to the surface normal (polar scattering angle) and ranges from 0 to $\pi/2$ angle (i.e., $\theta = 0$ is perpendicular to the surface). φ is the angle between the surface projections of the Sun vector and the vector pointing to the observer (azimuth scattering angle) and ranges from $-\pi$ to $+\pi$. $\varphi = 0$ is the sunward direction, whereas $\varphi = \pm\pi$ is the anti-sunward direction. The solar zenith angle (SZA) is defined as the angle between the surface normal and the vector pointing to the Sun, the latter of which corresponds to the direction from which the solar wind ions impinge onto the surface. While f_0 describes the scattering function's overall amplitude, f_1 through f_3 describe three different features that were seen in the observed data and which are given by:

$$f_1(z_1, \varphi) = z_1 \cdot \cos(2\varphi) + (1 - z_1)$$

$$f_2(z_2,\varphi) = z_2 \cdot \cos(\varphi) + (1 - z_2) \tag{41}$$

$$f_3(z_3,\theta) = \left(1 - \frac{z_3}{\pi/2}\right) \cdot \sin(\theta + z_3) + \frac{z_3}{\pi/2}$$

where the z-terms are functions of the SZA (given in radians), and given by:

$$\begin{aligned} z_1(SZA) &= (0.30 \cdot SZA + 0.03) \\ z_2(SZA) &= 0.24 \cdot \cos(1.30 - 1.52 \cdot SZA) \\ z_3(SZA) &= \frac{\pi}{2} - 1.03 \cdot SZA \end{aligned} \tag{42}$$

Since, the integral of f_S must be equal to the cosine of the solar zenith angle, and f_0 is only a function of the solar zenith angle and not of the observation angles, thus Eq. (38) leads to

$$f_0(SZA) = \frac{\cos(SZA)}{\iint f_1(SZA,\varphi) \cdot f_2(SZA,\varphi) \cdot f_3(SZA,\theta)\, d\Omega} \tag{43}$$

Inserting Eq. (41) and Eq. (42) in Eq. (43) then gives for f_0:

$$\begin{aligned} f_0(SZA) = \cos(SZA)/\{&0.74 \cdot (SZA - 3.23) \cdot \\ &\cdot (2 \cdot SZA \cdot \cos(1.03 \cdot SZA) + SZA \cdot \sin(1.03 \cdot SZA) \cdot \pi - 4 \cdot (SZA - 1.53)) \cdot \\ &\cdot (\cos(1.52 \cdot SZA - 1.30)) - 4.17\} \end{aligned} \tag{44}$$

The energy spectrum of backscattered hydrogen ENAs was also determined empirically from observed ENA data from the Chandrayaan-1 mission (Futaana et al. 2012), which showed that the energy spectra of backscattered ENAs are best reproduced by Maxwell-Boltzmann distribution functions:

$$f(E) = n_0 \sqrt{\frac{2E}{m}} \left(\frac{m}{2\pi k_B T}\right)^{3/2} \exp\left(\frac{-E}{k_B T}\right) \tag{45}$$

where $k_B T$ is the characteristic energy of the scattered particles, and n_0 is the number density. The median of the best parameters of 108 data sets resulted in values of $n_0 = 2.98\ \text{cm}^{-3}$ and $k_B T = 93.0$ eV. If the solar wind velocity is known, then the characteristic energy can be calculated from the solar wind velocity (Futaana et al. 2012):

$$k_B T = 0.273 \cdot v_{SW} - 1.99 \tag{46}$$

with the characteristic energy $k_B T$ in units of [eV] and the solar wind speed v_{SW} in units of [$\text{km}\,\text{s}^{-1}$].

Figure 19 shows an energy sprectum for ENAs recorded by the Chandrayaan-1 mission (Futaana et al. 2012). The best fit of the ENA energy spectra is by a Maxwell-Boltzmann distribution (Eq. (45)), which indicates that the back-scattering mechanism is not a single binary collision with a surface atom, because then the ENA energy would be much higher. Most likely the backscattered ENAs are generated via multiple collisions off surfaces of regolith grains, which have a very rough surface on the microscopic scale. Considering the observed average energy spectrum shown in Fig. 19 implies that the ENAs have lost a considerable fraction of their initial energy as solar wind protons. Assuming an energy loss for each collision with a surface atom of typical 10–20% (Niehus et al. 1993), the impinging protons with an energy of 1 keV ($v_{SW} \approx 400\ \text{km}\,\text{s}^{-1}$) experience 10 to 20 of collisions to end up with a characteristic energy of about 100 eV.

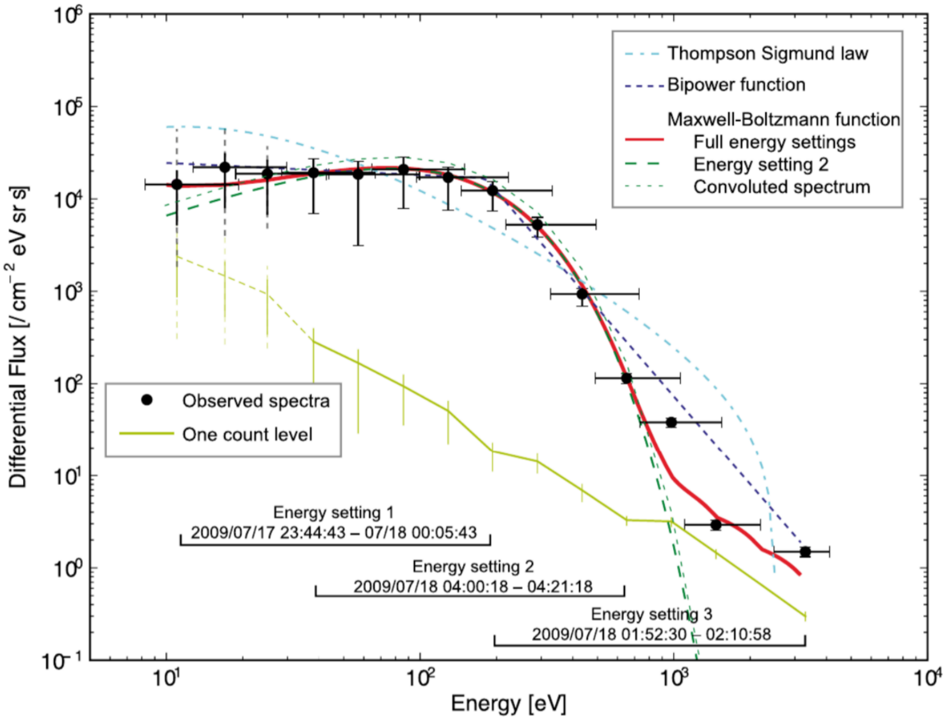

Fig. 19 Differential ENA flux of the observed backscattered ENAs (black circles). Data for three consecutive Chandrayaan-1 orbits around the Moon are averaged. Error bars correspond to the energy resolution (x-axis) and the error in flux (y-axis) mainly due to the uncertainty of the ionization efficiency of the conversion surface of the CENA instrument (Kazama et al. 2009). Particularly, no reliable ionization efficiency is available for low energy channels < 25 eV, and thus, the error bars may be underestimated in the low energy channels < 25 eV (dashed lines). The energy ranges corresponding to the energy settings 1–3 of the CENA instrument are shown. The yellow line gives the one count level based on the accumulation time, the energy resolution, and the ionization efficiency. Three different functions for fitting the data were examined: the Thompson-Sigmund law, Eq. (25) (light blue line), the bi-power law (blue line), and the Maxwell-Boltzmann distribution (red line). In addition, a Maxwell-Boltzmann distribution fitted only to the energy setting 2 data (38–652 eV) is distribution convolved with relatively wide energy also shown by the green dotted line. Figure reproduced from Futaana et al. (2012) with permission

8.1 Observations of Particle Reflection from the Moon

Up until about 2010, it was commonly assumed that almost all ($\sim$99%) plasma ions impinging onto the lunar surface are immediately absorbed there (see e.g., Feldman et al. 2000, Crider and Vondrak 2002). This absorption, and the large obstacle the Moon presents to the plasma flow will cause a plasma vacuum (also known as plasma cavity) behind the Moon (e.g., Lyon et al. 1967). Later, the assumption of total ion absorption was invalidated when the Interstellar Boundary Explorer (IBEX; McComas et al. 2009a) and Chandrayaan-1 (Goswami and Annadurai 2008) observed lunar energetic neutral atoms (ENAs) for the first time (McComas et al. 2009b; Wieser et al. 2009). According to these measurements, a substantial fraction of $\sim$10–20% of the impinging solar wind protons are neutralized and scattered back as ENAs during their interaction with the surface (Vorburger et al. 2013; Lue et al. 2016). Since then, many more ENA reflection studies conducted by IBEX, Chandrayaan-1, and Chang'E-4 have been published. These studies differ in location of the observing instrument with respect to the lunar surface (and thus size of the observed area) and in energy range, but all three missions measured similar ENA reflection ratios.

Table 5 Compilation of reflection ratios for ENAs of lunar hydrogen

Reference	Mission	Moon distance	Surface area/ Observation	Energy range	ENA albedo
McComas et al. (2009b)	IBEX	∼100 000 km	1/4 of Moon	380 eV–2.5 keV	∼0.1
Wieser et al. (2009)	Chandrayaan-1	100–200 km	few hundred km^2	38–652 eV	0.16–0.20
Futaana et al. (2012)	Chandrayaan-1	100–200 km	few hundred km^2	11 eV–3.3 keV	$0.19^{0.21}_{0.16}$
Rodríguez M. et al. (2012)	Chandrayaan-1	100–200 km	1/4 of Moon	10 eV–2 keV	0.09 ± 0.05
Funsten et al. (2013)	IBEX	∼100 000 km	1/4 of Moon	250 eV–3.6 keV	0.07–0.20
Saul et al. (2013)	IBEX	∼100 000 km	1/4 of Moon	10 eV–2 keV	0.11 ± 0.06
Vorburger et al. (2013)	Chandrayaan-1	100–200 km	few hundred km^2	11 eV–2.2 keV	0.16 ± 0.05
Zhang et al. (2020)	Chang'E-4	48 cm	1.6 m^2	30 eV–10 keV	$0.32^{0.58}_{0.19}$

Table 5 lists all published reflection ratios together with their observation parameters. One notable difference between the individual observations is that Chang'E-4, i.e., the measurements were performed from a platform on the lunar surface, measured substantially higher ENA fluxes below 10% solar wind energy than Chandrayaan-1 and IBEX did (Zhang et al. 2020). The authors propose that this is a result of local surface regolith features (e.g., porosity, grain size, composition, and sputter yield) that only become apparent in the high spatial resolution measurements of Chang'E-4 at the surface. As expected, the ENA reflected flux varies with plasma incidence angle, with the highest values measured at the sub-solar point, and with the lowest values measured at the terminator (Wieser et al. 2009).

Since the solar wind plasma not only consists of protons but also contains alpha particles (∼4%), it can be expected that some of these alpha particles are also reflected back to space from the lunar surface as helium ENAs. Indeed, Chandrayaan-1 measured backscattered He for the first time (Vorburger et al. 2014). Unfortunately, the He signal was not strong enough and the instrument's geometric factor was not known well enough to allow any quantification of the He ENA fluxes.

All ENA observations exhibit a similar ENA energy spectrum: The ENA energy spectrum is almost flat at lower energies, rolls over at a characteristic energy of about 100 eV, and above it exponentially decreases with energy up to the initial solar wind energy, ∼0.1–1 keV (Futaana et al. 2012; Rodríguez M. et al. 2012; Allegrini et al. 2013; Funsten et al. 2013). The characteristic ENA energy of 100 eV corresponds to about 10% of the initial solar wind energy. The energy spectrum suggests that the ENAs are mainly produced through backscattering of the solar wind ions and not by the surface sputter processes (e.g., Rodríguez M. et al. 2012). Assuming an average energy loss of 10–20% per surface interaction (Niehus et al. 1993), implies that the particles have undergone 10–20 collisions on the surface before they are scattered back to space. A clear observed linear correlation between the characteristic ENA energy and the solar wind velocity (rather than energy) further hints at the surface interaction process being momentum rather than energy driven.

ENA observations have also indicated that the directional scattering function for hydrogen ENAs depends on the solar wind incident angle to the lunar surface, and it is azimuthally isotropic and mainly sunward at low solar zenith angles (SZAs) but less isotropic and forward-scattering at high SZAs (Schaufelberger et al. 2011). What is contrary to expectations and to laboratory experiments, though, is that ions interacting with the lunar surface are preferably backward-scattered instead of forward-scattered (Schaufelberger et al. 2011). It is assumed that this is a result of the lunar surface regolith not being smooth on an atomic level, but highly porous on a micro-, mini-, and macro-scale instead, resulting in atoms undergoing several collisions before being scattered back to space. This is also supported by the ENAs' energy spectrum, which was discussed above.

The hydrogen ENAs energy spectrum and scattering function are dependent on the plasma temperature (Allegrini et al. 2013; Lue et al. 2016); therefore, their spectrum gets broader in the magnetosheath (Allegrini et al. 2013) and in the terrestrial plasma sheet (Harada et al. 2014a) due to the higher temperature of the ambient plasma compared to that in the solar wind.

ENAs were also observed on the lunar nightside (Vorburger et al. 2016). These nightside ENAs appear as two distinct ring-shaped distributions: the first of which ranges ∼6° into the nightside and can be related to the solar wind kinetic temperature; and the second of which ranges from the terminator ∼30° into the nightside, with its maximum located ∼12° beyond the terminator. The second population is related to ions entering the lunar wake, which are deflected by ambipolar fields at the wake boundary to the lunar night side surface. The nightside ENA populations amount to ∼1.5% of the total dayside ENA flux, and exhibit characteristic energies ∼4 eV lower than the average dayside ENA energy, with an abrupt drop of ∼10 eV in characteristic energy at the terminator.

As the Moon enters Earth's magnetosphere, the plasma environment changes drastically. The solar wind plasma, which was supersonic upstream, is slowed down, shocked to subsonic velocities, and the plasma is compressed and heated in the process. Consequently, the ions backscattered from the lunar surface as ENAs are also modified to some extent. In Earth's magnetosheath, the H ENA energy spectrum is slightly broader and less peaked because of the increased plasma temperature (Lue et al. 2016), whereas in Earth's plasma sheet the hydrogen ENA reflection ratio is slightly lower than the upstream value (Harada et al. 2014a, 2014b).

A fraction of the backscattered particles is electrically charged. Before the first observations of ENAs from the Moon, the Kaguya spacecraft observed that 0.1–1% of the incident solar wind proton flux was backscattered from the lunar surface as protons (H^+) (Saito et al. 2008; Holmström et al. 2010; Lue et al. 2014). From Chandrayaan-1 and IBEX measurements we know that this is a small component compared to the flux of backscattered H-ENA, with a ratio of H^+/H-ENA < 0.1 (see Table 5). The fraction of the backscattered ions from lunar surface is correlated with the solar wind speed, varies from ∼0.01% for low solar wind speed of ∼250 km/s up to ∼1% for high solar wind speed of ∼550 km/s (Lue et al. 2014). The observed backscattered protons cover a broad range of energies from ∼10–100% of the incident solar wind energy, with a peak at ∼70–80% of the solar wind energy, which is higher than the energy peak for hydrogen H-ENAs (Lue et al. 2014). Up until now, the observed ions backscattered from the surface only consist of protons and the backscattering of the heavier solar wind ions (e.g., alpha particles) have not been observed yet (Saito et al. 2008; Lue et al. 2014), perhaps due to the low abundance of the heavier ions in the solar wind results in a backscattering fraction below the observation limits and/or because of the chemistry of their interaction with lunar regolith.

Despite the small fraction of backscattered H^+ ions, this population has important consequences for the lunar plasma environment since these ions flow against the solar wind stream and perturb the solar wind plasma. In turn, the solar wind forces the backscattered

H^+ to cycloid trajectories with curvatures comparable to the Moon itself. Depending on the solar wind and interplanetary magnetic field configurations, these trajectories can bring the ions thousands of kilometers upstream of the Moon (e.g., Holmström et al. 2010; Halekas et al. 2013) or deep into the lunar wake (e.g., Nishino et al. 2009a, 2009b; Dhanya et al. 2016), and may contribute to the H^+ flux onto the nightside surface (see Vorburger et al. 2016).

The backscattered H^+ ions appear to have a similar scattering function to that of the backscattered H-ENAs (Lue et al. 2017, 2018). However, there are clear differences in the energy spectra, where the H^+ ions have a higher mean energy than the H-ENAs (Lue et al. 2014; Lue et al. 2017, 2018). This suggests that the exit speed from the surface affects the charge state fractions of the scattered particles, i.e., the charge state fraction H^+/H-ENA of backscattered particles increases with higher exit speeds from the lunar surface. Since the mean exit speed increases with increasing impact speed (Futaana et al. 2012), Lue et al. (2014) suggested that this exit-speed dependence could explain a positive correlation between the total H^+ scattering rate and the solar wind impact speed, observed in a case study of Chandrayaan-1 data. However, in a larger statistical study of ARTEMIS data, Lue et al. (2018) did not find a similar trend in the total H^+ scattering rate as function of impact speed. Further studies are required to paint a better picture of the relation between the H-ENA and H^+ scattering.

A small fraction of the backscattered solar wind is also expected to be negatively charged, e.g. H^- (Wekhof 1981). H^- photo-detaches into H ENA within a fraction of a second in sunlight at 1 AU, and H^- ions likely do not have a significant impact on the lunar plasma environment. Nevertheless, observations of H^- are required to complete the picture of solar wind scattering from planetary surfaces. Scattered negative ions may be an important component in plasma environments further out in the solar system where the solar photon flux is lower, or in shadowed environments such as the nightside of Mercury. Photo-detachment of negative ions would also contribute to the overall ENA fluxes in a planetary environment.

When incoming ions encounter localized regions of lunar crustal magnetization the interaction between solar wind ions and the lunar surface becomes more complicated (e.g., Kallio et al. 2012; Wieser et al. 2009; Bamford et al. 2012, 2016; Jarvinen et al. 2014; Fatemi et al. 2015; Deca et al. 2015, 2016; Poppe et al. 2016a). As the incoming ions encounter the so-called mini-magnetosphere associated with the crustal magnetization, some ions are decelerated, some are deflected, and some are heated and reflected back to space without interacting with the lunar surface at all. Figure 20 shows a hybrid calculation of the solar wind interaction with a magnetic anomaly on the lunar surface. It demonstrates the deflection of ions at the magnetic anomaly, causing a reduction of ion flux to the surface at the anomaly, and an increase of ion flux surrounding it (an ion "halo"), and a reduction of the ion velocity component towards the surface (Kallio et al. 2012). In the ion "halo" the impact flux and the density of protons are higher than in the undisturbed regions far from the magnetic anomaly (>50 km). The total magnetic field differs from the crustal magnetic field because of the magnetic field associated with the electric currents around the magnetic anomaly. In ENA images this altered interaction process results in the area associated with the crustal magnetization exhibiting less ENA flux while the surrounding area exhibits more ENA flux than the non-magnetized surface nearby (Wieser et al. 2010). Another feature of this modified interaction process is that the mini-magnetosphere exhibits a large electric potential, $+135$ V, because the protons being able to penetrate further into the magnetic field of the mini-magnetosphere than electrons can. This potential was predicted by hybrid modelling (Kallio et al. 2012; Jarvinen et al. 2014) and was observed in Chandrayaan-1 measurements (Futaana et al. 2013).

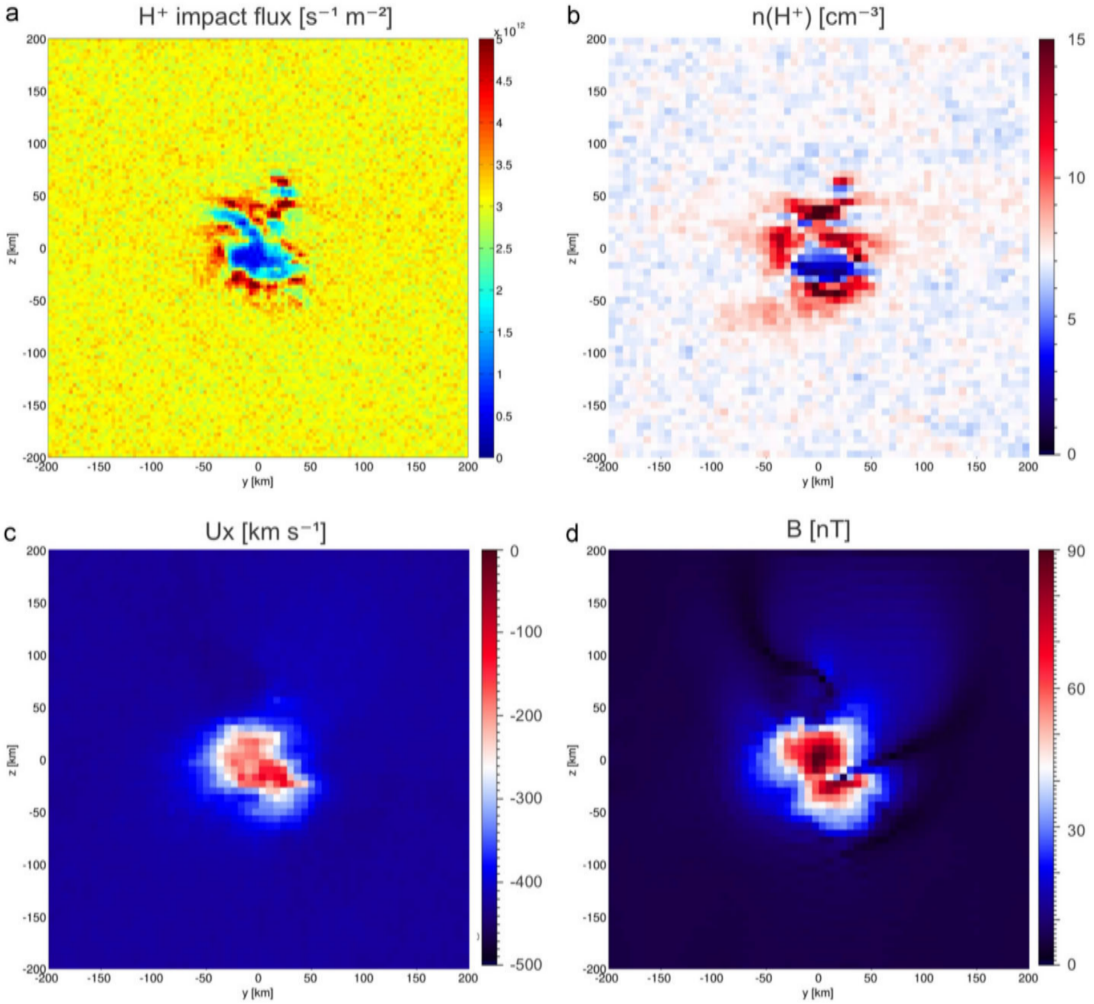

Fig. 20 Properties of the solar wind protons on the lunar surface near a magnetic dipole on the lunar surface. Figure reproduced from Kallio et al. (2012) with permission. (**a**) The impact flux of protons to the surface [$\mathrm{s}^{-1}\,\mathrm{m}^{-2}$], (**b**) the density of protons at the surface [cm^{-3}], (**c**) the vertical velocity of protons [$\mathrm{km\,s}^{-1}$] and (**d**) the total magnetic field [nT]. The magnetic dipole is located 50 km below the surface at $y = z = 0$

From the Chandrayaan-1 observations we know that the shielding efficiency of lunar crustal magnetizations against solar wind ions ranges from 0% to 70%, and strongly depends on the magnetic field strength, the geometric structure of the magnetic anomaly, and on the upstream plasma conditions (Saito et al. 2010; Wieser et al. 2010; Vorburger et al. 2012, 2013; Harada et al. 2014a). Lunar crustal magnetic fields play a crucial role in the incidence and reflection of the solar wind ions on the lunar surface (e.g., Lue et al. 2011; Saito et al. 2012). Observations have shown that on average between 5–10% of the solar wind proton flux is reflected from lunar crustal magnetic fields at an altitude between the surface and the location of the spacecrafts (Lue et al. 2011; Saito et al. 2010, 2012; Poppe et al. 2017; Tsunakawa et al. 2010, 2015). However, depending on the strength and location of the crustal magnetic fields and the energy and angle of the incident solar wind ions, up to 50% reflection over strong crustal fields have been also reported (Lue et al. 2011). Global ENA maps also show a considerable reduction (up to 50%) of backscattered hydrogen ENAs over the magnetized areas on the lunar surface (Vorburger et al. 2013). These ENA observations suggest partial shielding of the lunar surface from the solar wind ions (Saito et al. 2010; Wieser et al. 2010; Vorburger et al. 2013), but the shielding efficiency strongly depends on the strength of the crustal fields and the upstream plasma conditions (Vorburger et al. 2012; Harada et al. 2014a). In addition to the surface shielding, simulations and observations have shown that the solar wind ions are deflected around the magnetized areas and impact the lunar surface (e.g., Kallio et al. 2012; Wieser et al. 2009; Bamford et al. 2012, 2016; Jarvinen et al. 2014; Fatemi et al. 2015; Deca et al. 2015, 2016; Poppe et al. 2016a), resulting in the enhancement of the incident ion flux to the lunar surface in the areas surrounding the magnetic anomaly, and consequently provides a relatively higher backscattering ENA fluxes around some of the strongly magnetized areas compared to the unmagnetized surface (Wieser et al. 2010; Futaana et al. 2013).

The reflected ions from lunar crustal magnetic fields and the backscattered ions from lunar surface interact with the ambient electromagnetic environment and the upstream plasma and generate a broad range of plasma waves from ∼0.01–0.1 Hz narrowband ULF (Nakagawa et al. 2012; Halekas et al. 2013) to ∼0.1–10 Hz broadband whistlers (Halekas et al. 2008a, 2012; Nakagawa et al. 2011; Tsugawa et al. 2012) and narrowband whistlers from ∼1 Hz up to ∼100 Hz (e.g., Lin et al. 1998; Halekas et al. 2006, 2008a; Tsugawa et al. 2011, 2012; Harada et al. 2014b). Some of these reflected ions are "picked-up" and move into the lunar wake and they may impact the lunar nightside (e.g., Nishino et al. 2009b; Dhanya et al. 2018). However, the flux of these ions is expected to be very low, thus they have a minor contribution in the surface sputtering on the nightside.

9 Conclusions

A quantitative treatment of the particle release from the surfaces of the Moon and Mercury is a complicated endeavor. Although the theoretical formulation of the release processes is quite mature, a set of external drivers and parameters related to surface physics are needed for a quantitative calculation of the particle fluxes released from the surface into the exosphere, which often is not available in the needed accuracy. Moreover, in the observations of exospheric species, most often there is a mix of release processes active, which makes the comparison to the theoretical calculations complicated. In that respect Na and K in the exosphere are the most complicated species to interpret, since they can be released by all four release processes.

As external drivers one needs the fluxes of photons, of fluxes plasma particles (ions and electrons) and their energies, and fluxes micrometeorites onto these surfaces. Some of these parameters are available from observations by several spacecraft, with more to expected in the future. Often these parameters are not available at the exact time of the exosphere observation, or the exact location of the exosphere observation, requiring extrapolation and adjustments of these parameters. Thus, often modelling the solar wind plasma, its interaction with the magnetosphere, to define the different plasma populations, is needed to derive the necessary plasma parameters for particle release. Moreover, from the plasma data measured at the spacecraft location one must infer the particle flux that actually arrives at the surface, which is more complicated at Mercury than at the Moon because of its magnetosphere, which is quite variable on short time scales. The resulting global magnetic field is affecting the fluxes of charged particles inside the magnetosphere and thus also the plasma fluxes arriving at the surface and their location.

The surface physics on the microscopic scale, even at the atomic scale, governs the actual release of atoms or molecules from the surface. In principle, processes like sputtering, thermal desorption, and PSD have been studied in the surface science community for decades and longer. However, many of the surface physics parameters, like sputter yields, binding energies, roughness, surface charging, … and the actual mineralogical composition are needed to be known on microscopic spatial scales and thus affect the quantitative prediction of released particle fluxes. Moreover, the systems investigated in these laboratory studies are typically idealized surfaces (e.g. polished sample surfaces) under very controlled laboratory conditions. Thus, their results apply to actual planetary surfaces, which are continuously modified by space weathering, only in a limited way. Bennett et al. (2013) reviewed the processes at planetary surfaces from the surface physics point of view.

Clearly, more laboratory work on the release processes is needed using analogue samples representing the surfaces of the Moon or Mercury, e.g., matching the roughness, the granularity, the mix of minerals. Also, the irradiation by particles or photons should representative of the respective planetary environment. For example, sputtering of regolith-like samples has been investigated by several groups, and promises to be an ongoing activity. If made available, lunar samples from the Apollo missions would be even better for such studies. Release by PSD and ESD is also under investigation by several laboratories. The largest uncertainty is in the exosphere production by micrometeorite impact: on the one hand, the fluxes of micrometeorites onto the surfaces of the Moon and Mercury are not known that well, on the other hand the formation of the impact plasma (its temperature and density), and the release of surface material is the least understood on a quantitative level from the four release processes discussed.

Funding Note Open access funding provided by University of Bern.

References

I. Adler, J.I. Trombka, Orbital chemistry-lunar surface analysis from X-ray and gamma-ray sensing experiments. Phys. Chem. Earth **10**, 17–43 (1977). https://doi.org/10.1016/0079-1946(77)90004-0

M. Ait El Fqih, Angular distribution of sputtered alloy. Experimental and simulated study. Eur. Phys. J. D **56**, 167–172 (2010). https://doi.org/10.1140/epjd/e2009-00272-8

F. Allegrini, M.A. Dayeh, M.I. Desai, H.O. Funsten, S.A. Fuselier, P.H. Janzen, D.J. McComas, E. Möbius, D.B. Reisenfeld, D.F. Rodríguez M., N. Schwadron, P. Wurz, Lunar energetic neutral atom (ENA) spectra measured by the interstellar boundary explorer (IBEX). Planet. Space Sci. **85**, 232–242 (2013). https://doi.org/10.1016/j.pss.2013.06.014

K.A. Anderson, R.P. Lin, R.E. McGuire, J.E. McCoy, Measurement of lunar and planetary magnetic fields by reflection of low energy electrons. Space Sci. Instrum. **1**, 439–470 (1975)

B.J. Anderson, C.L. Johnson, H. Korth, R.M. Winslow, J.E. Borovsky, M.E. Purucker, J.A. Slavin, S.C. Solomon, M.T. Zuber, R.L. McNutt Jr., Low-degree structure in Mercury's planetary magnetic field. J. Geophys. Res. **117**, E00L12 (2012). https://doi.org/10.1029/2012JE004159

M.O. Archer, D.L. Turner, J.P. Eastwood, S.J. Schwartz, T.S. Horbury, Global impacts of a Foreshock Bubble: magnetosheath, magnetopause and ground-based observations. Planet. Space Sci. **106**, 56–66 (2015). https://doi.org/10.1016/j.pss.2014.11.026

T.P. Armstrong, S.M. Krimigis, L.J. Lanzerotti, A reinterpretation of the reported energetic particle fluxes in the vicinity of Mercury. J. Geophys. Res. (1896–1977) **80**, 4015–4017 (1975). https://doi.org/10.1029/JA080i028p04015

A.V. Artemyev, V. Angelopoulos, A. Runov, I.Y. Vasko, Hotion flows in the distant magnetotail: ARTEMIS observations fromlunar orbit to $\sim -200\ R_E$. J. Geophys. Res. Space Phys. **122**, 9898–9909 (2017). https://doi.org/10.1002/2017JA024433

S.D. Bale, Shadowed particle distributions near the Moon. J. Geophys. Res. Space Phys. **102**(A9), 19773–19778 (1997). https://doi.org/10.1029/97JA01676

S.J. Bame, J.R. Asbridge, W.C. Feldman, M.D. Montgomery, P.D. Kearney, Solar wind heavy ion abundances. Sol. Phys. **43**(2), 463–473 (1975). https://doi.org/10.1007/BF00152368

R.A. Bamford, B. Kellett, W.J. Bradford, C. Norberg, A. Thornton, K.J. Gibson, I.A. Crawford, L. Silva, L. Gargaté, R. Bingham, Mini-magnetospheres above the lunar surface and the formation of lunar swirls. Phys. Rev. Lett. **109**(8), 081101 (2012). https://doi.org/10.1103/PhysRevLett.109.081101

R.A. Bamford, E.P. Alves, F. Cruz, B.J. Kellett, R.A. Fonseca, L.O. Silva, R.M.G.M. Trines, J.S. Halekas, G. Kramer, E. Harnett, R.A. Cairns, R. Bingham, 3D PIC simulations of collisionless shocks at lunar magnetic anomalies and their role in forming lunar swirls. Astrophys. J. **830**(2), 146 (2016). https://doi.org/10.3847/0004-637X/830/2/146

D. Banerjee, S. Vadawale, Theoretical modelling of X-ray fluorescence signals for different lunar compositions and dependence on solar activity. Adv. Space Res. **46**, 651–656 (2010). https://doi.org/10.1016/j.asr.2010.04.021

R.A. Baragiola, Sputtering: survey of observations and derived principles. Philos. Trans. - Royal Soc., Math. Phys. Eng. Sci. **362**, 29–53 (2004). https://doi.org/10.1098/rsta.2003.1301

R.A. Baragiola, R.A. Vidal, W. Svendsen, J. Schou, M. Shi, D.A. Bahr, C.L. Atteberrry, Sputtering of water ice. Nucl. Instrum. Methods Phys. Res. B **209**, 294–303 (2003). https://doi.org/10.1016/S0168-583X(02)02052-9

A.F. Barghouty, F.W. Meyer, P.R. Harris, J.H. Adams, Solar-wind protons and heavy ions sputtering of lunar surface materials. Nucl. Instrum. Methods Phys. Res., Sect. B, Beam Interact. Mater. Atoms **269**(11), 1310–1315 (2011). https://doi.org/10.1016/j.nimb.2010.12.033

S.V. Baryshev, A.V. Zinovev, C.E. Tripa, R.A. Erck, I.V. Veryovkin, White light interferometry for quantitative surface characterization in ion sputtering experiments. Appl. Surf. Sci. **258**, 6963 (2012). https://doi.org/10.1016/j.apsusc.2012.03.144

R. Behrisch, W. Eckstein (eds.), *Sputtering by Particle Bombardment, Experiments and Computer Calculations from Threshold to MeV Energies*. Topics in Applied Physics, vol. 110 (Springer, Berlin, 2007). ISBN 978-3-540-44502-9

M.R. Benedikt, M. Scherf, H. Lammer, E. Marcq, P. Odert, M. Leitzinger, N.V. Erkaev, Escape of rock-forming volatile elements and noble gases from planetary embryos. Icarus **347**, 113772 (2000). https://doi.org/10.1016/j.icarus.2020.113772

M. Benna, B.J. Anderson, D.N. Baker, S.A. Boardsen, G. Gloeckler, R.E. Gold, G.C. Ho, R.M. Killen, H. Korth, S.M. Krimigis, M.E. Purucker, R.L. McNutt Jr., J.M. Raines, W.E. McClintock, M. Sarantos, J.A. Slavin, S.C. Solomon, T.H. Zurbuchen, Modeling of the magnetosphere of Mercury at the time of the first MESSENGER flyby. Icarus **209**, 3–10 (2010). https://doi.org/10.1016/j.icarus.2009.11.036

C.J. Bennett, C. Pirim, T.M. Orlando, Space-weathering of solar system bodies: a laboratory perspective. Chem. Rev. **113**(12), 9086–9150 (2013). https://doi.org/10.1021/cr400153k

C.J. Bennett, J.L. McLain, M. Sarantos, R.D. Gann, A. DeSimone, T.M. Orlando, Investigating potential sources of Mercury's exospheric Calcium: photon-stimulated desorption of Calcium Sulfide. J. Geophys. Res., Planets **121**, 137–146 (2016). https://doi.org/10.1002/2015JE004966

A. Benninghofen, F.G. Rüdenauer, H.W. Werner, Secondary ion mass spectrometry–basic concepts, instrumental aspects, applications and trends, Wiley, New York, 1277 pages. Surf. Interface Anal. **10**, 435 (1987). https://doi.org/10.1002/sia.740100811

J. Benson, J.W. Freeman, H.K. Hills, R.R. Vondrak, Bow shock protons in the lunar environment. Earth Moon Planets **14**, 19–25 (1975). https://doi.org/10.1007/BF00562969

A.O. Benz, Flare observations. Living Rev. Sol. Phys. **14**, 2 (2017). https://doi.org/10.1007/s41116-016-0004-3

A.O. Benz, M. Güdel, Physical processes in magnetically driven flares on the Sun, stars, and young stellar objects. Annu. Rev. Astron. Astrophys. **48**(1), 241–287 (2010). https://doi.org/10.1146/annurev-astro-082708-101757

E.L. Berger, L.P. Keller, Solar flare track exposure ages in regolith particles: a calibration for transmission electron microscope measurements. Paper 1543, in *46th Lunar and Planet. Sci. Conf.*, The Woodlands, Texas (2015). https://www.hou.usra.edu/meetings/lpsc2015/pdf/1543.pdf

T.J. Bernatowicz, F.A. Podosek, Argon adsorption and the lunar atmosphere. Proc. Lunar Planet. Sci. **21**, 307–313 (1991).

G. Betz, W. Husinsky, Sputtering of Insulators. Nucl. Instrum. Methods Phys. Res. B **32**, 331–340 (1988)

G. Betz, K. Wien, Energy and angular distributions of sputtered particles. Nucl. Instrum. Methods Phys. Res. B **140**, 1–110 (1994)

G. Betz, E. Wolfrum, P. Wurz, K. Mader, B. Strehl, W. Husinsky, R.F. Haglund, N.H. Tolk, Ground state and excited state atom production by electron and ion bombardment of NaCl and CaF_2, in *Desorption Induced by Electronic Transitions, DIET III*, ed. by R.H. Stuhlen, M.L. Knotek (Springer, Berlin, 1987), pp. 278–283

P. Bhattacharya, R. Bhattacharjee, A study on weibull distribution for estimating the parameters. J. Appl. Quant. Methods **5**(2), 234–241 (2010)

J.P. Biersack, L.G. Haggmark, A Monte Carlo computer program for the transport of energetic ions in amorphous targets. Nucl. Instrum. Methods **174**, 257–269 (1980). https://doi.org/10.1016/0029-554X(80)90440-1

P. Bochsler, Minor ions in the solar wind. Astron. Astrophys. Rev. **14**, 1–40 (2007). https://doi.org/10.1007/s00159-006-0002-x

P. Borin, G. Cremonese, F. Marzari, M. Bruno, S. Marchi, Statistical analysis of micrometeoroids flux on Mercury. Astron. Astrophys. **503**, 259–264 (2009). https://doi.org/10.1051/0004-6361/200912080

P. Borin, M. Bruno, G. Cremonese, F. Marzari, Estimate of the neutral atoms' contribution to the Mercury exosphere caused by a new flux of micrometeoroids. Astron. Astrophys. **517**, A89 (2010). https://doi.org/10.1051/0004-6361/201014312

H.S. Bridge, C. Dilworth, A.J. Lazarus, E.F. Lyon, B. Rossi, F. Scherb, Direct observations of the interplanetary plasma. J. Phys. Soc. Jpn. **17**, 553 (1962). http://adsabs.harvard.edu/abs/1962JPSJS..17B.553B

R.A. Brizzolara, C.B. Cooper, T.K. Olson, Energy distribution of neutral atoms sputtered by very low energy heavy ions. Nucl. Instrum. Methods Phys. Res. B **35**, 36–42 (1988)

M. Bruno, G. Cremonese, S. Marchi, Neutral sodium atoms release from the surfaces of the Moon and Mercury induced by meteoroid impacts. Planet. Space Sci. **55**, 1494–1501 (2007). https://doi.org/10.1016/j.pss.2006.10.006

M.H. Burger, R.M. Killen, W.E. McClintock, R.J. Vervack Jr., A.W. Merkel, A.L. Sprague, M. Sarantos, Modeling MESSENGER observations of calcium in Mercury's exosphere. J. Geophys. Res. **117**, E00L11 (2012). https://doi.org/10.1029/2012JE004158

M.H. Burger, R.M. Killen, W.E. McClintock, A.W. Merkel, R.J. Vervack, T.A. Cassidy, M. Sarantos, Seasonal variations in Mercury's dayside calcium exosphere. Icarus **238**, 51–58 (2014). https://doi.org/10.1016/j.icarus.2014.04.049

M.W. Caffe, C.M. Hohenberg, T.D. Swindle, J.N. Goswami, Evidence in meteorites for an active early Sun. Astrophys. J. **313**, L1 (1987). https://doi.org/10.1086/184826

S. Candelaresi, A. Hillier, H. Maehara, A. Brandenburg, K. Shibata, Superflare occurrence and energies on G-, K-, and M-type dwarfs. Astrophys. J. **792**, 67 (2014a). https://doi.org/10.1088/0004-637X/792/1/67

S. Candelaresi, A. Hillier, H. Maehara, A. Brandenburg, K. Shibata, Superflare occurrence and energies on G-, K-, and M-type dwarfs. Astrophys. J. **792**, 67 (2014b). https://doi.org/10.1088/0004-637X/792/1/67

R.C. Carrington, Description of a singular appearance seen in the Sun on September 1. Mon. Not. R. Astron. Soc. **20**, 13–15 (1859). https://doi.org/10.1093/mnras/20.1.13

W. Cassidy, R.E. Johnson, Monte Carlo model of sputtering and other ejection processes within a regolith. Icarus **176**, 499–507 (2005). https://doi.org/10.1016/j.icarus.2005.02.013

T.A. Cassidy, A.W. Merkel, M.H. Burger, M. Sarantos, R.M. Killen, W.E. McClintock, R.J. Vervack, Mercury's seasonal sodium exosphere: MESSENGER orbital observations. Icarus **248**, 547–559 (2015). https://doi.org/10.1016/j.icarus.2014.10.037

P.C. Chamberlin, T.N. Woods, L. Didkovsky, F.G. Eparvier, A.R. Jones, J.L. Machol, J.P. Mason, M. Snow, E.M.B. Thiemann, R.A. Viereck, D.L. Woodraska, Solar ultraviolet irradiance observations of the solar flares during the intense September 2017 storm period. Space Weather **16**, 1470–1487 (2018). https://doi.org/10.1029/2018SW001866

S.C. Chase Jr., E.D. Miner, D. Morrison, G. Münch, G. Neugebauer, Mariner 10 infrared radiometer results: temperatures and thermal properties of the surface of Mercury. Icarus **28**(4), 565–578 (1976). https://doi.org/10.1016/0019-1035(76)90130-5

E. Chatzitheodoridis, G. Kiriakidis, Secondary ion mass spectrometry and its application to thin film characterization, in *Handbook of Thin Film Materials*, ed. by H.S. Nalwa. Characterization and Spectroscopy of Thin Films, vol. 2 (Academic Press, San Diego, 2002)

Y. Chen, G. Toth, P. Cassak, X. Jia, T.I. Gombosi, J.A. Slavin, M.G. Henderson, Global three-dimensional simulation of Earth's dayside reconnection using a two-way coupled magnetohydrodynamics with embedded particle-in-cell model: initial results. J. Geophys. Res. **122**, 10318–10335 (2017). https://doi.org/10.1002/2017JA024186

A.F. Cheng, R.E. Johnson, S.M. Krimigis, L.J. Lanzerotti, Magnetosphere, exosphere and surface of Mercury. Icarus **71**, 430–440 (1987). https://doi.org/10.1016/0019-1035(87)90038-8

R. Christoffersen, Z. Rahman, L.P. Keller, Solar ion sputter deposition in the lunar regolith: experimental simulation using focused-ion beam techniques. LPSC Conference Paper (2012). https://ntrs.nasa.gov/citations/20120003591

S.P. Christon, G. Gloeckler, D.J. Williams, T. Mukai, R.W. McEntire, C. Jacquey, V. Angelopoulos, A.T.Y. Lui, S. Kokubun, D.H. Fairfield, M. Hirahara, T. Yamamoto, Energetic atomic and molecular ions of ionospheric origin observed in distant magnetotail flow-reversal events. Geophys. Res. Lett. **21**(25), 3023–3026 (1994). https://doi.org/10.1029/94GL02095

M.J. Cintala, Impact-induced thermal effects in the lunar and Mercuria regoliths. J. Geophys. Res. **97**, 947–973 (1992). https://doi.org/10.1029/91JE02207

A. Collette, K. Drake, A. Mocker, Z. Sternovsky, T. Munsat, M. Horanyi, Time-resolved temperature measurements in hypervelocity dust impact. Planet. Space Sci. **89**, 58–62 (2013). https://doi.org/10.1016/j.pss.2013.02.007

B. Cooper, A. Potter, R.K. Illen, T. Morgan, Midinfrared spectra of Mercury. J. Geophys. Res. **106**(E12), 32803–32814 (2001). https://doi.org/10.1029/2000JE001377

D.H. Crider, R.R. Vondrak, Hydrogen migration to the lunar poles by solar wind bombardment of the Moon. Adv. Space Res. **30**, 1869–1874 (2002). https://doi.org/10.1016/S0273-1177(02)00493-3

N.U. Crooker, S. Shodhan, J.T. Gosling, J. Simmerer, R.P. Lepping, J.T. Steinberg, S.W. Kahler, Density extremes in the solar wind. Geophys. Res. Lett. **27**, 3769–3772 (2000). https://doi.org/10.1029/2000GL003788

C. Cupak, P.S. Szabo, H. Biber, R. Stadlmayr, C. Grave, M. Fellinger, J. Brötzner, R.A. Wilhelm, W. Müller, A. Mutzke, M.V. Moro, F. Aumayr, Sputter yields of rough surfaces: importance of the mean surface inclination angle from nano- to microscopic rough regimes. Appl. Surf. Sci. **570**, 151204 (2021). https://doi.org/10.1016/j.apsusc.2021.151204

J.R.A. Davenport, D.M. Kipping, D. Sasselov, J.M. Matthews, C. Cameron, MOST observations of our nearest neighbor: flares on Proxima Centauri. Astrophys. J. Lett. **829**, L31 (2016). https://doi.org/10.3847/2041-8205/829/2/L31

J. Deca, A. Divin, B. Lembège, M. Horányi, S. Markidis, G. Lapenta, General mechanism and dynamics of the solar wind interaction with lunar magnetic anomalies from 3-D particle-in-cell simulations. J. Geophys. Res. Space Phys. **120**(8), 6443–6463 (2015). https://doi.org/10.1002/2015JA021070

J. Deca, A. Divin, X. Wang, B. Lembège, M. Horányi, S. Markidis, G. Lapenta, Three-dimensional full-kinetic simulation of the solar wind interaction with a vertical dipolar lunar magnetic anomaly. Geophys. Res. Lett. **43**(9), 4136–4144 (2016). https://doi.org/10.1002/2016GL068535

H.G. Demars, R.W. Schunk, Solar wind proton velocity distributions: comparison of the bi-Maxwellian based 16-moment expansion with observations. Planet. Space Sci. **38**(9), 1091–1103 (1990). https://doi.org/10.1016/0032-0633(90)90018-L

A.J. DeSimone, T.M. Orlando, Photodissociation of water and O(^{3}P$_J$) formation on a lunar impact melt breccia. J. Geophys. Res., Planets **119**, 894–904 (2014). https://doi.org/10.1002/2013JE004598

A.J. DeSimone, T.M. Orlando, H_2O and O (^{3}P$_J$) photodesorption from amorphous solid water deposited on a lunar mare basalt. Icarus **255**, 44–50 (2015). https://doi.org/10.1016/j.icarus.2014.08.023

R.M. Dewey, J.A. Slavin, J.M. Raines, D.N. Baker, D.J. Lawrence, Energetic electron acceleration and injection during dipolarization events in Mercury's magnetotail. J. Geophys. Res. Space Phys. **122**, 12,170–12,188 (2017). https://doi.org/10.1002/2017JA024617

R.M. Dewey, J.M. Raines, W. Sun, J.A. Slavin, G. Poh, MESSENGER observations of fast plasma flows in Mercury's magnetotail. Geophys. Res. Lett. **45**, 10,110–10,118 (2018). https://doi.org/10.1029/2018GL079056

R.M. Dewey, J.A. Slavin, J.M. Raines, A.R. Azari, W. Sun, MESSENGER observations of flow braking and flux pileup of dipolarizations in Mercury's magnetotail: evidence for current wedge formation. J. Geophys. Res. **125**, e2020JA028112 (2020). https://doi.org/10.1029/2020JA028112

M.B. Dhanya, A. Bhardwaj, Y. Futaana, S. Fatemi, M. Holmström, S. Barabash, M. Wieser, P. Wurz, A. Alok, R.S. Thampi, Proton entry into the near-lunar plasma wake for magnetic field aligned flow. Geophys. Res. Lett. **40**(12), 2913–2917 (2013). https://doi.org/10.1002/grl.50617

M.B. Dhanya, A. Bhardwaj, Y. Futaana, S. Barabash, A. Alok, M. Wieser, M. Holmström, P. Wurz, Characteristics of proton velocity distribution functions in the near-lunar wake from Chandrayaan-1/SWIM observations. Icarus **271**, 120–130 (2016). https://doi.org/10.1016/j.icarus.2016.01.032

M.B. Dhanya, A. Bhardwaj, A. Alok, Y. Futaana, S. Barabash, M. Wieser, M. Holmström, P. Wurz, First observation of transport of solar wind protons scattered from magnetic anomalies into the near lunar wake: observations by SARA/Chandrayaan-1. Geophys. Res. Lett. **45**(17), 8826–8833 (2018). https://doi.org/10.1029/2018GL079330

G.A DiBraccio, J.A. Slavin, S.A. Boardsen, B.J. Anderson, H. Korth, T.H. Zurbuchen, J.M. Raines, D.N. Baker, R.L. McNutt Jr., S.C. Solomon, MESSENGER observations of magnetopause structure and dynamics at Mercury. J. Geophys. Res. **118**997–1008 (2013). https://doi.org/10.1002/jgra.50123

M. Dominique, A.N. Zhukov, P. Heinzel, I.E. Dammasch, L. Wauters, L. Dolla, S. Shestov, M. Kretzschmar, J. Machol, G. Lapenta, W. Schmutz, First detection of solar flare emission in mid-ultraviolet Balmer continuum. Astrophys. J. Lett. **867**, L24 (2018). https://doi.org/10.3847/2041-8213/aaeace

C. Dong, L. Wang, A. Hakim, A. Bhattacharjee, J.A. Slavin, G.A. DiBraccio, K. Germaschewski, Global ten-moment multifluid simulations of the solar wind interaction with Mercury: from the planetary conducting core to the dynamic magnetosphere. Geophys. Res. Lett. **46**, 11588–11596 (2019). https://doi.org/10.1029/2019GL083180

L. Doyle, G. Ramsay, J.G. Doyle, Superflares and variability in solar-type stars with TESS in the Southern hemisphere. Mon. Not. R. Astron. Soc. **494**, 3596–3610 (2020). https://doi.org/10.1093/mnras/staa923

C.A. Dukes, R.A. Baragiola, The lunar surface-exosphere connection: measurement of secondary-ions from Apollo soils. Icarus **255**, 51 (2015). https://doi.org/10.1016/j.icarus.2014.11.032

C.A. Dukes, W.-Y-. Chang, M. Famá, R.A. Baragiola, Laboratory studies on the sputtering contribution to the sodium atmospheres of Mercury and the Moon. Icarus **212**, 463 (2011). https://doi.org/10.1016/j.icarus.2011.01.027

E. Dullni, Velocity distributions of the metal atoms sputtered from oxygen and nitrogen covered Ti- and Al-surfaces. Nucl. Instrum. Methods Phys. Res. B **2**, 610–613 (1984). https://doi.org/10.1016/0168-583X(84)90276-3

J.W. Dungey, Interactions of solar plasma with the geomagnetic field. Planet. Space Sci. **10**, 233–237 (1963). https://doi.org/10.1016/0032-0633(63)90020-5

P. Dyal, C.W. Parkin, W.D. Daily, Magnetism and the interior of the Moon. Rev. Geophys. **12**(4), 568–591 (1974). https://doi.org/10.1029/RG012i004p00568

J.P. Eastwood, E.A. Lucek, C. Mazelle, K. Meziane, Y. Narita, J. Pickett, R.A. Treumann, The foreshock. Space Sci. Rev. **118**(1–4), 41–94 (2005). https://doi.org/10.1007/s11214-005-3824-3

J.P. Eastwood, D.G. Sibeck, V. Angelopoulos, T.D. Phan, S.D. Bale, J.P. McFadden, C.M. Cully, S.B. Mende, D. Larson, S. Frey, C.W. Carlson, K.-H. Glassmeier, H.U. Auster, A. Roux, O. Le, Contel, THEMIS observations of a hot flow anomaly: solar wind, magnetosheath, and ground-based measurements. Geophys. Res. Lett. **35**, L17S03 (2008). https://doi.org/10.1029/2008GL033475

J. Egedal, W. Daughton, A. Le, Large-scale electron acceleration by parallel electric fields during magnetic reconnection. Nat. Phys. **8**, 321–324 (2012). https://doi.org/10.1038/nphys2249

G. Eichhorn, Impact light flash studies: temperature, ejecta, vaporization, in *Interplanetary Dust and Zodiacal Light*, vol. 48 (1976), pp. 243–247. https://doi.org/10.1007/3-540-07615-8_490

G. Eichhorn, Heating and vaporization during hypervelocity particle impact. Planet. Space Sci. **26**, 463–467 (1978a). https://doi.org/10.1016/0032-0633(78)90067-3

G. Eichhorn, Primary velocity dependence of impact ejecta parameters. Planet. Space Sci. **26**, 469–471 (1978b). https://doi.org/10.1016/0032-0633(78)90068-5

R.C. Elphic, H.O. Funsten III, B.L. Barraclough, D.J. McComas, M.T. Paffett, D.T. Vaniman, G. Heiken, Lunar surface composition and solar wind-induced secondary ion mass spectrometry. Geophys. Res. Lett. **18**(11), 2165–2168 (1991). https://doi.org/10.1029/91GL02669

A.G. Emslie, B.R. Dennis, G.D. Holman, H.S. Hudson, Refinements to flare energy estimates: a follow-up to “Energy partition in two solar flare/CME events” by A.G. Emslie et al. J. Geophys. Res. **110**, A11103 (2005). https://doi.org/10.1029/2005JA011305

A.G. Emslie, B.R. Dennis, A.Y. Shih, P.C. Chamberlin, R.A. Mewaldt, C.S. Moore, G.H. Share, A. Vourlidas, B.T. Welsch, Global energetics of thirty-eight large solar eruptive events. Astron. J. **759**, 71 (2012). https://doi.org/10.1088/0004-637X/759/1/71

N.V. Erkaev, H. Lammer, P. Odert, Yu.N. Kulikov, K.G. Kislyakova, Extreme hydrodynamic atmospheric loss near the critical thermal escape regime. Mon. Not. R. Astron. Soc. **448**, 1916–1921 (2015). https://doi.org/10.1093/mnras/stv130

W. Exner, D. Heyner, L. Liuzzo, U. Motschmann, D. Shiota, K. Kusano, T. Shibayama, Coronal mass ejection hits Mercury: A.I.K.E.F. hybrid-code results compared to MESSENGER data. Planet. Space Sci. **153**, 89–99 (2018). https://doi.org/10.1016/j.pss.2017.12.016

W.M. Farrell, T.J. Stubbs, R.R. Vondrak, G.T. Delory, J.S. Halekas, Complex electric fields near the lunar terminator: the near-surface wake and accelerated dust. Geophys. Res. Lett. **34**, L14201 (2007). https://doi.org/10.1029/2007GL029312

W.M. Farrell, J.S. Halekas, R.M. Killen, G.T. Delory, N. Gross, L.V. Bleacher, D. Krauss-Varben, P. Travnicek, D. Hurley, T.J. Stubbs, M.I. Zimmerman, T.L. Jackson, Solar-Storm/Lunar Atmosphere Model (SSLAM): an overview of the effort and description of the driving storm environment. J. Geophys. Res. **117**, E00K04 (2012). https://doi.org/10.1029/2012JE004070

S. Fatemi, M. Holmström, Y. Futaana, The effects of lunar surface plasma absorption and solar wind temperature anisotropies on the solar wind proton velocity space distributions in the low-altitude lunar plasma wake. J. Geophys. Res. Space Phys. **117**, A10 (2012). https://doi.org/10.1029/2011JA017353

S. Fatemi, C. Lue, M. Holmström, A.R. Poppe, M. Wieser, S. Barabash, G.T. Delory, Solar wind plasma interaction with Gerasimovich lunar magnetic anomaly. J. Geophys. Res. Space Phys. **120**(6), 4719–4735 (2015). https://doi.org/10.1002/2015JA021027

S. Fatemi, N. Poirier, M. Holmström, J. Lindkvist, M. Wieser, S. Barabash, A modelling approach to infer the solar wind dynamic pressure from magnetic field observations inside Mercury's magnetosphere. Astron. Astrophys. **A614**, A132 (2018). https://doi.org/10.1051/0004-6361/201832764

S. Fatemi, A.R. Poppe, S. Barabash, Hybrid simulations of solar wind proton precipitation to the surface of Mercury. J. Geophys. Res. **125**, e2019JA027706 (2020). https://doi.org/10.1029/2019JA027706

W.C. Feldman, D.J. Lawrence, R.C. Elphic, B.L. Barraclough, S. Maurice, I. Genetay, A.B. Binder, Polar hydrogen deposits on the Moon. J. Geophys. Res. **105**, 4175–4176 (2000). https://doi.org/10.1029/1999JE001129

L. Fletcher, B.R. Dennis, H.S. Hudson, S. Krucker, K. Phillips, A. Veronig, M. Battaglia, L. Bone, A. Caspi, Q. Chen, P. Gallagher, P.T. Grigis, H. Ji, W. Liu, R.O. Milligan, M. Temmer, An observational overview of solar flares. Space Sci. Rev. **159**, 19 (2011). https://doi.org/10.1007/s11214-010-9701-8

N. Fray, B. Schmitt, Sublimation of ices of astrophysical interest: a bibliographic review. Planet. Space Sci. **57**, 2053–2080 (2009). https://doi.org/10.1016/j.pss.2009.09.011

C. Fröhlich, Total solar irradiance: what have we learned from the last three cycles and the recent minimum? Space Sci. Rev. **176**, 237–252 (2013). https://doi.org/10.1007/s11214-011-9780-1

H.O. Funsten, F. Allegrini, P.A. Bochsler, S.A. Fuselier, M. Gruntman, K. Henderson, P.H. Janzen, R.E. Johnson, B.A. Larsen, D.J. Lawrence, D.J. McComas, E. Möbius, D.B. Reisenfeld, D. Rodríguez, N.A. Schwadron, P. Wurz, Reflection of solar wind hydrogen from the lunar surface. J. Geophys. Res. **118**(2), 292–305 (2013). https://doi.org/10.1002/jgre.20055

Y. Futaana, S. Barabash, M. Wieser, M. Holmström, A. Bhardwaj, M.B. Dhanya, R. Sridharan, P. Wurz, A. Schaufelberger, K. Asamura, Protons in the near-lunar wake observed by the sub-keV atom reflection analyzer on board Chandrayaan-1. J. Geophys. Res. Space Phys. **115**(A10), A10248 (2010). https://doi.org/10.1029/2010JA015264

Y. Futaana, S. Barabash, M. Wieser, M. Holmström, C. Lue, P. Wurz, A. Schaufelberger, A. Bhardwaj, M.B. Dhanya, K. Asamura, Empirical energy spectra of neutralized solar wind protons from the lunar regolith. J. Geophys. Res. **117**, E05005 (2012). https://doi.org/10.1029/2011JE004019

Y. Futaana, S. Barabash, M. Wieser, C. Lue, P. Wurz, A. Vorburger, A. Bhardwaj, K. Asamura, Remote energetic neutral atom imaging of electric potential over a lunar magnetic anomaly. Geophys. Res. Lett. **40**, 262–266 (2013). https://doi.org/10.1002/grl.50135

E. Gaidos, N. Moskovitz, D.M. Williams, Terrestrial exoplanet light curves, in *Proc. International Astronomical Union Colloquium*, vol. 200 (2006), pp. 153–158. https://doi.org/10.1017/S1743921306009239

D. Gamborino, A. Vorburger, P. Wurz, Mercury's sodium exosphere: an ab initio calculation to interpret MESSENGER observations. Ann. Geophys. **37**, 455–470 (2019). https://doi.org/10.5194/angeo-2018-109

D.J. Gershman, J.A. Slavin, J.M. Raines, T.H. Zurbuchen, B.J. Anderson, H. Korth, D.N. Baker, S.C. Solomon, Magnetic flux pileup and plasma depletion in Mercury's subsolar magnetosheath. J. Geophys. Res. **118**, 7181–7199 (2013). https://doi.org/10.1002/2013JA019244

A. Goehlich, D. Gillmann, H.F. Döbele, Angular resolved energy distributions of sputtered atoms at low bombarding energy. Nucl. Instrum. Methods Phys. Res. B **164–165**, 834–839 (2000). https://doi.org/10.1016/S0168-583X(99)01106-4

W. Gonzalez, E. Parker (eds.), *Magnetic Reconnection: Concepts and Applications*. Astrophysics and Space Science Library, vol. 427 (Springer, Cham, 2016). 549 p. ISBN 9783319264301

J.T. Gosling, R.T. Hansen, S.J. Bame, Solar wind speed distributions: 1962–1970. J. Geophys. Res. **76**(7), 1811–1815 (1971). https://doi.org/10.1029/JA076i007p01811

J.T. Gosling, J.R. Asbridge, S.J. Bame, G. Paschmann, N. Sckopke, Observations of two distinct populations of bow shock ions in the upstream solar wind. Geophys. Res. Lett. **5**(11), 957–960 (1978). https://doi.org/10.1029/GL005i011p00957

J.N. Goswami, M. Annadurai, Chandrayaan-1 mission to the Moon. Acta Astronaut. **63**(11), 1215–1220 (2008). https://doi.org/10.1016/j.actaastro.2008.05.013

C. Grava, R.M. Killen, M. Benna, A.A. Berezhnoy, J.S. Halekas, F. Leblanc, M.N. Nishino, C. Plainaki, J.M. Raines, M. Sarantos, B.D. Teolis, O.J. Tucker, R.J. Vervack, A. Vorburger, Extreme volatiles and refractories in surface-bounded exospheres. Space Sci. Rev. **217**, 61 (2021). https://doi.org/10.1007/s11214-021-00833-8

E.W. Greenstadt, C.T. Russell, M. Hoppe, Magnetic field orientation and suprathermal ion streams in the Earth's foreshock. J. Geophys. Res. Space Phys. **85**(A7), 3473–3479 (1980). https://doi.org/10.1029/JA085iA07p03473

K.I. Gringauz, V.V. Bezrukikh, V.D. Ozerov, R.E. Ribchinsky, Some results of experiments in interplanetary space by means of charged particle traps on Soviet space probes. Space Res. **2**, 539–553 (1961)

E. Grün, M. Horanyi, Z. Sternovsky, The lunar dust environment. Planet. Space Sci. **59**, 1672–1680 (2011). https://doi.org/10.1016/j.pss.2011.04.005

M.N. Günther, Z. Zhan, S. Seager, P.B. Rimmer, S. Ranjan, K.G. Stassun, R.J. Oelkers, T. Daylan, E. Newton, M.H. Kristiansen, K. Olah, E. Gillen, S. Rappaport, G.R. Ricker, R.K. Vanderspek, D.W. Latham, J.N. Winn, J.M. Jenkins, A. Glidden, M. Fausnaugh, A.M. Levine, J.A. Dittmann, S.N. Quinn, A. Krishnamurthy, E.B. Ting, Stellar flares from the first TESS data release: exploring a new sample of M dwarfs. Astron. J. **159**, 60 (2020). https://doi.org/10.3847/1538-3881/ab5d3a

A.S. Hale, B. Hapke, A time-dependent model of radiative and conductive thermal energy transport in planetary regoliths with applications to the Moon and Mercury. Icarus **156**, 318–334 (2002). https://doi.org/10.1006/icar.2001.6768

J.S. Halekas, S.D. Bale, D.L. Mitchell, R.P. Lin, Electrons and magnetic fields in the lunar plasma wake. J. Geophys. Res. **110**, A07222 (2005). https://doi.org/10.1029/2004JA010991

J.S. Halekas, D.A. Brain, D.L. Mitchell, R.P. Lin, Whistler waves observed near lunar crustal magnetic sources. Geophys. Res. Lett. **33**, L22104 (2006). https://doi.org/10.1029/2006GL027684

J.S. Halekas, G.T. Delory, R.P. Lin, T.J. Stubbs, W.M. Farrell, Lunar Prospector observations of the electrostatic potential of the lunar surface and its response to incident currents. J. Geophys. Res. **113**, A09102 (2008a). https://doi.org/10.1029/2008JA013194

J.S. Halekas, D.A. Brain, R.P. Lin, D.L. Mitchell, Solar wind interaction with lunar crustal magnetic anomalies. Adv. Space Res. **41**(8), 1319–1324 (2008b). https://doi.org/10.1016/j.asr.2007.04.003

J.S. Halekas, V. Angelopoulos, D.G. Sibeck, K.K. Khurana, C.T. Russell, G.T. Delory, W.M. Farrell, J.P. McFadden, J.W. Bonnell, D. Larson, R.E. Ergun, F. Plaschke, K.H. Glassmeier, First results from ARTEMIS, a new two-spacecraft lunar mission: counter-streaming plasma populations in the lunar wake. Space Sci. Rev. **165**, 93–107 (2011). https://doi.org/10.1007/s11214-010-9738-8

J.S. Halekas, A.R. Poppe, W.M. Farrell, G.T. Delory, V. Angelopoulos, J.P. McFadden, J.W. Bonnell, K.H. Glassmeier, F. Plaschke, A. Roux, R.E. Ergun, Lunar precursor effects in the solar wind and terrestrial magnetosphere. J. Geophys. Res. **117**, A05101 (2012). https://doi.org/10.1029/2011JA017289

J.S. Halekas, A.R. Poppe, J.P. McFadden, K.-H. Glassmeier, The effects of reflected protons on the plasma environment of the moon for parallel interplanetary magnetic fields. Geophys. Res. Lett. **40**(17), 4544–4548 (2013). https://doi.org/10.1002/grl.50892

J.S. Halekas, A.R. Poppe, J.P. McFadden, The effects of solar wind velocity distributions on the refilling of the lunar wake: ARTEMIS observations and comparisons to one-dimensional theory. J. Geophys. Res. Space Phys. **119**, 5133–5149 (2014a). https://doi.org/10.1002/2014JA020083

J.S. Halekas, A.R. Poppe, J.P. McFadden, V. Angelopoulos, K.-H. Glassmeier, D.A. Brain, Evidence for small-scale collisionless shocks at the Moon from ARTEMIS. Geophys. Res. Lett. **41**, 7436–7443 (2014b). https://doi.org/10.1002/2014GL061973

J.S. Halekas, D.A. Brain, M. Holmström, M. Plasma Wake, in *Magnetotails in the Solar System*, ed. by e.A. Keiling, C.M. Jackman, P.A. Delamere (2015), pp. 149–167. https://doi.org/10.1002/9781118842324.ch9

B. Hapke, Space weathering from Mercury to the asteroid belt. J. Geophys. Res. **106**, 10039–10073 (2001). https://doi.org/10.1029/2000JE001338

Y. Harada, J.S. Halekas, Upstream waves and particles at the Moon, in *Low-Frequency Waves in Space Plasmas*, ed. by e.A. Keiling, D.-H. Lee, V. Nakariakov (2016). https://doi.org/10.1002/9781119055006.ch18

Y. Harada, S. Machida, Y. Saito, S. Yokota, K. Asamura, M.N. Nishino, T. Tanaka, H. Tsunakawa, H. Shibuya, F. Takahashi, M. Matsushima, H. Shimizu, Interaction between terrestrial plasma sheet electronsand the lunar surface: SELENE (Kaguya) observations. Geophys. Res. Lett. **37**, L19202 (2010). https://doi.org/10.1029/2010GL044574

Y. Harada, Y. Futaana, S. Barabash, M. Wieser, P. Wurz, A. Bhardwaj, K. Asamura, Y. Saito, S. Yokota, H. Tsunakawa, S. Machida, Backscattered energetic neutral atoms from the Moon in the Earth's plasma sheet observed by Chandarayaan-1/sub-keV atom reflecting analyzer instrument. J. Geophys. Res. **119**(5), 3573–3584 (2014a). https://doi.org/10.1002/2013JA019682

Y. Harada, J.S. Halekas, A.R. Poppe, S. Kurita, J.P. McFadden, Extended lunar precursor regions: electron-wave interaction. J. Geophys. Res. **119**, 9160–9173 (2014b). https://doi.org/10.1002/2014JA020618

R.A. Haring, A.W. Kolfschoten, A.E. De Vries, Chemical sputtering by keV ions. Nucl. Instrum. Methods Phys. Res. B **2**(1–3), 544–549 (1984). https://doi.org/10.1016/0168-583X(84)90263-5

W.K. Hartmann, Impact experiments, 1, ejecta velocity distributions and related results from regolith targets. Icarus **63**, 69–98 (1985). https://doi.org/10.1016/0019-1035(85)90021-1

G. Hayderer, M. Schmid, P. Varga, H. Winter, F. Aumayr, A highly sensitive quartz-crystal microbalance for sputtering investigations in slow ion–surface collisions. Rev. Sci. Instrum. **70**, 3696 (1999). https://doi.org/10.1063/1.1149979

P. Hedelt, Y. Ito, H.U. Keller, R. Reulke, P. Wurz, H. Lammer, H. Rauer, L. Esposito, Titan's atomic hydrogen corona. Icarus **210**, 424–435 (2010). https://doi.org/10.1016/j.icarus.2010.06.012

P. Heinzel, L. Kleint, Hydrogen balmer continuum in solar flares detected by the Interface Region Imaging Spectrograph (IRIS). Astrophys. J. Lett. **794**, L23 (2014). https://doi.org/10.1088/2041-8205/794/2/L23

D. Hercík, P.M. Trávnícek, Š. Štverák, P. Hellinger, Properties of Hermean plasma belt: numerical simulations and comparison with MESSENGER data. J. Geophys. Res. **121**, 413–431 (2016). https://doi.org/10.1002/2015JA021938

D. Heyner, C. Nabert, E. Liebert, K.-H. Glassmeier, Concerning reconnection-induction balance at the magnetopause of Mercury. J. Geophys. Res. Space Phys. **121**, 2935–2961 (2016). https://doi.org/10.1002/2015JA021484

H. Hijazi, M.E. Bannister, H.M. Meyer III, C.M. Rouleau, A.F. Barghouty, D.L. Rickman, F.W. Meyer, Anorthite sputtering by H^+ and Ar^{q+} (q=1-9) at solar wind velocities. J. Geophys. Res. Space Phys. **119**, 8006 (2014). https://doi.org/10.1002/2014JA020140

H. Hijazi, M.E. Bannister, H.M. Meyer III, C.M. Rouleau, F.W. Meyer, Kinetic and potential sputtering of an anorthite-like glassy thin film. J. Geophys. Res., Planets **122**, 1597 (2017). https://doi.org/10.1002/2017JE005300

F.L. Hinton, D.R. Taeusch, Variation of the lunar atmosphere with the strength of the solar wind. J. Geophys. Res. **69**(7), 1341–1347 (1964)

G.C. Ho, S.M. Krimigis, R.E. Gold, D.N. Baker, J.A. Slavin, B.J. Anderson, H. Lorth, R.D. Starr, D.J. Lawrence, R.R. McNutt, S.C. Solomon, MESSENGER observations of transient bursts of energetic electrons in Mercury's magnetosphere. Science **333**, 1865–1868 (2011a). https://doi.org/10.1126/science.1211141

G.C. Ho, R.D. Starr, R.E. Gold, S.M. Krimigis, J.A. Slavin, D.N. Baker, B.J. Anderson, R.L. McNutt, L.R. Nittler, S.C. Solomon, Observations of suprathermal electrons in Mercury's magnetosphere during the three MESSENGER flybys. Planet. Space Sci. **59**, 2016–2025 (2011b). https://doi.org/10.1016/j.pss.2011.01.011

G.C. Ho, R.D. Starr, S.M. Krimigis, J.D. Vandegriff, D.N. Baker, R.E. Gold, B.J. Anderson, H. Korth, D. Schriver, R.L. McNutt Jr., S.C. Solomon, MESSENGER observations of suprathermal electrons in Mercury's magnetosphere. Geophys. Res. Lett. **43**, 550–555 (2016). https://doi.org/10.1002/2015GL066850

R.R. Hodges Jr., Differential equation for exospheric lateral transportation and its application to terrestrial hydrogen. J. Geophys. Res. **78**(31), 7340–7346 (1973)

R.R. Hodges Jr., Methods for Monte Carlo simulation of the exospheres of the Moon and Mercury. J. Geophys. Res. **85**(A1), 164–169 (1980)

W.O. Hofer, Angular, energy, and mass distribution of sputtered particles, in *Sputtering by Particle Bombardment III*, ed. by R. Behrisch, K. Wittmaack. Topics in Applied Physics, vol. 64 (Springer, Berlin, 1991). https://doi.org/10.1007/3540534288_16

M. Holmström, M. Wieser, S. Barabash, Y. Futaana, A. Bhardwaj, Dynamics of solar wind protons reflected by the Moon. J. Geophys. Res. **115**, A06206 (2010). https://doi.org/10.1029/2009JA014843

K.A. Holsapple, The scaling of impact processes in planetary sciences. Annu. Rev. Earth Planet. Sci. **21**, 333–373 (1993). https://doi.org/10.1146/annurev.ea.21.050193.002001

K.A. Holsapple, K.R. Housten (2020). http://keith.aa.washington.edu/craterdata/scaling/index.htm

L.L. Hood, A. Zakharian, J. Halekas, D.L. Mitchell, R.P. Lin, M.H. Acuña, A.B. Binder, Initial mapping and interpretation of lunar crustal magnetic anomalies using Lunar Prospector magnetometer data. J. Geophys. Res. **106**(E11), 27825–27839 (2001). https://doi.org/10.1029/2000JE001366

K.R. Housen, R.M. Schmidt, K.A. Holsapple, Crater ejecta scaling laws: fundamental forms based on dimensional analysis. J. Geophys. Res. **88**(B3), 2485–2499 (1983). https://doi.org/10.1029/JB088iB03p02485

W.S. Howard, H. Corbett, N.M. Law, J.K. Ratzloff, N. Galliher, A.L. Glazier, R. Gonzalez, A.V. Soto, O. Fors, D. del Ser, J. Haislip, EvryFlare. III. Temperature evolution and habitability impacts of dozens of superflares observed simultaneously by evryscope and TESS. Astrophys. J. **902**, 115 (2020). https://doi.org/10.3847/1538-4357/abb5b4

H.S. Hudson, T.N. Woods, P.C. Chamberlin, L. Fletcher, G. Del Zanna, L. Didkovsky, N. Labrosse, D. Graham, The EVE Doppler sensitivity and flare observations. Sol. Phys. **273**, 69–80 (2011). https://doi.org/10.1007/s11207-011-9862-y

D.M. Hunten, T.M. Morgan, D.M. Shemansky, The Mercury Atmosphere, in *Mercury (A89-43751 19-91)* (University of Arizona Press, Tucson, 1988), pp. 562–612

W. Husinsky, The application of Doppler shift laser fluorescence spectroscopy for the detection and energy analysis of particles evolving from surfaces. J. Vac. Sci. Technol., B Microelectron. Process. Phenom. **3**, 1546 (1985). https://doi.org/10.1116/1.582983

W. Husinsky, I. Girgis, G. Betz, Doppler shift laser fluorescence spectroscopy of sputtered and evaporated atoms under Ar+ bombardment. J. Vac. Sci. Technol. B **3**, 1543–1545 (1985). https://doi.org/10.1116/1.582982

S.M. Imber, J.A. Slavin, MESSENGER observations of magnetotail loading and unloading: implications for substorms at Mercury. J. Geophys. Res. **122**(11), 402–411 (2017). https://doi.org/10.1002/2017JA024332. p. 412

W.-H. Ip, A. Kopp, MHD simulations of the solar wind interaction with Mercury. J. Geophys. Res. **107**(A11), 1348 (2002). https://doi.org/10.1029/2001JA009171

N. Jäggi, A. Galli, P. Wurz, H. Biber, P.S. Szabo, J. Brötzner, F. Aumayr, P.M.E. Tollan, K. Mezger, Creation of Lunar and Hermean analogue mineral powder samples for solar wind irradiation experiments and thermal infrared spectra analysis. Icarus **365**, 114492 (2021). https://doi.org/10.1016/j.icarus.2021.114492

D. Janches, A.A. Berezhnoy, A.A. Christou, G. Cremonese, T. Hirai, M. Horányi, J.M. Jasinski, M. Sarantos, Meteoroids as one of the sources for exosphere formation on airless bodies in the inner solar system. Space Sci. Rev. **217**, 50 (2021). https://doi.org/10.1007/s11214-021-00827-6

R. Jarvinen, M. Alho, E. Kallio, P. Wurz, S. Barabash, Y. Futaana, On vertical electric fields at lunar magnetic anomalies. Geophys. Res. Lett. **41**, 2243–2249 (2014). https://doi.org/10.1002/2014GL059788

J.M. Jasinski, J.A. Slavin, J.M. Raines, G.A. DiBraccio, Mercury's solar wind interaction as characterized by magnetospheric plasma mantle observations with MESSENGER. J. Geophys. Res. Space Phys. **122**, 12,153–12,169 (2017). https://doi.org/10.1002/2017JA024594

X. Jia, J.A. Slavin, T.I. Gombosi, L.K.S. Daldorff, G. Toth, B. van der Holst, Global MHD simulations of Mercury's magnetosphere with coupled planetary interior: induction effect of the planetary conducting core on the global interaction. J. Geophys. Res. Space Phys. **120**, 4763–4775 (2015). https://doi.org/10.1002/2015JA021143

X. Jia, J.A. Slavin, G. Poh, G.A. DiBraccio, G. Toth, Y. Chen, J.M. Raines, T.I. Gombosi, MESSENGER observations and global simulations of highly compressed magnetosphere events at Mercury. J. Geophys. Res. **124**, 229–247 (2019). https://doi.org/10.1029/2018JA026166

F.S. Johnson, Lunar atmosphere. Rev. Geophys. Space Phys. **9**(3), 813–823 (1971)

C.L. Johnson, M.E. Purucker, H. Korth, B.J. Anderson, R.M. Winslow, M.M.H. Al Asad, J.A. Slavin, I.I. Alexeev, R.J. Phillips, M.T. Zuber, S.C. Solomon, MESSENGER observations of Mercury's magnetic field structure. J. Geophys. Res. **117**, E00L14 (2012). https://doi.org/10.1029/2012JE004217

A.P. Jordan, Evidence for dielectric breakdown weathering on the Moon. Icarus **358**, 114199 (2021). https://doi.org/10.1016/j.icarus.2020.114199

A.P. Jordan, T.J. Stubbs, J.K. Wilson, N.A. Schwadron, H.E. Spence, Dielectric breakdown weathering of the Moon's polar regolith. J. Geophys. Res., Planets **120**, 210–225 (2015). https://doi.org/10.1002/2014JE004710

A.P. Jordan, T.J. Stubbs, J.K. Wilson, N.A. Schwadron, H.E. Spence, The rate of dielectric breakdown weathering of lunar regolith in permanently shadowed regions. Icarus **283**, 352–358 (2017). https://doi.org/10.1016/j.icarus.2016.08.027

K. Kabin, T.I. Gombosi, D.L. DeZeeuw, K.G. Powell, Interaction of Mercury with the solar wind. Icarus **143** 379–406 (2000). https://doi.org/10.1006/icar.1999.6252

E. Kallio, P. Janhunen, Solar wind and magnetospheric ion impact on Mercury's surface. Geophys. Res. Lett. **30**(17), 1877 (2003). https://doi.org/10.1029/2003GL017842

E. Kallio, P. Janhunen, The response of the Hermean magnetosphere to the interplanetary magnetic field. Adv. Space Res. **33**, 2176–2181 (2004). https://doi.org/10.1016/S0273-1177(03)00447-2

E. Kallio, P. Wurz, R. Killen, S. McKenna-Lawlor, A. Milillo, A. Mura, S. Massetti, S. Orsini, H. Lammer, P. Janhunen, W-H. Ip, On the impact of multiply charged heavy solar wind ions on the surface of Mercury, the Moon and Ceres. Planet. Space Sci. **56**, 1506–1516 (2008). https://doi.org/10.1016/j.pss.2008.07.018

E. Kallio, R. Järvinen, S. Dyadechkin, P. Wurz, S. Barabash, F. Alvarez, V. Fernandes, Y. Futaana, A.M. Harri, J. Heilimo, C. Lue, J. Mäkelä, N. Porjo, W. Schmidt, T. Silli, Kinetic simulations of finite gyroradius effects in the Lunar plasma environment on global, meso, and microscales. Planet. Space Sci. **74**, 146–155 (2012). https://doi.org/10.1016/j.pss.2012.09.012

E. Kallio, S. Dyadechkin, P. Wurz, M. Khodachenko, Space weathering on the Moon: farside-nearside solar wind precipitation asymmetry. Planet. Space Sci. **166**, 9–22 (2019). https://doi.org/10.1016/j.pss.2018.07.013

S. Kameda, I. Yoshikawa, M. Kagitani, S. Okano, Interplanetary dust distribution and temporal variability of Mercury's atmospheric Na. Geophys. Res. Lett. **36**, L15201 (2009). https://doi.org/10.1029/2009GL039036

Y. Kazama, S. Barabash, M. Wieser, K. Asamura, P. Wurz, in *An LENA Instrument Onboard BepiColombo and Chandrayaan-1*. AIP Conf. Proc. CP1144 (2009), pp. 109–113. https://doi.org/10.1063/1.3169273

R. Kelly, The surface binding energy in slow collisional sputtering. Nucl. Instrum. Methods Phys. Res. B **18**(1–6), 388–398 (1986). https://doi.org/10.1016/S0168-583X(86)80063-5

R.M. Killen, Source and maintenance of the argon atmospheres of Mercury and the Moon. Meteorit. Planet. Sci. **37**, 1223–1231 (2002). https://doi.org/10.1111/j.1945-5100.2002.tb00891.x

R.M. Killen, J.M. Hahn, Impact vaporization as a possible source of Mercury's calcium exosphere. Icarus **250**, 230–237 (2015). https://doi.org/10.1016/j.icarus.2014.11.035

R.M. Killen, W.-H. Ip, The surface-bounded atmospheres of Mercury and the Moon. Rev. Geophys. **37**, 361–406 (1999). https://doi.org/10.1029/1999RG900001

R.M. Killen, M. Sarantos, A.E. Potter, P. Reiff, Source rates and ion recycling rates for Na and K in Mercury's atmosphere. Icarus **171**, 1–19 (2004). https://doi.org/10.1016/j.icarus.2004.04.007

R. Killen, G. Cremonese, H. Lammer, S. Orsini, A.E. Potter, A.L. Sprague, P. Wurz, M. Khodachenko, H.I.M. Lichtenegger, A. Milillo, A. Mura, Processes that promote and deplete the exosphere of Mercury. Space Sci. Rev. **132**, 433–509 (2007). https://doi.org/10.1007/s11214-007-9232-0

R.M. Killen, D.M. Hurley, W.M. Farrell, The effect on the lunar exosphere of a coronal mass ejection passage. J. Geophys. Res. **117**, E00K02 (2012). https://doi.org/10.1029/2011JE004011

D. Koga, W.D. Gonzalez, V.M. Souza, F.R. Cardoso, C. Wang, Z.K. Liu, Dayside magnetopause reconnection: its dependence on solar wind and magnetosheath conditions. J. Geophys. Res. **124**, 8778–8787 (2019). https://doi.org/10.1029/2019JA026889

L. Kööp, P.R. Heck, H. Busemann, A.M. Davis, J. Greer, C. Maden, M.M.M. Meier, R. Wieler, High early solar activity inferred from helium and neon excesses in the oldest meteorite inclusions. Nat. Astron. **2**, 709–713 (2018). https://doi.org/10.1038/s41550-018-0527-8

P. Kotrč, O. Procházka, P. Heinzel, New observations of Balmer continuum flux in solar flares instrument description and first results. Sol. Phys. **291**, 779–789 (2016). https://doi.org/10.1007/s11207-016-0860-y

M. Kretzschmar, The Sun as a star: observations of white-light flares. Astron. Astrophys. **530**, A84 (2011). https://doi.org/10.1051/0004-6361/201015930

K.R. Kuhlman, K. Sridharan, A. Kvit, Simulation of solar wind space weathering in orthopyroxene. Planet. Space Sci. **115**, 110 (2015). https://doi.org/10.1016/j.pss.2015.04.003

M. Küster, W. Eckstein, V. Dose, J. Roth, The influence of surface roughness on the angular dependence of the sputter yield. Nucl. Instrum. Methods B **145**, 320–331 (2000)

M. Küstner, W. Eckstein, V. Dose, J. Roth, The influence of surface roughness on the angular dependence of the sputter yield. Nucl. Instrum. Methods Phys. Res., Sect. B, Beam Interact. Mater. Atoms **145**(3), 320–331 (1998). https://doi.org/10.1016/S0168-583X(98)00399-1

M. Küstner, W. Eckstein, E. Hechtl, J. Roth, Angular dependence of the sputtering yield of rough beryllium surfaces. J. Nucl. Mater. **265**, 22 (1999). https://doi.org/10.1016/S0022-3115(98)00648-5

H. Lammer, S.J. Bauer, Mercury's exosphere: origin of sputtering and implications. Planet. Space Sci. **45**, 73–79 (1997). https://doi.org/10.1016/S0032-0633(96)00097-9

H. Lammer, S. Bauer, *Planetary Aeronomy* (Springer, Berlin, 2004). ISBN-13 9783540214724

H. Lammer, P. Wurz, M.R. Patel, R. Killen, C. Kolb, S. Massetti, S. Orsini, A. Milillo, The variability of Mercury's exosphere by particle and radiation induced surface release processes. Icarus **166**(2), 238–247 (2003). https://doi.org/10.1016/j.icarus.2003.08.012

Y. Langevin, The regolith of Mercury: present knowledge and implications for the Mercury Orbiter mission. Planet. Space Sci. **45**(1), 31–37 (1997). https://doi.org/10.1016/S0032-0633(96)00098-0

D.J. Lawrence, B.J. Anderson, D.N. Baker, W.C. Feldman, G.C. Ho, H. Korth, R.L. McNutt Jr., P.N. Peplowski, S.C. Solomon, R.D. Starr, J.D. Vandegriff, R.M. Winslow, Comprehensive survey of energetic electron events in Mercury's magnetosphere with data from the MESSENGER Gamma-Ray and Neutron Spectrometer. J. Geophys. Res. Space Phys. **120**, 2851–2876 (2015). https://doi.org/10.1002/2014JA020792

F. Leblanc, R.E. Johnson, Mercury's sodium exosphere. Icarus **164**, 261–281 (2013). https://doi.org/10.1016/S0019-1035(03)00147-7

F. Leblanc, C. Schmidt, V. Mangano, A. Mura, G. Cremonese, J.M. Raines, J.M. Jasinski, M. Sarantos, A. Milillo, R.M. Killen, T. Cassidy, R.J. Vervack Jr., S. Kameda, M.T. Capria, M. Horanyi, D. Janches, A. Berezhnoy, A. Christou, T. Hirai, P. Lierle, J. Morgenthaler, Comparative Na and K Mercury and Moon exospheres. Space Sci. Rev. **218**, 2 (2022)

L.C. Lee, Z.F. Fu, A theory of magnetic flux transfer at the Earth's magnetopause. Geophys. Res. Lett. **12**(2), 105–108 (1985). https://doi.org/10.1029/GL012i002p00105

S.T. Lepri, T.H. Zurbuchen, Iron charge state distributions as an indicator of hot ICMEs: possible sources and temporal and spatial variations during solar maximum. J. Geophys. Res. **109**, A01112 (2004). https://doi.org/10.1029/2003JA009954

S.T. Lepri, T.H. Zurbuchen, Direct observational evidence of filament material within interplanetary coronal mass ejections. Astrophys. J. Lett. **723**, L22–L27 (2010). https://doi.org/10.1088/2041-8205/723/1/L22

R.P. Leyser, S.M. Imber, S.E. Milan, J.A. Slavin, The influence of IMF clock angle on dayside flux transfer events at Mercury. Geophys. Res. Lett. **44**, 10,829–10,837 (2017). https://doi.org/10.1002/2017GL074858

X. Li, F. Guo, H. Li, G. Li, Particle acceleration during magnetic reconnection in a low-beta plasma. Astrophys. J. **843**, 1 (2017). https://doi.org/10.3847/1538-4357/aa745e

R.P. Lin, D.L. Mitchell, D.W. Curtis, K.A. Anderson, C.W. Carlson, J. McFadden, M.H. Acuña, L.L. Hood, A. Binder, Lunar surface magnetic fields and their interaction with the solar wind: results from lunar prospector. Science **281**(5382), 1480–1484 (1998). https://doi.org/10.1126/science.281.5382.1480

S.T. Lindsay, M.K. James, E.J. Bunce, S.M. Imbera, H. Korth, A. Martindale, T.K. Yeoman, MESSENGER X-ray observations of magnetosphere–surface interaction on the nightside of Mercury. Planet. Space Sci. **125**, 72–79 (2016). https://doi.org/10.1016/j.pss.2016.03.005

M.J. Loeffler, C.A. Dukes, R.A. Baragiola, Irradiation of olivine by 4 keV He^+: simulation of space weathering by the solar wind. J. Geophys. Res. **114**, E03003 (2009). https://doi.org/10.1029/2008JE003249

E.A. Lucek, D. Constantinescu, M.L. Goldstein, J. Pickett, J.L. Pinçon, F. Sahraoui, R.A. Treumann, S.N. Walker, The magnetosheath. Space Sci. Rev. **118**, 95–152 (2005). https://doi.org/10.1007/s11214-005-3825-2

P.G. Lucey, D.T. Blewett, G.J. Taylor, B.R. Hawke, Imaging of lunar surface maturity. J. Geophys. Res. **105**(E8), 20377–20386 (2000). https://doi.org/10.1029/1999JE001110

C. Lue, Y. Futaana, S. Barabash, M. Wieser, M. Holmström, A. Bhardwaj, M.B. Dhanya, P. Wurz, Strong influence of lunar crustal fields on the solar wind flow. Geophys. Res. Lett. **38**, L03202 (2011). https://doi.org/10.1029/2010GL046215

C. Lue, Y. Futaana, S. Barabash, M. Wieser, A. Bhardwaj, P. Wurz, Chandrayaan-1 observations of backscattered solar wind protons from the lunar regolith: dependence on the solar wind speed. J. Geophys. Res., Planets **119**, 968–975 (2014). https://doi.org/10.1002/2013JE004582

C. Lue, Y. Futaana, S. Barabash, Y. Saito, M. Nishino, M. Wieser, K. Asamura, A. Bhardwaj, P. Wurz, Scattering characteristics and imaging of energetic neutral atoms from the Moon in the terrestrial magnetosheath. J. Geophys. Res. Space Phys. **121**(1), 432–445 (2016). https://doi.org/10.1002/2015JA021826

C. Lue, Y. Futaana, S. Barabash, M. Wieser, A. Bhardwaj, P. Wurz, K. Asamura, Solar wind scattering from the surface of Mercury: lessons from the Moon. Icarus **296**, 39–48 (2017). https://doi.org/10.1016/j.icarus.2017.05.019

C. Lue, J.S. Halekas, A.R. Poppe, J.P. McFadden, ARTEMIS observations of solar wind proton scattering off the lunar surface. J. Geophys. Res. Space Phys. **123**, 5289–5299 (2018). https://doi.org/10.1029/2018JA025486

E.F. Lyon, H.S. Bridge, J.H. Binsack, Explorer 35 plasma measurements in the vicinity of the Moon. J. Geophys. Res. **72**(23), 6113–6117 (1967). https://doi.org/10.1029/JZ072i023p06113

T.E. Madey, B.V. Yakshinskiy, V.N. Ageev, R.E. Johnson, Desorption of alkali atoms and ions from oxide surfaces: relevance to origins of Na and K in atmospheres of Mercury and the Moon. J. Geophys. Res. **103**(E3), 5873–5887 (1998). https://doi.org/10.1029/98JE00230

T.E. Madey, R.E. Johnson, T.M. Orlando, Far-out surface science: radiation-induced surface processes in the solar system. Surf. Sci. **500**, 838–858 (2002). https://doi.org/10.1016/S0039-6028(01)01556-4

H. Maehara, T. Shibayama, S. Notsu, Y. Notsu, T. Nagao, S. Kusaba, S. Honda, D. Nogami, K. Shibata, Superflares on solar-type stars. Nature **485**, 478–481 (2012). https://doi.org/10.1038/nature11063

H. Maehara, T. Shibayama, Y. Notsu, S. Notsu, S. Honda, D. Nogami, K. Shibata, Statistical properties of superflares on solar-type stars based on 1-min cadence data. Earth Planets Space **67**, 59 (2015). https://doi.org/10.1186/s40623-015-0217-z

A. Mallama, D. Wang, R.A. Howard, Photometry of Mercury from SOHO/LASCO and Earth: the phase function from 2 to 170°. Icarus **155**(2), 253–264 (2002). https://doi.org/10.1006/icar.2001.6723

V. Mangano, A. Milillo, A. Mura, S. Orsini, E. DeAngelis, A.M. DiLellis, P. Wurz, The contribution of impact-generated vapour to the hermean atmosphere. Planet. Space Sci. **55**(11), 1541–1556 (2007). https://doi.org/10.1016/j.pss.2006.10.008

S. Marchi, S. Mottola, G. Cremonese, M. Massironi, E. Martellato, A new chronology for the Moon and Mercury. Astron. J. **137**, 4936–4948 (2009). https://doi.org/10.1088/0004-6256/137/6/4936

E. Marsch, Kinetic physics of the solar corona and solar wind. Living Rev. Sol. Phys. **3**, 1 (2006). https://doi.org/10.12942/lrsp-2006-1

E. Marsch, K.-H. Mühlhäuser, R. Schwenn, H. Rosenbauer, W. Pilipp, F.M. Neubauer, Solar wind protons: three-dimensional velocity distributions and derived plasma parameters measured between 0.3 and 1 AU. J. Geophys. Res. Space Phys. **87**(A1), 52–72 (1982). https://doi.org/10.1029/JA087iA01p00052

R. Martinez, Th. Langlinay, C.R. Ponciano, E.F. da Silveira, M.E. Palumbo, G. Strazzulla, J.R. Brucato, H. Hijazi, A.N. Agnihotri, P. Boduch, A. Cassimi, A. Domaracka, F. Ropars, H. Rothard, Sputtering of sodium and potassium from nepheline: secondary ion yields and velocity spectra. Nucl. Instrum. Methods Phys. Res. B **406**, 523 (2017). https://doi.org/10.1016/j.nimb.2017.01.042

S. Massetti, S. Orsini, A. Milillo, A. Mura, E. De Angelis, H. Lammer, P. Wurz, Mapping of the cusp plasma precipitation on the surface of Mercury. Icarus **166**, 229–237 (2003). https://doi.org/10.1016/j.icarus.2003.08.005

S. Massetti, S. Orsini, A. Milillo, A. Mura, Modelling Mercury's magnetosphere and plasma entry through the dayside magnetopause. Planet. Space Sci. **55**, 1557–1568 (2007). https://doi.org/10.1016/j.pss.2006.12.008

S. Massetti, V. Mangano, A. Milillo, A. Mura, S. Orsini, C. Plainaki, Short-term observations of double-peaked Na emission from Mercury's exosphere. Geophys. Res. Lett. **44**, 2970–2977 (2017). https://doi.org/10.1002/2017GL073090

A. Masters, A more viscous-like solar wind interaction with all the giant planets. Geophys. Res. Lett. **45**, 7320–7329 (2018). https://doi.org/10.1029/2018GL078416

L. Matteini, P. Hellinger, S. Landi, P.M. Trávníček, M. Velli, Ion kinetics in the solar wind: coupling global expansion to local microphysics. Space Sci. Rev. **172**(1–4), 373–396 (2012). https://doi.org/10.1007/s11214-011-9774-z

G. Matthews, Celestial body irradiance determination from an underfilled satellite radiometer: application to albedo and thermal emission measurements of the Moon using CERES. Appl. Opt. **47**, 4981–4993 (2008). https://doi.org/10.1364/AO.47.004981

W.E. McClintock, R.J. Vervack Jr., E.T. Bradley, R.M. Killen, N. Mouawad, A.L. Sprague, M.H. Burger, S.C. Solomon, N.R. Izenberg, MESSENGER observations of Mercury's exosphere: detection of magnesium and distribution of constituents. Science **324**, 610–613 (2009). https://www.jstor.org/stable/20493836

D.J. McComas, F. Allegrini, P. Bochsler, M. Bzowski, M. Collier, H. Fahr, H. Fichtner, H. Funsten, S. Fuselier, G. Gloeckler, M. Gruntman, V. Izmodenov, P. Knappenberger, M. Lee, S. Livi, D. Mitchell, E. Möbius, T. Moore, S. Pope, D. Reisenfeld, E. Roelof, J. Scherrer, N. Schwadron, R. Tyler, M. Wieser, M. Witte, P. Wurz, G. Zank, IBEX—the interstellar boundary explorer. Space Sci. Rev. **146**, 11–33 (2009a). https://doi.org/10.1007/s11214-009-9499-4

D.J. McComas, F. Allegrini, P. Bochsler, P. Frisch, H.O. Funsten, M. Gruntman, P.H. Janzen, H. Kucharek, E. Möbius, D.B. Reisenfeld, N.A. Schwadron, Lunar backscatter and neutralization of the solar wind: first observations of neutral atoms from the Moon. Geophys. Res. Lett. **36**, L12105 (2009b). https://doi.org/10.1029/2009GL038794

G.M. McCracken, The behaviour of surfaces under ion bombardment. Rep. Prog. Phys. **38**(2), 241 (1975). https://doi.org/10.1088/0034-4885/38/2/002

J.L. McLain, A.L. Sprague, G.A. Grieves, D. Schriver, P. Travinicek, T.M. Orlando, Electron-stimulated desorption of silicates: a potential source for ions in Mercury's space environment. J. Geophys. Res. **116**, E03007 (2011). https://doi.org/10.1029/2010JE003714

M. Meftah, L. Damé, D. Bolsée, A. Hauchecorne, N. Pereira, D. Sluse, G. Cessateur, A. Irbah, J. Bureau, M. Weber, K. Bramstedt, T. Hilbig, R. Thiéblemont, M. Marchand, F. Lefèvre, A. Sarkissian, S. Bekki, SOLAR-ISS: a new reference spectrum based on SOLAR/SOLSPEC observation. Astron. Astrophys. **611**, A1 (2018). https://doi.org/10.1051/0004-6361/201731316

A.W. Merkel, R.J. Vervack Jr., R.M. Killen, T.A. Cassidy, W.E. McClintock, L.R. Nittler, M.H. Burger, Evidence connecting Mercury's magnesium exosphere to its magnesium-rich surface terrane. Geophys. Res. Lett. **45**, 6790–6797 (2018). https://doi.org/10.1029/2018GL078407

F.W. Meyer, P.R. Harris, C.N. Taylor, H.M. Meyer III, A.F. Barghouty, J.H. Adams, Sputtering of lunar regolith simulant by protons and singly and multicharged Ar ions at solar wind energies. Nucl. Instrum. Methods Phys. Res. B **269**, 1316 (2011). https://doi.org/10.1016/j.nimb.2010.11.091

A. Milillo, P. Wurz, S. Orsini, D. Delcourt, E. Kallio, R.M. Killen, H. Lammer, S. Massetti, A. Mura, S. Barabash, G. Cremonese, I.A. Daglis, E. DeAngelis, A.M. Di Lellis, S. Livi, V. Mangano, K. Torkar, Surface-exosphere-magnetosphere system of Mercury. Space Sci. Rev. **117**, 397–443 (2005). https://doi.org/10.1007/s11214-005-3593-z

A. Milillo, M. Fujimoto, G. Murakami, J. Benkhoff, J. Zender, S. Aizawa, M. Dósa, L. Griton, D. Heyner, G. Ho, S.M. Imber, X. Jia, T. Karlsson, R.M. Killen, M. Laurenza, S.T. Lindsay, S. McKenna-Lawlor, A. Mura, J.M. Raines, D.A. Rothery, N. André, W. Baumjohann, A. Berezhnoy, P.A. Bourdin, E.J. Bunce, F. Califano, J. Deca, S. de la Fuente, C. Dong, C. Grava, S. Fatemi, P. Henri, S.L. Ivanovski, B.V. Jackson, M. James, E. Kallio, Y. Kasaba, E. Kilpua, M. Kobayashi, B. Langlais, F. Leblanc, C. Lhotka, V. Mangano, A. Martindale, S. Massetti, A. Masters, M. Morooka, Y. Narita, J.S. Oliveira, D. Odstrcil, S. Orsini, M.G. Pelizzo, C. Plainaki, F. Plaschke, F. Sahraoui, K. Seki, J.A. Slavin, R. Vainio, P. Wurz, S. Barabash, C.M. Carr, D. Delcourt, K.-H. Glassmeier, M.N. Grande, M. Hirahara, J. Huovelin, O. Korablev, H. Kojima, H. Lichtenegger, S. Livi, A. Matsuoka, R. Moissl, M. Moncuquet, K. Muinonen, E. Quèmerais, Y. Saito, S. Yagitani, I. Yoshikawa, J.-E. Wahlund, Investigating Mercury's environment with the two-spacecraft BepiColombo mission. Space Sci. Rev. **216**, 93 (2020). https://doi.org/10.1007/s11214-020-00712-8

D.L. Mitchell, J.S. Halekas, R.P. Lin, S. Frey, L.L. Hood, M.H. Acuna, A. Binder, Global mapping of lunar crustal magnetic fields by Lunar Prospector. Icarus **194**(2), 401–409 (2008). https://doi.org/10.1016/j.icarus.2007.10.027

W. Möller, W. Eckstein, Tridyn—a TRIM simulation code including dynamic composition changes. Nucl. Instrum. Methods Phys. Res. B **2**(1–3), 814–818 (1984). https://doi.org/10.1016/0168-583X(84)90321-5

C.S. Moore, P.C. Chamberlin, R. Hock, Measurements and modelling of total solar irradiance in X-class solar flares. Astron. J. **787**, 32 (2014). https://doi.org/10.1088/0004-637X/787/1/32

R.V. Morris, Fine-grained metal distribution in grain-size separates of lunar soils: production and evolution of the fine-grained metal. Lunar Planet. Sci. Conf. **8**, 682–684 (1977)

L.S. Morrissey, O.J. Tucker, R.M. Killen, S. Nakhla, D.W. Savin, Solar wind ion sputtering of sodium from silicates using molecular dynamics calculations of surface binding energies. Astrophys. J. Lett. **925**, L6 (2022). https://doi.org/10.3847/2041-8213/ac42d8

S.-P. Moschou, J.J. Drake, O. Cohen, J.D. Alvarado-Gómez, C. Garraffo, F. Fraschetti, The stellar CME–flare relation: what do historic observations reveal? Astrophys. J. **877**, 105 (2019). https://doi.org/10.3847/1538-4357/ab1b37

M. Müller, S.F. Green, N. McBride, D. Koschny, J.C. Zarnecki, M.S. Bentley, Estimation of the dust flux near Mercury. Planet. Space Sci. **50**, 1101–1115 (2002). https://doi.org/10.1016/S0032-0633(02)00048-X

J. Müller, S. Simon, J.-C. Wang, U. Motschmann, D. Heyner, J. Schüle, W.-H. Ip, G. Kleindienst, G.J. Pringle, Origin of Mercury's double magnetopause: 3D hybrid simulation study with A.I.K.E.F. Icarus **218**, 666–687 (2012). https://doi.org/10.1016/j.icarus.2011.12.028

A. Mura, S. Orsini, A. Milillo, D. Delcourt, S. Massetti, E. De Angelis, Dayside H^+ circulation at Mercury and neutral particle emission. Icarus **175**(2), 305–319 (2005). https://doi.org/10.1016/j.icarus.2004.12.010

A. Mura, P. Wurz, H.I.M. Lichtenegger, H. Schleicher, H. Lammer, D. Delcourt, A. Milillo, S. Orsini, S. Massetti, M.L. Khodachenko, The sodium exosphere of Mercury: comparison between observations during Mercury's transit and model results. Icarus **200**, 1–11 (2009). https://doi.org/10.1016/j.icarus.2008.11.014

F.H. Murcray, D.G. Murcray, W.J. Williams, Infrared emissivity of lunar surface features: 1. Balloon-borne observations. J. Geophys. Res. **75**(14), 2662–2669 (1970). https://doi.org/10.1029/JB075i014p02662

A. Mutzke, R. Schneider, I. Bizyukov, SDTrimSP-2D studies of the influence of mutual flux arrangement on erosion and deposition. J. Nucl. Mater. **390–391**, 115–118 (2009). https://doi.org/10.1016/j.jnucmat.2009.01.133

A. Mutzke, R. Schneider, W. Eckstein, R. Dohmen SDTrimSP Version 5.00. IPP-Report (2011). https://pure.mpg.de/rest/items/item_2139848/component/file_2139847/content

A. Mutzke, R. Schneider, W. Eckstein, R. Dohmen, K. Schmid, U.V. Toussaint, G. Badelow *SDTrimSP Version 6.00 (IPP 2019-02)* (Max-Planck-Institut für Plasmaphysik, Garching, 2019). https://doi.org/10.17617/2.3026474

T. Nakagawa, ULF/ELF waves in near-Moon space, in *Low-Frequency Waves in Space Plasmas*, ed. by A. Keiling, D.-H. Lee, V. Nakariakov (2016). https://doi.org/10.1002/9781119055006.ch17

T. Nakagawa, F. Takahashi, H. Tsunakawa, H. Shibuya, H. Shimizu, M. Matsushima, Non-monochromatic whistler waves detected by Kaguya on the dayside surface of the Moon. Earth Planets Space **63**(1), 37–46 (2011). https://doi.org/10.5047/eps.2010.01.005. 3rd Kaguya Science Meeting on Earth, Planets and Space, Tokyo, January 14–15, 2009

T. Nakagawa, A. Nakayama, F. Takahashi, H. Tsunakawa, H. Shibuya, H. Shimizu, M. Matsushima, Large-amplitude monochromatic ULF waves detected by Kaguya at the Moon. J. Geophys. Res. **117**, A04101 (2012). https://doi.org/10.1029/2011JA017249

K. Namekata, T. Sakaue, K. Watanabe, A. Asai, H. Maehara, Y. Notsu, S. Notsu, S. Honda, T.T. Ishii, K. Ikuta, D. Nogami, K. Shibata, Statistical studies of solar white-light flares and comparisons with superflares on solar-type stars. Astrophys. J. **851**, 91 (2017). https://doi.org/10.3847/1538-4357/aa9b34

H. Niehus, W. Heiland, E. Taglauer, Low-energy ion scattering at surfaces. Surf. Sci. Rep. **17**(4–5), 213–303 (1993). https://doi.org/10.1016/0167-5729(93)90024-J

M.N. Nishino, K. Maezawa, M. Fujimoto, Y. Saito, S. Yokota, K. Asamura, T. Tanaka, H. Tsunakawa, M. Matsushima, F. Takahashi, T. Terasawa, H. Shibuya, H. Shimizu, Pairwise energy gain-loss feature of solar wind protons in the near-Moon wake. Geophys. Res. Lett. **36**(12), L12108 (2009a). https://doi.org/10.1029/2009GL039049

M.N. Nishino, M. Fujimoto, K. Maezawa, Y. Saito, S. Yokota, K. Asamura, T. Tanaka, H. Tsunakawa, M. Matsushima, F. Takahashi, T. Terasawa, H. Shibuya, H. Shimizu, Solar-wind proton access deep into the near-Moon wake. Geophys. Res. Lett. **36**(16), L16103 (2009b). https://doi.org/10.1029/2009GL039444

M.N. Nishino, Y. Harada, Y. Saito, H. Tsunakawa, F. Takahashi, S. Yokota, M. Matsushima, H. Shibuya, H. Shimizu, Kaguya observations of the lunar wake in the terrestrial foreshock: surface potential change by bow-shock reflected ions. Icarus **293**, 45–51 (2017). https://doi.org/10.1016/j.icarus.2017.04.005

L.R. Nittler, S.Z. Weider, The surface composition of Mercury. Elements **15**, 33–38 (2019). https://doi.org/10.2138/gselements.15.1.33

S.K. Noble, C.M. Pieters, L.P. Keller, An experimental approach to understanding the optical effects of space weathering. Icarus **192**, 629–642 (2007). https://doi.org/10.1016/j.icarus.2007.07.021

D. Nogami, Y. Notsu, S. Honda, H. Maehara, S. Notsu, T. Shibayama, K. Shibata, Two Sun-like superflare stars rotating as slow as the Sun. Publ. Astron. Soc. Jpn. **66**(2), L4 (2014). https://doi.org/10.1093/pasj/psu012

Y. Notsu, T. Shibayama, H. Maehara, S. Notsu, T. Nagao, S. Honda, T.T. Ishii, D. Nogami, K. Shibata, Superflares on solar-type stars observed with Kepler II. Photometric variability of superflare-generating stars: a signature of stellar rotation and starspots. Astrophys. J. **771**, 127 (2013). https://doi.org/10.1088/0004-637X/771/2/127

Y. Notsu, H. Maehara, S. Honda, S.L. Hawley, J.R.A. Davenport, K. Namekata, S. Notsu, K. Ikuta, D. Nogami, K. Shibata, Do Kepler superflare stars really include slowly rotating Sun-like stars?—Results using APO 3.5 m telescope spectroscopic observations and Gaia-DR2 data. Astrophys. J. **876**, 58 (2019). https://doi.org/10.3847/1538-4357/ab14e6

K.W. Ogilvie, J.T. Steinberg, R.J. Fitzenreiter, C.J. Owen, A.J. Lazarus, W.M. Farrell, R.B. Torbert, Observations of the lunar plasma wake from the WIND spacecraft on December 27, 1994. Geophys. Res. Lett. **23**(10), 1255–1258 (1996). https://doi.org/10.1029/96GL01069

M. Øieroset, T.D. Phan, R.P. Lin, B.U. Sonnerup, Walén and variance analyses of high-speed flows observed by Wind in the midtail plasma sheet: evidence for reconnection. J. Geophys. Res. **105**(A11), 25247–25263 (2002). https://doi.org/10.1029/2000JA900075

T. Okada, K. Shirai, Y. Yamamoto, T. Arai, K. Ogawa, H. Shiraishi, M. Iwasaki, T. Kawamura, H. Morito, M. Grande, M. Kato, X-ray fluorescence spectrometry of Lunar surface by XRS onboard SELENE (Kaguya). Trans. Jpn. Soc. Aeronaut. Space Sci. **7**, 39–42 (2009). https://doi.org/10.2322/tstj.7.Tk_39

N. Omidi, J.P. Eastwood, D.G. Sibeck, Foreshock bubbles and their global magnetospheric impacts. J. Geophys. Res. Space Phys. **115**, A6 (2010). https://doi.org/10.1029/2009JA014828

N. Omidi, D. Sibeck, X. Blanco-Cano, D. Rojas-Castillo, D. Turner, H. Zhang, P. Kajdič, Dynamics of the foreshock compressional boundary and its connection to foreshock cavities. J. Geophys. Res. Space Phys. **118**(2), 823–831 (2013). https://doi.org/10.1002/jgra.50146

S. Orsini, V. Mangano, A. Mura, D. Turrini, S. Massetti, A. Milillo, C. Plainaki, The influence of space environment on the evolution of Mercury. Icarus **239**, 281–290 (2014). https://doi.org/10.1016/j.icarus.2014.05.031

S. Orsini, V. Mangano, A. Milillo, C. Plainaki, A. Mura, J.M. Raines, E. De Angelis, R. Rispoli, F. Lazzarotto, A. Aronica, Mercury sodium exospheric emission as a proxy for solar perturbations transit. Sci. Rep. **8**, 928 (2018). https://doi.org/10.1038/s41598-018-19163-x

S. Orsini, S. Livi, H. Lichtenegger, S. Barabash, A. Milillo, E. De Angelis, M. Phillips, G. Laky, M. Wieser, A. Olivieri, C. Plainaki, G. Ho, R.M. Killen, J.A. Slavin, P. Wurz, J.-J. Berthelier, I. Dandouras, M. Dosa, E. Kallio, S. McKenna-Lawlor, K. Torkar, O. Vaisberg, F. Allegrini, I.A. Daglis, C. Dong, C.P. Escoubet, S. Fatemi, M. Fränz, S. Ivanovski, N. Krupp, H. Lammer, F. Leblanc, V. Mangano, A. Mura, H. Nilsson, J.M. Raines, R. Rispoli, M. Sarantos, H.T. Smith, K. Szego, A. Varsani, A. Aronica, F. Camozzi, A.M. Di Lellis, G. Fremuth, F. Giner, R. Gurnee, J. Hayes, H. Jeszenszky, F. Tominetti, B. Trantham, J. Balaz, W. Baumjohann, D. Brienza, U. Bührke, M.-D. Bush, M. Cantatore, S. Cibella, L. Colasanti, G. Cremonese, L. Cremonesi, M. D'Alessandro, D. Delcourt, M. Delva, M. Desai, M. Famá, M. Ferris, H. Fischer, A. Gaggero, D. Gamborino, P. Garnier, B. Gibson, R. Goldstein, M. Grande, V. Grishin, D. Haggerty, M. Holmström, I. Horvath, K.C. Hsieh, A. Jacques, R.E. Johnson, A. Kazakov, K. Kecskemety, H. Krüger, C. Kürbisch, F. Lazzarotto, F. Leblanc, M. Leichtfried, R. Leoni, A. Loose, D. Maschietti, S. Massetti, F. Mattioli, G. Miller, D. Moissenko, A. Morbidini, R. Noschese, F. Nuccilli, C. Nunez, N. Paschalidis, S. Persyn, D. Piazza, M. Oja, J. Ryno W, Schmidt, J.A. Scheer, A. Shestakov, S.S. Shuvalov, K. Seki, S. Selci, K. Smith, R. Sordini, F. Stenbeck, J. Svensson, L. Szalai, K. Szego, D. Toublanc, C. Urdiales, N. Vertolli, R. Wallner, P. Wahlstroem, P. Wilson, S. Zampieri, SERENA: particle instrument suite for determining the Sun-Mercury interaction from BepiColombo. Space. Sci. Rev. **217**(11) (2021). https://doi.org/10.1007/s11214-020-00787-3

C. Pahlke, H. Düsterhöft, U. Müller-Jahreis, Measurements of the energy distributions of positive secondary ions in the energy range from 0 eV to about 500 eV, in *Secondary Ion Mass Spectrometry SIMS III* (Springer, Berlin, 1982), pp. 124–127

M. Pfleger, H.I.M. Lichtenegger, P. Wurz, H. Lammer, E. Kallio, M. Alho, A. Mura, S. McKenna-Lawlor, J.A. Martín-Fernández, 3D-modeling of Mercury's solar wind sputtered surface-exosphere environment. Planet. Space Sci. **115**, 90–101 (2015). https://doi.org/10.1016/j.pss.2015.04.016

C.M. Pieters, S.K. Noble, Space weathering on airless bodies. J. Geophys. Res. **121**, 1865–1884 (2016). https://doi.org/10.1002/2016JE005128

G. Poh, J.A. Slavin, X. Jia, G.A. DiBraccio, J.M. Raines, S.M. Imber, D.J. Gershman, W.-J. Sun, B.J. Anderson, H. Korth, T.H. Zurbuchen, R.L. McNutt Jr., S.C. Solomon, MESSENGER observations of cusp plasma filaments at Mercury. J. Geophys. Res. Space Phys. **121**, 8260–8285 (2016). https://doi.org/10.1002/2016JA022552

G. Poh, J.A. Slavin, X. Jia, J.M. Raines, S.M. Imber, W.-J. Sun, D.J. Gershman, G.A. DiBraccio, K.J. Genestreti, A.W. Smith, Mercury's cross-tail current sheet: structure, X-line location and stress balance. Geophys. Res. Lett. **44**, 678–686 (2017). https://doi.org/10.1002/2016GL071612

P. Pokorný, M. Sarantos, D. Janches, A comprehensive model of the meteoroid environment around Mercury. Astrophys. J. **863**, 31 (2018). https://doi.org/10.3847/1538-4357/aad051

P. Pokorný, D. Janches, M. Sarantos, J.R. Szalay, M. Horányi, D. Nesvorný, M.J. Kuchner, Meteoroids at the Moon: orbital properties, surface vaporization, and impact ejecta production. J. Geophys. Res. **124**, 752–778 (2019). https://doi.org/10.1029/2018JE005912

A.R. Poppe, S. Fatemi, J.S. Halekas, M. Holmström, G.T. Delory, ARTEMIS observations of extreme diamagnetic fields in the lunar wake. Geophys. Res. Lett. **41**(11), 3766–3773 (2014). https://doi.org/10.1002/2014GL060280

A.R. Poppe, S. Fatemi, I. Garrick-Bethell, D. Hemingway, M. Holmström, Solar wind interaction with the Reiner Gamma crustal magnetic anomaly: connecting source magnetization to surface weathering. Icarus **266**, 261–266 (2016a). https://doi.org/10.1016/j.icarus.2015.11.005

A.R. Poppe, M.O. Fillingim, J.S. Halekas, J. Raeder, V. Angelopoulos, ARTEMIS observations of terrestrial ionospheric molecular ion outflow at the Moon. Geophys. Res. Lett. **43**, 6749–6758 (2016b). https://doi.org/10.1002/2016GL069715

A.R. Poppe, J.S. Halekas, C. Lue, S. Fatemi, ARTEMIS observations of the solar wind proton scattering function from lunar crustal magnetic anomalies. J. Geophys. Res., Planets **122**(4), 771–783 (2017). https://doi.org/10.1002/2017JE005313

A.R. Poppe, W.M. Farrell, J.S. Halekas, Formation timescales of amorphous rims on lunar grains derived from ARTEMIS observations. J. Geophys. Res., Planets **123**, 37–46 (2018). https://doi.org/10.1002/2017JE005426

A.E. Potter, Chemical sputtering could produce sodium vapor and ice on Mercury. Geophys. Res. Lett. **22**(23), 3289–3292 (1995). https://doi.org/10.1029/95GL03181

A.E. Potter, R.M. Killen, T.H. Morgan, Solar radiation acceleration effects on Mercury sodium emission. Icarus **186**, 571–580 (2007). https://doi.org/10.1016/j.icarus.2006.09.025

J.M. Raines, D.J. Gershman, J.A. Slavin, T.H. Zurbuchen, H. Korth, B.J. Anderson, S.C. Solomon, Structure and dynamics of Mercury's magnetospheric cusp: MESSENGER measurements of protons and planetary ions. J. Geophys. Res. Space Phys. **119**, 6587–6602 (2014). https://doi.org/10.1002/2014JA020120

J.M. Raines, G.A. DiBraccio, T.A. Cassidy, D.C. Delcourt, M. Fujimoto, X. Jia, V. Mangano, A. Milillo, M. Sarantos, J.A. Slavin, P. Wurz, Plasma sources in planetary magnetospheres: Mercury. Space Sci. Rev. **192**(1), 1–54 2015. https://doi.org/10.1007/s11214-015-0193-4

J.M. Raines, R.M. Dewey, N.M. Staudacher, P.J. Tracy, C.M. Bert, M. Sarantos, D.J. Gershman, J.M. Jasinski, J.M. Slavin, Proton precipitation in Mercury's northern magnetospheric cusp. J. Geophys. Res. (2022), submitted

J.M. Raines, R.M. Dewey, N.M. Staudacher, P.J. Tracy, C.M. Bert, M. Sarantos, D.J. Gershman, J.M. Jasinski, J.M. Slavin, Proton precipitation in Mercury's northern magnetospheric cusp. J. Geophys. Res. (2022, submitted)

R.D. Ramsier, J.T. Yates, Electron-stimulated desorption: principles and applications. Surf. Sci. Rep. **6–8**, 243–378 (1991). https://doi.org/10.1016/0167-5729(91)90013-N

E. Richer, R. Modolo, G.M. Chanteur, S. Hess, F. Leblanc, A global hybrid model for Mercury's interaction with the solar wind: case study of the dipole representation. J. Geophys. Res. **117**, A10228 (2012). https://doi.org/10.1029/2012JA017898

N.C. Richmond, L.L. Hood, A preliminary global map of the vector lunar crustal magnetic field based on Lunar Prospector magnetometer data. J. Geophys. Res. **113**, E02010 (2008). https://doi.org/10.1029/2007JE002933

D.F. Rodríguez M., L. Saul, P. Wurz, S.A. Fuselier, H.O. Funsten, D.J. McComas, E. Möbius, IBEX-Lo observations of energetic neutral hydrogen atoms originating from the lunar surface. Planet. Space Sci. **60**(1), 297–303 (2012). https://doi.org/10.1016/j.pss.2011.09.009

J. Roth, J. Bohdansky, W. Ottenberger, *Data on Low Energy Light Ion Sputtering* (Max-Planck-Inst. für Plasmaphysik, Garching bei München, 1979). http://hdl.handle.net/11858/00-001M-0000-0027-6AE8-3

C.T. Russell, D.N. Baker, J.A. Slavin, The magnetosphere of Mercury, in *Mercury* (University of Arizona Press, Tucson, 1988), pp. 514–561

J.M. Saari, R.W. Shorthill, The sunlit lunar surface. I. Albedo studies and full Moon temperature distribution. Moon **5**(1–2), 161–178 (1972)

Y. Saito, S. Yokota, T. Tanaka, K. Asamura, M.N. Nishino, M. Fujimoto, H. Tsunakawa, H. Shibuya, M. Matsushima, H. Shimizu, F. Takahashi, T. Mukai, T. Terasawa, Solar wind proton reflection at the lunar surface: low energy ion measurement by MAP-PACE onboard SELENE (KAGUYA). Geophys. Res. Lett. **35**, L24205 (2008). https://doi.org/10.1029/2008GL036077

Y. Saito, S. Yokota, K. Asamura, T. Tanaka, M.N. Nishino, T. Yamamoto, Y. Terakawa, M. Fujimoto, H. Hasegawa, H. Hayakawa, M. Hirahara, M. Hoshino, S. Machida, T. Mukai, T. Nagai, T. Nagatsuma, T. Nakagawa, M. Nakamura, K. Oyama, E. Sagawa, S. Sasaki, K. Seki, I. Shinohara, T. Terasawa, H. Tsunakawa, H. Shibuya, M. Matsushima, H. Shimizu, F. Takahashi, In-flight performance and initial results of plasma energy angle and composition experiment (PACE) on SELENE (Kaguya). Space Sci. Rev. **154**, 265–303 (2010). https://doi.org/10.1007/s11214-010-9647-x

Y. Saito, M.N. Nishino, M. Fujimoto, T. Yamamoto, S. Yokota, H. Tsunakawa, H. Shibuya, M. Matsushima, H. Shimizu, F. Takahashi, Simultaneous observavation of the electron acceleration and ion deceleration over lunar magnetic anomalies. Earth Planets Space **64**, 83–92 (2012). https://doi.org/10.5047/eps.2011.07.011

Y. Saito, D. Delcourt, M. Hirahara, S. Barabash, N. André, T. Takashima, K. Asamura, S. Yokota, M. Wieser, M.N. Nishino, M. Oka, Y. Futaana, Y. Harada, J.-A. Sauvaud, P. Louarn, B. Lavraud, V. Génot, C. Mazelle, I. Dandouras, C. Jacquey, C. Aoustin, A. Barthe, A. Cadu, A. Fedorov, A.-M. Frezoul, C. Garat, E. Le Comte, Q.-M. Lee, J.-L. Médale, D. Moirin, E. Penou, M. Petiot, G. Peyre, J. Rouzaud, H.-C. Séran, Z. Němeček, J. Safránková, M.F. Marcucci, R. Bruno, G. Consolini, W. Miyake, I. Shinohara, H. Hasegawa, K. Seki, A.J. Coates, F. Leblanc, C. Verdeil, B. Katra, D. Fontaine, J.-M. Illiano, J.-J. Berthelier, J.-D. Techer, M. Fraenz, H. Fischer, N. Krupp, J. Woch, U. Bührke, B. Fiethe, H. Michalik, H.M.T. Yanagimachi, Y. Miyoshi, T. Mitani, M. Shimoyama, Q. Zong, P. Wurz, H. Andersson, S. Karlsson, M. Holmström, Y. Kazama, W.-H. Ip, M. Hoshino, M. Fujimoto, N. Terada, K. Keika the Bepi-Colombo Mio/MPPE Team, Pre-flight calibration and near-Earth commissioning results of the Mercury Plasma Particle Experiment (MPPE) onboard MMO (Mio). Space Sci. Rev. **217**, 70 (2021). https://doi.org/10.1007/s11214-021-00839-2

M. Sarantos, R.M. Killen, A.S. Sharma, J.A. Slavin, Influence of plasma ions on source rates for the lunar exosphere during passage through the Earth's magnetosphere. Geophys. Res. Lett. **35**, L04105 (2008). https://doi.org/10.1029/2007GL032310

M. Sarantos, R.M. Killen, A. Surjalal Sharma, J.A. Slavin, Sources of sodium in the lunar exosphere: modeling using ground-based observations of sodium emission and spacecraft data of the plasma. Icarus **205**, 364–374 (2010). https://doi.org/10.1016/j.icarus.2009.07.039

L. Saul, P. Wurz, A. Vorburger, D.F. Rodríguez M., S.A. Fuselier, D.J. McComas, E. Möbius, S. Barabash, H. Funsten, P. Janzen, Solar wind reflection from the lunar surface: the view from far and near. Planet. Space Sci. **84**, 1–4 (2013). https://doi.org/10.1016/j.pss.2013.02.004

P. Saxena, R.M. Killen, V. Airapetian, N.E. Petro, N.M. Curran, A.M. Mandell, Was the Sun a slow rotator? Sodium and potassium constraints from the lunar regolith. Astrophys. J. Lett. **876**, L16 (2019). https://doi.org/10.3847/2041-8213/ab18fb

M.J. Schaible, C.A. Dukes, A.C. Hutcherson, P. Lee, M.R. Collier, R.E. Johnson, Solar wind sputtering rates of small bodies and ion mass spectrometry detection of secondary ions. J. Geophys. Res., Planets **122**, 1968–1983 (2017). https://doi.org/10.1002/2017JE005359

M.J. Schaible, M. Sarantos, B.A. Anzures, S.W. Parman, T.M. Orlando, Photon-stimulated desorption of MgS as a potential source of sulfur in Mercury's exosphere. J. Geophys. Res., Planets **125**, e2020JE006479 (2020). https://doi.org/10.1029/2020JE006479

A. Schaufelberger, P. Wurz, S. Barabash, M. Wieser, Y. Futaana, M. Holmström, A. Bhardwaj, M.B. Dhanya, R. Sridharan, K. Asamura, Scattering function for energetic neutral hydrogen atoms off the lunar surface. Geophys. Res. Lett. **38**, L22202 (2011). https://doi.org/10.1029/2011GL049362

T. Schenkel, A.V. Hamza, A.V. Barnes, D.H. Schneider, Interaction of slow, very highly charged ions with surfaces. Prog. Surf. Sci. **61**, 23 (1999). https://doi.org/10.1016/S0079-6816(99)00009-X

C.E. Schlemm, R.D. Starr, G.C. Ho, K.E. Bechtold, S.A. Hamilton, J.D. Boldt, W.V. Boynton, W. Bradley, M.E. Fraeman, R.E. Gold, J.O. Goldsten, J.R. Hayes, S.E. Jaskulek, E. Rossano, R.A. Rumpf, E.D. Schaefer, K. Strohben, R.G. Shelton, R.E. Thompson, J.I. Trombka, B.D. Williams, The X-ray spectrometer on the MESSENGER spacecraft, in *The Messenger Mission to Mercury*, ed. by D.L. Domingue, C.T. Russell (Springer, New York, 2007). https://doi.org/10.1007/s11214-007-9248-5

C.A. Schmidt, J. Baumgardner, M. Mendillo, J.K. Wilson, Escape rates and variability constraints for high-energy sodium sources at Mercury. J. Geophys. Res. **117**, A03301 (2012). https://doi.org/10.1029/2011JA017217

N. Schörghofer, M. Benna, A.A. Berezhnoy, B. Greenhagen, B.M. Jones, S. Li, T.M. Orlando, P. Prem, O.J. Tucker, C. Wöhler, Water group exospheres and surface interactions on the Moon, Mercury, and Ceres. Space Sci. Rev. **217**, 74 (2021). https://doi.org/10.1007/s11214-021-00846-3

C.J. Schrijver, P.M. Trávnícek, B.J. Anderson, M. Ashour-Abdalla, D. Baker, M. Benna, S.A. Boardsen, R.E. Gold, P. Hellinger, G.C. Ho, H. Korth, S.M. Krimigis, R.L. McNutt Jr., J.M. Raines, R.L. Richards, J.A. Slavin, S.C. Solomon, R.D. Starr, T.H. Zurbuchen, Quasi-trapped ion and electron populations at Mercury. Geophys. Res. Lett. **38**, L23103 (2011). https://doi.org/10.1029/2011GL049629

C.J. Schrijver, J. Beer, U. Baltensperger, E.W. Cliver, M. Güdel, H.S. Hudson, K.G. McCracken, R.A. Osten, T. Peter, D.R. Soderblom, I.G. Usoskin, E.W. Wolff, Estimating the frequency of extremely energetic solar events, based on solar, stellar, lunar, and terrestrial records. J. Geophys. Res. **117**, A08103 (2012). https://doi.org/10.1029/2012JA017706

S.J. Schwartz, Hot flow anomalies near the Earth's bow shock. Adv. Space Res. **15**(8–9), 107–116 (1995). https://doi.org/10.1016/0273-1177(94)00092-F

S.J. Schwartz, C.P. Chaloner, P.J. Christiansen, A.J. Coates, D.S. Hall, A.D. Johnstone, P.M. Gough, A.J. Norris, R.P. Rijnbeek, D.J. Southwood, L.J. Woolliscroft, An active current sheet in the solar wind. Nature **318**(6043), 269–271 (1985). https://doi.org/10.1038/318269a0

K. Seki, M. Hirahara, T. Terasawa, I. Shinohara, T. Mukai, Y. Saito, S. Machida, T. Yamamoto, S. Kokubun, Coexistence of Earth-origin O^{+} and solar wind-origin $\mathrm{H}^{+}/\mathrm{He}^{++}$ in the distant magnetotail. Geophys. Res. Lett. **23**(9), 985–988 (1996). https://doi.org/10.1029/96GL00768

K. Seki, A. Nagy, C.M. Jackman, F. Crary, D. Fontaine, P. Zarka, P. Wurz, A. Milillo, J.A. Slavin, D.C. Delcourt, M. Wiltberger, R. Ilie, X. Jia, S.A. Ledvina, R.W. Schunk, A review of general processes related to plasma sources and losses for solar system magnetospheres. Space Sci. Rev. **192**(1), 27–89 (2015). https://doi.org/10.1007/s11214-015-0170-y

D.E. Shemansky, The role of solar wind ions in the space environment, in *Proc. 23rd Int. Symp. Rarefied Gas Dynamics*. AIP Conf. Proc., vol. 663 (2003), pp. 687–696. https://doi.org/10.1063/1.1581610

K. Shibata, T. Magara, Solar flares: magnetohydrodynamic processes. Living Rev. Sol. Phys. **8**, 6 (2011). https://doi.org/10.12942/lrsp-2011-6

K. Shibata, H. Isobe, A. Hillier, A.R. Choudhuri, H. Maehara, T.T. Ishii, T. Shibayama, S. Notsu, Y. Notsu, T. Nagao, S. Honda, D. Nogami, Can superflares occur on our Sun? Publ. Astron. Soc. Jpn. **65**(3), 49 (2013). https://doi.org/10.1093/pasj/65.3.49

T. Shibayama, H. Maehara, S. Notsu, Y. Notsu, T. Nagao, S. Honda, T.T. Ishii, D. Nogami, K. Shibata, Superflares on solar-typee stars observed with Kepler. I. Statistical properties of superflares. Astrophys. J. Suppl. Ser. **209**, 5 (2013). https://doi.org/10.1088/0067-0049/209/1/5

K. Shiokawa, T. Ogino, K. Hayashi, D.J. McEwen, Quasi-periodic poleward motions of morningside Sun-aligned arcs: a multievent study. J. Geophys. Res. **102**(A11), 24325–24332 (1993). https://doi.org/10.1029/97JA02383

V.I. Shulga, Note on the artefacts in SRIM simulation of sputtering. Appl. Surf. Sci. **439**, 456–461 (2018). https://doi.org/10.1016/j.apsusc.2018.01.039

D.G. Sibeck, T.-D. Phan, R. Lin, R.P. Lepping, A. Szabo, Wind observations of foreshock cavities: a case study. J. Geophys. Res. Space Phys. **107**(A10), SMP-4 (2002). https://doi.org/10.1029/2001JA007539

P. Sigmund, Theory of sputtering. I. Sputtering yield of amorphous and polycrystalline targets. Phys. Rev. **184**, 383–416 (1969)

P. Sigmund, Recollections of fifty years with sputtering. Thin Solid Films **520**, 6031–6049 (2012). https://doi.org/10.1016/j.tsf.2012.06.003

A. Simpson, J.H. Eraker, J.E. Lamport, P.H. Walpole, Electrons and protons accelerated in Mercury's magnetic field. Science **185**, 160–166 (1974). https://doi.org/10.1126/science.185.4146.160

J.A. Slavin, M.H. Acuña, B.J. Anderson, D.N. Baker, M. Benna, S.A. Boardsen, G. Gloeckler, R.E. Gold, G.C. Ho, H. Korth, S.M. Krimigis, R.L. McNutt Jr., J.M. Raines, M. Sarantos, D. Schriver, S.C. Solomon, P. Trávníček, T.H. Zurbuchen, MESSENGER observations of magnetic reconnection in Mercury's magnetosphere. Science **324**(5927), 606–610 (2009). https://doi.org/10.1126/science.1172011

J.A. Slavin, S.M. Imber, S.A. Boardsen, G.A. DiBraccio, T. Sundberg, M. Sarantos, T. Nieves-Chinchilla, A. Szabo, B.J. Anderson, H. Korth, T.H. Zurbuchen, J.M. Raines, C.L. Johnson, R.M. Winslow, R.M. Killen, R.L. McNutt Jr., S.C. Solomon, MESSENGER observations of a flux-transfer-event shower at Mercury. J. Geophys. Res. **117**, A00M06 (2012). https://doi.org/10.1029/2012JA017926

J.A. Slavin, G.A. DiBraccio, D.J. Gershman, S.M. Imber, G.K. Poh, J.M. Raines, T.H. Zurbuchen, X. Jia, D.N. Baker, K.-H. Glassmeier, S.A. Livi, S.A. Boardsen, T.A. Cassidy, M. Sarantos, T. Sundberg, A. Masters, C.L. Johnson, R.M. Winslow, B.J. Anderson, H. Korth, R.L. McNutt Jr., C. Solomon, MESSENGER observations of Mercury's dayside magnetosphere under extreme solar wind conditions. J. Geophys. Res. **119**, 8087–8116 (2014). https://doi.org/10.1002/2014JA020319

J.A. Slavin, H.R. Middleton, J.M. Raines, X. Jia, J. Zhong, W.-J. Sun, S. Livi, S.M. Imber, G.-K. Poh, M. Akhavan-Tafti, J.M. Jasinski, G.A. DiBraccio, C. Dong, R.M. Dewey, M.L. Mays, MESSENGER observations of disappearing dayside magnetosphere events at Mercury. J. Geophys. Res. Space Phys. **124**, 6613–6635 (2019). https://doi.org/10.1029/2019JA026892

J.A. Slavin, D.N. Baker, D.J. Gerhsman, G.C. Ho, S.M. Imber, S.M. Krimigis, T. Sundberg, Mercury's dynamic magnetosphere, in *Mercury: The View after MESSENGER*, ed. by S.C. Solomon, L.R. Nittler, B.J. Anderson (Cambridge University Press, London, 2020), pp. 461–496

J.A. Slavin, S.M. Imber, J.M. Raines, A Dungey cycle in the life of Mercury's magnetosphere, in *Space Physics and Aeronomy Collection Volume 2: Magnetospheres in the Solar System*, ed. by R. Maggiolo,

N. André, H. Hasegawa, D.T. Welling. Geophysical Monograph, vol. 259 (Am. Geophys. Union/Wiley, Washington/New York, 2021). https://doi.org/10.1002/9781119815624.ch34

B.U. Sonnerup, Magnetopause reconnection rate. J. Geophys. Res. **79**(10), 1546–1549 (1974). https://doi.org/10.1029/JA079i010p01546

M. Sporn, G. Libiseller, T. Neidhart, M. Schmid, F. Aumayr, H.P. Winter, P. Varga, M. Grether, D. Niemann, N. Stolterfoht, Potential sputtering of clean SiO_2 by slow highly charged ions. Phys. Rev. Lett. **79**, 945 (1997). https://doi.org/10.1103/PhysRevLett.79.945

A.L. Sprague, A diffusion source for sodium and potassium in the atmospheres of Mercury and the Moon. Icarus **84**, 93–105 (1990). https://doi.org/10.1016/0019-1035(90)90160-B

R. Stadlmayr, P.S. Szabo, B.M. Berger, C. Cupak, R. Chiba, D. Blöch, D. Mayer, B. Stechauner, M. Sauer, A. Foelske-Schmitz, M. Oberkofler, T. Schwarz-Selinger, A. Mutzke, F. Aumayr, Fluence dependent changes of surface morphology and sputtering yield of iron: comparison of experiments with SDTrimSP-2D Nucl. Instrum. Methods Phys. Res., Sect. B, Beam Interact. Mater. Atoms **430**, 42 (2018). https://doi.org/10.1016/j.nimb.2018.06.004

R.D. Starr, D. Schriver, L.R. Nittler, S.Z. Weider, P.K. Byrne, G.C. Ho, E.A. Rhodes, C.E. Schlemm, S.C. Solomon, P.M. Trávníček, MESSENGER detection of electron-induced X-ray fluorescence from Mercury's surface. J. Geophys. Res. **117**, E00L02 (2012). https://doi.org/10.1029/2012JE004118

S.A. Stern, The lunar atmosphere: history, status, current problems, and context. Rev. Geophys. **37**(4), 453–491 (1999). https://doi.org/10.1029/1999RG900005

S.A. Stern, J.C. Cook, J.-Y. Chaufray, P.D. Feldman, G.R. Gladstone, K.D. Retherford, Lunar atmospheric H_2 detections by the LAMP UV spectrograph on the Lunar Reconnaissance Orbiter. Icarus **226**, 1210–1213 (2013). https://doi.org/10.1016/j.icarus.2013.07.011

T.J. Stubbs, J.S. Halekas, W.M. Farrell, R.R. Vondrak, R. Richard, Lunar surface charging: a global perspective using lunar prospector data, in *Workshop on Dust in Planetary Systems (ESA SP-643)*, ed. by H. Krueger, A. Graps 26–30 September 2005, Kauai, Hawaii, USA (2007), pp. 181–184

W.J. Sun, S.Y. Fu, J.A. Slavin, J.M. Raines, Q.G. Zong, G.K. Poh, T.H. Zurbuchen, Spatial distribution of Mercury's flux ropes and reconnection fronts: MESSENGER observations. J. Geophys. Res. Space Phys. **121**, 7590–7607 (2016). https://doi.org/10.1002/2016JA022787

W.J. Sun, J.M. Raines, S.Y. Fu, J.A. Slavin, Y. Wei, G.K. Poh, Z.Y. Pu, Z.H. Yao, Q.G. Zong, W.X. Wan, MESSENGER observations of the energization and heating of protons in the near-Mercury magnetotail. Geophys. Res. Lett. **44**, 8149–8158 (2017). https://doi.org/10.1002/2017GL074276

W.J. Sun, J.A. Slavin, R.M. Dewey, J.M. Raines, S.Y. Fu, Y. Wei, T. Karlsson, G.K. Poh, X. Jia, D.J. Gershman, Q.G. Zong, W.X. Wan, Q.Q. Shi, Z.Y. Pu, D. Zhao, A comparative study of the proton properties of magnetospheric substorms at Earth and Mercury in the near magnetotail. Geophys. Res. Lett. **45**, 7933–7941 (2018). https://doi.org/10.1029/2018GL079181

W.J. Sun, J.A. Slavin, A.W. Smith, R.M. Dewey, G.K. Poh, X. Jia, J.M. Raines, S. Livi, Y. Saito, D.J. Gershman, G.A. DiBraccio, S.M. Imber, J.P. Guo, S.Y. Fu, Q.G. Zong, J.T. Zhao, Flux transfer event showers at Mercury: dependence on plasma β and magnetic shear and their contribution to the Dungey cycle. Geophys. Res. Lett. **47**, e2020GL089784 (2020). https://doi.org/10.1029/2020GL089784

W. Sun, J.A. Slavin, A. Milillo, S. Orsini, X. Jia1, J.M. Raines, S. Livi, J.M. Jasinski, R.M. Dewey, S. Fu, J. Zhao, Q.-G. Zong, Y. Saito, C. Li, MESSENGER observations of planetary ion enhancements at Mercury's northern magnetospheric cusp during Flux Transfer Event Showers (2022). arXiv:2201.03987

D.M. Suszcynsky, J.T. Gosling, M.F. Thomsen, Ion temperature profiles in the horns of the plasma sheet. J. Geophys. Res. **98**(A1), 257–262 (1993). https://doi.org/10.1029/92JA01733

P.S. Szabo, R. Chiba, H. Biber, R. Stadlmayr, B.M. Berger, D. Mayer, A. Mutzke, M. Doppler, M. Sauer, J. Appenroth, J. Fleig, A. Foelske-Schmitz, H. Hutter, K. Mezger, H. Lammer, A. Galli, P. Wurz F. Aumayr, Solar wind sputtering of wollastonite as a lunar analogue material—comparisons between experiments and simulations. Icarus **314**, 98 (2018). https://doi.org/10.1016/j.icarus.2018.05.028

P.S. Szabo, H. Biber, N. Jäggi, M. Brenner, D. Weichselbaum, A. Niggas, R. Stadlmayr, D. Primetzhofer, A. Nenning, A. Mutzke, M. Sauer, J. Fleig, A. Foelske-Schmitz, K. Mezger, H. Lammer, A. Galli, P. Wurz, F. Aumayr, Dynamic potential sputtering of lunar analog material by solar wind ions. Astrophys. J. **891**, 100 (2020a). https://doi.org/10.3847/1538-4357/ab7008

P.S. Szabo, H. Biber, N. Jäggi, M. Wallner, R. Stadlmayr, M.V. Moro, A. Nenning, A. Mutzke, K. Mezger, H. Lammer, D. Primetzhofer, J. Fleig, A. Galli, P. Wurz, F. Aumayr, Experimental insights into space weathering of phobos: laboratory investigation of sputtering by atomic and molecular planetary ions. J. Geophys. Res., Planets **125**, e2020JE006583 (2020b). https://doi.org/10.1029/2020je006583

P.S. Szabo, C. Cupak, H. Biber, N. Jäggi, A. Galli, P. Wurz, F. Aumayr, A theoretical model for the sputtering of rough surfaces. Surf. Interfaces (2022), submitted

J.R. Szalay, A.R. Poppe, J. Agarwal, D. Britt, I. Belskaya, M. Horányi, T. Nakamura, M. Sachse, F. Spahn, Dust phenomena relating to airless bodies. Space Sci. Rev. **214**, 98 (2018). https://doi.org/10.1007/s11214-018-0527-0

V.A. Thomas, S.H. Brecht, Evolution of diamagnetic cavities in the solar wind. J. Geophys. Res. **93**(A10), 11341–11353 (1988). https://doi.org/10.1029/JA093iA10p11341

M.W. Thompson, B.W. Farmery, P.A. Newson, A mechanical spectrometer for analyzing the energy distribution of sputtered atoms of copper and gold. Philos. Mag. **18**(152), 361–383 (1968). https://doi.org/10.1080/14786436808227357

A. Tolstogouzova, S. Daolio, C. Pagura, C.L. Greenwood, Energy distributions of secondary ions sputtered from aluminium and magnesium by Ne^+, Ar^+ and O_2^+: a comprehensive study. Int. J. Mass Spectrom. **214**, 327–337 (2002)

M. Tona, S. Takahashi, K. Nagata, N. Yoshiyasu, C. Yamada, N. Nakamura, S. Ohtani, Coulomb explosion potential sputtering induced by slow highly charged ion impact. Appl. Phys. Lett. **87**, 224102 (2005). https://doi.org/10.1063/1.2136361

P.M. Trávnícek, P. Hellinger, M.G.G.T. Taylor, P. Escoubet, I. Dandouras, E. Lucek, Magnetosheath plasma expansion: hybrid simulations. Geophys. Res. Lett. **34**, L15104 (2007). https://doi.org/10.1029/2007GL029728

P.M. Trávnícek, D. Schriver, P. Hellinger, D. Hercík, B.J. Anderson, M. Sarantos, J.A. Slavin, Mercury's magnetosphere-solar wind interaction for northward and southward interplanetary magnetic field: hybrid simulation results. Icarus **209**, 11–22 (2010). https://doi.org/10.1016/j.icarus.2010.01.008

O. Troshichev, S. Kokubun, Y. Kamide, A. Nishida, T. Mukai, T. Yamamoto, Convection in the distant magnetotail under extremely quiet and weakly disturbed conditions. J. Geophys. Res. **104**(A5), 10249–10263 (1999). https://doi.org/10.1029/1998JA900141

Y. Tsugawa, N. Terada, Y. Katoh, T. Ono, H. Tsunakawa, F. Takahashi, H. Shibuya, H. Shimizu, M. Matsushima, Statistical analysis of monochromatic whistler waves near the Moon detected by Kaguya. Ann. Geophys. **29**, 889–893 (2011). https://doi.org/10.5194/angeo-29-889-2011

Y. Tsugawa, Y. Katoh, N. Terada, T. Ono, H. Tsunakawa, F. Takahashi, H. Shibuya, H. Shimizu, M. Matsushima, Y. Saito, S. Yokota, M.N. Nishino, Statistical study of broadband whistler-mode waves detected by Kaguya near the Moon. Geophys. Res. Lett. **39**(16), L16101 (2012). https://doi.org/10.1029/2012GL052818

H. Tsunakawa, H. Shibuya, F. Takahashi, H. Shimizu, M. Matsushima, A. Matsuoka, S. Nakazawa, H. Otake, Y. Iijima, Lunar magnetic field observation and initial global mapping of lunar magnetic anomalies by MAP-LMAG onboard SELENE (Kaguya). Space Sci. Rev. **154**(1–4), 219–251 (2010). https://doi.org/10.1007/s11214-010-9652-0

H. Tsunakawa, F. Takahashi, H. Shimizu, H. Shibuya, M. Matsushima, Surface vector mapping of magnetic anomalies over the Moon using Kaguya and Lunar Prospector observations. J. Geophys. Res., Planets **120**, 1160–1185 (2015). https://doi.org/10.1002/2014JE004785

L. Tu, C.P. Johnstone, M. Güdel, H. Lammer, The extreme ultraviolet and X-ray Sun in time: high-energy evolutionary tracks of a solar-like star. Astron. Astrophys. **577**, L3 (2015). https://doi.org/10.1051/0004-6361/201526146

O.J. Tucker, W.M. Farrell, R.M. Killen, D.M. Hurley, Solar wind implantation into the lunar regolith: Monte Carlo simulations of H retention in a surface with defects and the H_2 exosphere. J. Geophys. Res., Planets **124**, 278–293 (2019). https://doi.org/10.1029/2018JE005805

D.L. Turner, N. Omidi, D.G. Sibeck, V. Angelopoulos, First observations of foreshock bubbles upstream of Earth's bow shock: characteristics and comparisons to HFAs. J. Geophys. Res. Space Phys. **118**, 1552–1570 (2013). https://doi.org/10.1002/jgra.50198

D.L. Turner, T.Z. Liu, L.B. Wilson III, I.J. Cohen, D.G. Gershman, J.F. Fennell, J.B. Blake, B.H. Mauk, N. Omidi, J.L. Burch, Microscopic, multipoint characterization of foreshock bubbles with Magnetospheric Multiscale (MMS). J. Geophys. Res. Space Phys. **125**, e2019JA027707 (2020). https://doi.org/10.1029/2019JA027707

A.L. Tyler, R.W.H. Kozlowski, D.M. Hunten, Observations of sodium in the tenuous lunar atmosphere. Geophys. Res. Lett. **15**(10), 1141–1145 (1988). https://doi.org/10.1029/GL015i010p01141

O.L. Vaisberg, L.A. Avanov, J.L. Burch, J.H. Waite Jr., Measurements of plasma in the magnetospheric tail lobes. Adv. Space Res. **18**(8), 63–67 (1996). https://doi.org/10.1016/0273-1177(95)00998-1

P. van der Heide, Sputtering and ion formation, Chap. 3, in *Secondary Ion Mass Spectrometry: An Introduction to Principles and Practices* (Wiley, New York, 2014)

J. Varela, F. Pantellini, M. Moncuquet, The effect of interplanetary magnetic field orientation on the solar wind flux impacting Mercury's surface. Planet. Space Sci. **119**, 264–269 (2015). https://doi.org/10.1016/j.pss.2015.10.004

A.N. Volkov, R.E. Johnson, O.J. Tucker, J.T. Erwin, Thermally driven atmospheric escape: transition from hydrodynamic to Jeans escape. Astrophys. J. Lett. **729**, L24 (2011). https://doi.org/10.1088/2041-8205/729/2/L24

R. von Steiger, N.A. Schwadron, L.A. Fisk, J. Geiss, G. Gloeckler, S. Hefti, B. Wilken, R.R. Wimmer-Schweingruber, T.H. Zurbuchen, Composition of quasi-stationary solar wind flows from Ulysses/Solar

Wind Ion Composition Spectrometer. J. Geophys. Res. **105**(A12), 27217–27238 (2000). https://doi.org/10.1029/1999JA000358

U. von Toussaint, A. Mutzke, A. Manhard, Sputtering of rough surfaces: a 3D simulation study. Phys. Scr. T **170**, 014056 (2017). https://doi.org/10.1088/1402-4896/aa90be

A. Vorburger, P. Wurz, S. Barabash, M. Wieser, Y. Futaana, M. Holmström, A. Bhardwaj, K. Asamura, Energetic neutral atom imaging of the lunar surface. J. Geophys. Res. **117**, A07208 (2012). https://doi.org/10.1029/2012JA017553

A. Vorburger, P. Wurz, S. Barabash, M. Wieser, Y. Futaana, C. Lue, M. Holmström, A. Bhardwaj, M.B. Dhanya, K. Asamura, Energetic neutral atom imaging of the lunar surface. J. Geophys. Res. **118**, 3937–3945 (2013). https://doi.org/10.1002/jgra.50337

A. Vorburger, P. Wurz, S. Barabash, M. Wieser, Y. Futaana, M. Holmström, A. Bhardwaj, K. Asamura, First direct observation of sputtered lunar oxygen. J. Geophys. Res. **119**(2), 709–722 (2014). https://doi.org/10.1002/2013JA019207

A. Vorburger, P. Wurz, S. Barabash, Y. Futaana, M. Wieser, A. Bhardwaj, M.B. Dhanya, K. Asamura, Transport of solar wind plasma onto the lunar nightside surface. Geophys. Res. Lett. **43**, 10586–10594 (2016). https://doi.org/10.1002/2016GL071094

M. Vyšinka, Z. Němeček, J. Šafránková, J. Pavlů, J. Vaverka, J. Lavková, Sputtering of spherical SiO_2 samples. IEEE Trans. Plasma Sci. **44**, 1036 (2016). https://doi.org/10.1109/TPS.2016.2564502

M. Wahl, A. Wucher, VUV photoionization of sputtered neutral silver clusters. Nucl. Instrum. Methods Phys. Res. B **94**, 36–46 (1994). https://doi.org/10.1016/0168-583X(94)95655-3

X.-D. Wang, W. Bian, J.-S. Wang, J.-J. Liu, Y.-L. Zou, H.-B. Zhang, C. Lü, J.-Z. Liu, W. Zuo, Y. Su, W.-B. Wen, M. Wang, Z.-Y. Ouyang, C.-L. Li, Acceleration of scattered solar wind protons at the polar terminator of the Moon: results from Chang'E-1/SWIDs. Geophys. Res. Lett. **37**(7) (2010). https://doi.org/10.1029/2010GL042891

S. Wang, Q. Zong, H. Zhang, Hot flow anomaly formation and evolution: cluster observations. J. Geophys. Res. Space Phys. **118**(7), 4360–4380 (2013). https://doi.org/10.1002/jgra.50424

A. Warmuth, G. Mann, Constraints on energy release in solar flares from RHESSI and GOES X-ray observations II. Energetics and energy partition. Astron. Astrophys. **588**, A116 (2016). https://doi.org/10.1051/0004-6361/201527475

G.K. Wehner, C.E. Kenknight, Investigation of sputtering effects on the Moon's surface, Final report (Technical Report). Minneapolis, MN, Litton Systems Inc., Applied Science Div. (1967). https://ntrs.nasa.gov/citations/19670028248

G.K. Wehner, C. Kenknight, D.L. Rosenberg, Sputtering rates under solar-wind bombardment. Planet. Space Sci. **11**(8), 885–895 (1963a). https://doi.org/10.1016/0032-0633(63)90120-X

G.K. Wehner, C.E. Kenknight, D. Rosenberg, Modification of the lunar surface by the solar-wind bombardment. Planet. Space Sci. **11**(11), 1257–1258 (1963b). https://doi.org/10.1016/0032-0633(63)90229-0

A. Wekhof, Negative ions in the ionospheres of planetary bodies without atmospheres. Moon Planets **24**(1), 45–52 (1981). https://rdcu.be/ciKNl

B.Y. Welsh, J. Wheatley, S.E. Browne, O.H.W. Siegmund, J.G. Doyle, E. O'Shea, A. Antonova, K. Forster, M. Seibert, P. Morrissey, Y. Taroyan, GALEX high time-resolution ultraviolet observations of dMe flare events. Astron. Astrophys. **458**, 921–930 (2006). https://doi.org/10.1051/0004-6361:20065304

Y.C. Whang, Interaction of the magnetized solar wind with the Moon. Phys. Fluids **11**(5), 969–975 (1968). https://doi.org/10.1063/1.1692068

M. Wieser, S. Barabash, Y. Futaana, M. Holmström, A. Bhardwaj, R. Sridharan, M.B. Dhanya, P. Wurz, A. Schaufelberger, K. Asamura, Extremely high reflection of solar wind protons as neutral hydrogen atoms from regolith in space. Planet. Space Sci. **57**, 14–15 (2009). https://doi.org/10.1016/j.pss.2009.09.012

M. Wieser, S. Barabash, Y. Futaana, M. Holmström, A. Bhardwaj, R. Sridharan, M.B. Dhanya, A. Schaufelberger, P. Wurz, K. Asamura, First observation of a mini-magnetosphere above a lunar magnetic anomaly using energetic neutral atoms. Geophys. Res. Lett. **37**, L05103 (2010). https://doi.org/10.1029/2009GL041721

J.-P. Williams, D.A. Paige, B.T. Greenhagen, E. Sefton-Nash, The global surface temperatures of the Moon as measured by the Diviner Lunar Radiometer Experiment. Icarus **283**, 300–325 (2017). https://doi.org/10.1016/j.icarus.2016.08.012

L.B. Wilson III, M.L. Stevens, J.C. Kasper, K.G. Klein, B.A. Maruca, S.D. Bale, T.A. Bowen, M.P. Pulupa, C.S. Salem, The statistical properties of solar wind temperature parameters near 1 AU. Astrophys. J. Suppl. Ser. **236**, 41 (2018). https://doi.org/10.3847/1538-4365/aab71c

J.K. Wilson, M. Mendillo, H.E. Spence, Magnetospheric influence on the Moon's exosphere. J. Geophys. Res. **111**, A07207 (2006). https://doi.org/10.1029/2005JA011364

R.M. Winslow, C.L. Johnson, B.J. Anderson, H. Korth, J.A. Slavin, M.E. Purucker, S.C. Solomon, Observations of Mercury's northern cusp region with MESSENGER's magnetometer. Geophys. Res. Lett. **39**, L08112 (2012). https://doi.org/10.1029/2012GL051472

R.M. Winslow, C.L. Johnson, B.J. Anderson, D.J. Gershman, J.M. Raines, R.J. Lillis, H. Korth, J.A. Slavin, S.C. Solomon, T.H. Zurbuchen, M.T. Zuber, Mercury's surface magnetic field determined from proton-reflection magnetometry. Geophys. Res. Lett. **41**, 4463–4470 (2014). https://doi.org/10.1002/2014GL060258

R.M. Winslow, L. Philpott, C.S. Paty, N. Lugaz, N.A. Schwadron, C.L. Johnson, H. Korth, Statistical study of ICME effects on Mercury's magnetospheric boundaries and northern cusp region from MESSENGER. J. Geophys. Res. Space Phys. **122**, 4960–4975 (2017). https://doi.org/10.1002/2016JA023548

R.M. Winslow, N. Lugaz, L. Philpott, C.J. Farrugia, C.L. Johnson, B.J. Anderson, C.S. Paty, N.A. Schwadron, M. Al Asad, Observations of extreme ICME ram pressure compressing Mercury's dayside magnetosphere to the surface. Astrophys. J. **889**, 184 (2020). https://doi.org/10.3847/1538-4357/ab6170

H.F. Winters, J.W. Coburn, Surface science aspects of etching reactions. Surf. Sci. Rep. **14**, 162–269 (1992). https://doi.org/10.1016/0167-5729(92)90009-Z

D.P. Woodruff, *Modern Techniques of Surface Science* (Cambridge University Press, Cambridge, 2016). ISBN 9781107023109

T.N. Woods, F.G. Eparvier, J. Fontenla, J. Harder, G. Kopp, W.E. McClintock, G. Rottman, B. Smiley, M. Snow, Solar irradiance variability during the October 2003 solar storm period. Geophys. Res. Lett. **31**, L10802 (2004). https://doi.org/10.1029/2004GL019571

T.N. Woods, F.G. Eparvier, S.M. Bailey, P.C. Chamberlin, J. Lean, G.J. Rottman, S.C. Solomon, W.K. Tobiska, D.L. Woodraska, Solar EUV experiment (SEE): mission overview and first results. J. Geophys. Res. **110**, A01312 (2005). https://doi.org/10.1029/2004JA010765

T.N. Woods, G. Kopp, P.C. Chamberlin, Contributions of the solar ultraviolet irradiance to the total solar irradiance during large flares. J. Geophys. Res. **111**, A10S14 (2006). https://doi.org/10.1029/2005JA011507

C.-J. Wu, W.-H. Ip, L.-C. Huang, A study of variability in the frequency distributions of the superflares of G-type stars observed by the Kepler mission. Astrophys. J. **798**, 92 (2015). https://doi.org/10.1088/0004-637X/798/2/92

P. Wurz, Solar Wind Composition, in The Dynamic Sun: Challenges for Theory and Observations. ESA SP-600, 5.2, pp. 1–9 (2005). https://ui.adsabs.harvard.edu/abs/2005ESASP.600E..44W

P. Wurz, Erosion processes affecting interplanetary dust grains, in *Nano Dust in the Solar System: Discoveries and Interpretations*. Astrophysics and Space Science Library, vol. 385 (Springer, Berlin, 2012), pp. 161–178. https://doi.org/10.1007/978-3-642-27543-2_8

P. Wurz, L. Blomberg, Particle populations in Mercury's magnetosphere. Planet. Space Sci. **49**(14–15), 1643–1653 (2001). https://doi.org/10.1016/S0032-0633(01)00102-7

P. Wurz, H. Lammer, Monte-Carlo simulation of Mercury's exosphere. Icarus **164**(1), 1–13 (2003). https://doi.org/10.1016/S0019-1035(03)00123-4

P. Wurz, E. Wolfrum, W. Husinsky, G. Betz, L. Hudson, N.H. Tolk, ESD thresholds for excited atoms desorbed from Alkali-Halides. Radiat. Eff. Defects Solids **109**, 203–212 (1989)

P. Wurz, W. Husinsky, G. Betz, Sputtering of clean and oxidized Cr and Ta metal targets using SNMS and SIMS, in *Proceedings of Symposium on Surface Science*, ed. by J.J. Ehrhardt, C. Launois, B. Mutaftschiev, M.R. Tempère (La Plagne, France, 1990), pp. 181–185

P. Wurz, J. Sarnthein, W. Husinsky, G. Betz, P. Nordlander, Y. Wang, Electron-stimulated desorption of neutral ground-state lithium atoms from LiF due to excitation of surface excitons. Phys. Rev. B **43**, 6729–6732 (1991). https://doi.org/10.1103/PHYSREVB.43.6729

P. Wurz, R.F. Wimmer-Schweingruber, K. Issautier, P. Bochsler, A.B. Galvin, F.M. Ipavich, Composition of magnetic cloud plasmas during 1997 and 1998, in *American Institute Physics on Solar and Galactic Composition* vol. CP-598 (2001), pp.145–151. https://doi.org/10.1063/1.1433993

P. Wurz, R. Wimmer-Schweingruber, P. Bochsler, A. Galvin, J.A. Paquette, F. Ipavich, Composition of magnetic cloud plasmas during 1997 and 1998. AIP Conf. Proc. **679**, 685–690 (2003). https://doi.org/10.1063/1.1618687

P. Wurz, U. Rohner, J.A. Whitby, C. Kolb, H. Lammer, P. Dobnikar, J.A. Martín-Fernández, The lunar exosphere: the sputtering contribution. Icarus **191**, 486–496 (2007). https://doi.org/10.1016/j.icarus.2007.04.034

P. Wurz, J.A. Whitby, U. Rohner, J.A. Martín-Fernández, H. Lammer, C. Kolb, Self-consistent modelling of Mercury's exosphere by sputtering, micro-meteorite impact and photon-stimulated desorption. Planet. Space Sci. **58**, 1599–1616 (2010). https://doi.org/10.1016/j.pss.2010.08.003

P. Wurz, D. Abplanalp, M. Tulej, M. Iakovleva, V.A. Fernandes, A. Chumikov, G. Managadze, Mass spectrometric analysis in planetary science: investigation of the surface and the atmosphere. Sol. Syst. Res. **46**, 408–422 (2012). https://doi.org/10.1134/S003809461206007X

P. Wurz, D. Gamborino, A. Vorburger, J.M. Raines, Heavy ion composition of Mercury's magnetosphere. J. Geophys. Res. **124**, 2603–2612 (2019). https://doi.org/10.1029/2018JA026319

B.V. Yakshinskiy, T.E. Madey, Photon-stimulated desorption as a substantial source of sodium in the lunar atmosphere. Nature **400**, 642–644 (1999). https://doi.org/10.1038/23204

B.V. Yakshinskiy, T.E. Madey, Desorption induced by electronic transitions of Na from SiO_2: relevance to tenuous planetary atmospheres. Surf. Sci. **451**, 160–165 (2000). https://doi.org/10.1016/S0039-6028(00)00022-4

B.V. Yakshinskiy, T.E. Madey, DIET of alkali atoms from mineral surfaces. Surf. Sci. **528**, 54–59 (2003). https://doi.org/10.1016/S0039-6028(02)02610-9

B.V. Yakshinskiy, T.E. Madey, Photon-stimulated desorption of Na from a lunar sample: temperature-dependent effects. Icarus **168**, 53–59 (2004). https://doi.org/10.1016/j.icarus.2003.12.007

B.V. Yakshinskiy, T.E. Madey, Temperature-dependent DIET of alkalis from SiO_2 films: comparison with a lunar sample. Surf. Sci. **593**, 202–209 (2005). https://doi.org/10.1016/j.susc.2005.06.062

H. Yang, J. Liu, Q. Gao, X. Fang, J. Guo, Y. Zhang, Y. Hou, Y. Wang, Z. Cao, The flaring activity of M dwarfs in the Kepler field. Astrophys. J. **849**, 36 (2017). https://doi.org/10.3847/1538-4357/aa8ea2

M. Zelen, N.C. Severo, Probability functions, in *Handbook of Mathematical Functions*, ed. by M. Abramowitz, A. Stegun (Dover, New York, 1965)

H. Zhang, D.G. Sibeck, Q.-G. Zong, N. Omidi, D. Turner, L.B.N. Clausen, Spontaneous hot flow anomalies at quasi-parallel shocks: 1. Observations. J. Geophys. Res. Space Phys. **118**, 3357–3363 (2013). https://doi.org/10.1002/jgra.50376

A. Zhang, M. Wieser, C. Wang, S. Barabash, W. Wang, X. Wang, Y. Zou, L. Li, J. Cao, L. Kalla, L. Dai, J. Svensson, L. Kong, M. Oja, B. Liu, V. Alatalo, Y. Zhang, J. Talonen, Y. Sun, M. Emanuelsson, C. Xue, L. Wang, F. Wang, W. Liu, Emission of energetic neutral atoms measured on the lunar surface by Chang'E-4. Planet. Space Sci. **189**, 104970 (2020). https://doi.org/10.1016/j.pss.2020.104970

J.F. Ziegler, M.D. Ziegler, J.P. Biersack, SRIM – the stopping and range of ions in matter. Nucl. Instrum. Methods Phys. Res., Sect. B, Beam Interact. Mater. Atoms **268**(11–12), 1818–1823 (2010). https://doi.org/10.1016/j.nimb.2010.02.091

F.M. Zimmermann, W. Ho, Velocity distributions of photochemically desorbed molecules. J. Chem. Phys. **100**(10), 7700–7706 (1994). https://doi.org/10.1063/1.466864

E. Zinner, On the constancy of solar particle fluxes form track, thermoluminescence and solar wind measurement in lunar rocks, in *The Ancient Sun: Fossil Record in the Earth, Moon and Meteorites*, ed. by R.O. Pepin, J.A. Eddy, R.B. Merrill (Pergamon Press, New York, 1980), pp. 201–226. http://adsabs.harvard.edu/full/1980asfr.symp..201Z

Q.-G. Zong, B. Wilken, J. Woch, T. Mukai, T. Yamamoto, G.D. Reeves, T. Doke, K. Maezawa, D.J. Williams, S. Kokubun, S. Ullaland, Energetic oxygen ion bursts in the distant magnetotail as a product of intense substorms: three case studies. J. Geophys. Res. Space Phys. **103**(A9), 20339–20363 (1998). https://doi.org/10.1029/97JA01146

T.H. Zurbuchen, J.M. Raines, G. Gloeckler, S.M. Krimigis, J.A. Slavin, P.L. Koehn, R.M. Killen, A.L. Sprague, R.L. McNutt, S.C. Solomon, MESSENGER observations of the composition of Mercury's ionized exosphere and plasma environment. Science **321**, 90–92 (2008). https://doi.org/10.1126/science.1159314

T.H. Zurbuchen, J.M. Raines, J.A. Slavin, D.J. Gershman, J.A. Gilbert, G. Gloeckler, B.J. Anderson, D.N. Baker, H. Korth, S.M. Krimigis, M. Sarantos, D. Schriver, R.L. McNutt Jr., S.C. Solomon, MESSENGER observations of the spatial distribution of planetary ions near Mercury. Science **333**, 1862–1865 (2011). https://doi.org/10.1126/science.1211302